Direct Numerical Simulation of Bubble-Bubble and Droplet-Droplet Interaction Using a Surface Thin Film Model

Ndivhuwo M. Musehane

Dissertation presented for the degree of
Master of Science

in the Department of Mathematics and Applied Mathematics
University of Cape Town

July 22, 2016

Supervisors:
Prof. B. Daya Reddy
Dr. Oliver F. Oxtoby

Declaration of Authorship

I, Ndivhuwo M. Musehane, know the meaning of plagiarism and declare that all the work in this dissertation titled, "Direct Numerical Simulation of Bubble-Bubble and Droplet-Droplet Interaction Using a Surface Thin Film Model" save for which is properly acknowledged, is my own.

Signed: Ndivhuwo M. Musehane

Date: 22/07/2016

UNIVERSITY OF CAPE TOWN

Abstract

Faculty of Science
Department of Mathematics and Applied Mathematics

Master of Science

Direct Numerical Simulation of Bubble-Bubble and Droplet-Droplet Interaction Using a Surface Thin Film Model

by Ndivhuwo M. Musehane

This dissertation deals with the simulation of dispersed multiphase flow. The particle-particle and particle-fluid interactions in this class of flows play an important role on the hydrodynamics and fluid transport phenomena that govern the overall flow behaviour. Accurate computational modelling of the particle-particle and particle-fluid interactions is thus required to correctly model the flow. The aim of this study is to use a Direct Numerical Simulation approach based on a smoothed Volume Of Fluid method to model particle-particle interactions in a dispersed multiphase flow at a fundamental level, and employing a surface thin film model, to drastically reduce the computational effort required. A multiscale modelling approach is followed with the smoothed Volume Of Fluid simulation on the particle scale and the surface thin film model simulation on the thin-film scale. The resulting governing equations are the Navier-Stokes equations for an incompressible viscous multiphase Newtonian fluid undergoing laminar and isothermal three-dimensional flow, the interface advection equation and the reduced order surface thin film equation. The model equations are discretized using the Finite Volume Method and implemented into the open source software OpenFOAM®. The numerical solution is obtained by solving the resulting non-linear system of equations implicitly on a structured computational grid on parallel processors using a pressure correction algorithm to converge the pressure at each time step. The study is restricted to gas-liquid systems where particles could either be bubbles or droplets; rigid particles are not considered. The model is tested against experimental results from binary collision of hydrocarbon droplets. Good qualitative numerical results are obtained at a practical computational cost.

Acknowledgements

I acknowledge the Council for Scientific and Industrial Research (CSIR) for the funding provided for this study through a Masters Studentship. I would like to thank the following people for their valuable contribution: Dr Oliver Oxtoby for your guidance, encouragement and support throughout this study. Prof. Daya Reddy for your inputs in overseeing and monitoring the progress of this study and Dr Johan Heyns for keeping me on track and providing technical assistance.

Contents

Declaration of Authorship i

Abstract ii

Acknowledgements iii

Contents iv

List of Figures vii

List of Tables ix

Abbreviations x

Symbols xi

1 Introduction 1
- 1.1 Applications . . . 1
- 1.2 Computational modelling of multiphase flow . . . 3
  - 1.2.1 Euler-Euler and Euler-Lagrange formulation . . . 4
  - 1.2.2 Interface tracking methods . . . 7
  - 1.2.3 Interface capturing methods . . . 8
  - 1.2.4 Volume-Of-Fluid method . . . 9
  - 1.2.5 Surface thin film model . . . 12
- 1.3 Motivation . . . 13
  - 1.3.1 Limitations of current models . . . 14
  - 1.3.2 Need for additional research . . . 15
- 1.4 Research objectives . . . 16
- 1.5 Dissertation outline . . . 16

2 Multiphase flow modelling 18
- 2.1 Volume averaging . . . 19
- 2.2 Single-phase volume averaged equations . . . 20
- 2.3 Two-phase mixture volume averaged equations . . . 21
- 2.4 VOF method . . . 22

2.5 Surface tension modelling with CSF . . . 24
2.6 Discretization of solution domain . . . 26
2.7 Discretization of governing equations . . . 27
2.7.1 Momentum equation . . . 28
2.7.2 VOF advection equation . . . 29
2.7.3 Smooth VOF equation . . . 30
2.8 Pressure equation . . . 30
2.9 Implementation into OpenFOAM® . . . 31
2.10 Closure . . . 32

3 Particle Interaction Modelling **33**
3.1 Numerical coalescence . . . 34
3.2 Multiple Marker VOF method . . . 37
3.3 Surface thin film model of coalescence . . . 39
3.3.1 Problem description . . . 41
3.3.2 Model assumptions . . . 42
3.3.3 Boundary conditions . . . 43
3.3.4 Model derivation . . . 44
3.4 Numerical Implementation . . . 47
3.4.1 Initial separation distance . . . 48
3.4.2 Thin film region . . . 50
3.5 Closure . . . 54

4 Validation **55**
4.1 Test case: static sphere . . . 56
4.1.1 Computational set-up . . . 56
4.1.2 Numerical results . . . 57
4.2 Test case: droplet impact onto a liquid-liquid interface . . . 60
4.2.1 Experimental set-up . . . 60
4.2.2 Computational set-up . . . 61
4.2.3 Numerical results . . . 63
4.3 Test case: Tetradecane droplet impact in 1 atm Nitrogen . . . 67
4.3.1 Experimental set-up . . . 67
4.3.2 Computational set-up . . . 68
4.3.3 Numerical results . . . 69
4.3.3.1 Selection of parameter ξ . . . 69
4.3.3.2 Selection of parameter h_{Crit} . . . 71
4.3.3.3 Droplet time series plots . . . 72
4.4 Closure . . . 73

5 Conclusions **80**
5.1 Summary . . . 80
5.1.1 Motivation . . . 80
5.1.2 Fluid flow modelling . . . 81
5.1.3 Particle interaction modelling . . . 81
5.2 Findings . . . 82
5.3 Recommendations for further study . . . 84

A Volume averaging theorems **85**

B Solution procedure flow chart **86**

Bibliography **87**

List of Figures

2.1 A general polyhedral shaped Control Volume in three dimensions 26

3.1 Two immiscible spheres with radius R in a discretized domain 34
3.2 Two immiscible spheres with radius R in a discretized domain with $\frac{D}{\delta h} = 20$ 35
3.3 Two immiscible spheres with radius R in a discretized domain with $\frac{D}{\delta h} = 200$ 35
3.4 Schematic representation of the surface tension force directions in the standard VOF method 36
3.5 Two immiscible spheres with radius R in a discretized domain represented by the SMMVOF method 37
3.6 Schematic representation of the surface tension force in the SMMVOF method 38
3.7 Two particles with radius R approaching each other with velocities $\mathbf{u}_1$ and $\mathbf{u}_2$ 40
3.8 Two particles with radius R approaching each other with velocities $\mathbf{u}_1$ and $\mathbf{u}_2$ forming a locally planar thin film 41
3.9 Dimpled thin liquid film between two interfaces 41
3.10 Close-up view of a locally planar thin film 42
3.11 Boundary conditions for two-dimensional planar thin film model 43

4.1 Pressure at different values of χ for $\sigma = 0.001$ kgs^{-2} 57
4.2 Pressure at different values of χ for $\sigma = 0.01$ kgs^{-2} 58
4.3 Pressure at different values of χ for $\sigma = 0.1$ kgs^{-2} 58
4.4 Comparison between the nonphysical velocity estimates from the unsmoothed (left) to the smoothed (right) volume fraction 59
4.5 Schematic representation of the computational set-up 62
4.6 Shape profile of droplet and liquid-liquid interface before and during droplet impact: experimental (left) and numerical (right) 64
4.7 Numerical and experimental results (solid lines and tic marks respectively); (a) Normalized center line position of upper ($\Diamond$), lower ($*$) and liquid-liquid interface ($+$), (b) Experimental and numerical (solid lines and tic marks respectively) normalized droplet height 65
4.8 Droplet Reynolds number 66
4.9 Axisymmetric case set-up 68
4.10 Thin film region β (region in red) for Case I with $\xi = 3$ 70
4.11 Variation of parameter ξ with time for (a) Case I, (b) Case II, (c) Case III and (d) Case IV 71
4.12 Time series interface shape deformations for Case I 75
4.13 Time series interface shape deformations for Case II 76
4.14 Time series interface shape deformations for Case III 77

4.16 Time series interface shape deformations for Case IV 79

B.1 Flow chart of numerical algorithm 86

List of Tables

4.1 Material Properties of a two-dimensional sphere in a square domain . . . 56
4.2 Percentage error difference between successive values of χ for $\sigma = 0.001$ kgs^{-2} 58
4.3 Material Properties of silicon oil (Dow Corning Fluid 200®) and water/glycerine mixture (Mohamed-Kassim and Longmire, 2003) 61
4.4 Experimental Parameters (Mohamed-Kassim and Longmire, 2003) 61
4.5 Computational arrangement comparison between current study and the numerical results of Coyajee and Boersma (2009) 66
4.6 Material Properties for Tetradecane and Nitrogen at 20°C (Pan et al., 2008) 68
4.7 Physical Quantities (Pan et al., 2008) 68
4.8 Minimum film thickness h_{Min} (m) for Case I, Case II, Case III and Case IV 70

Abbreviations

CFD	**C**omputational **f**luid **d**ynamics
CLSVOF	**C**omposite **L**evel **S**et and **V**olume **O**f **F**luid
CSF	**C**ontinuum **S**urface **F**orce
DNS	**D**irect **N**umerical **S**imulation
FVM	**F**inite **V**olume **M**ethod
LS	**L**evel **S**et
OpenFOAM®	**O**pen **F**ield **O**peration **A**nd **M**anipulation
SMMVOF	**S**moothed **M**ultiple **M**arker **V**olume **O**f **F**luid
VOF	**V**olume **O**f **F**luid

Symbols

Roman Letters

a	Interpolation ratio for face value from cell centre value	-
$\mathbf{A}_f$	Surface normal area vector	-
c	General scalar	-
D	Droplet diameter	m
$\mathbf{E}$	Rate of deformation tensor	-
$\mathbf{f}$	Body forces	-
$\mathbf{f}_\sigma$	Surface tension force	-
$\mathbf{F}$	Volumetric flux through the face	-
$\mathbf{g}$	Gravitational acceleration	ms^{-2}
h	Thin film thickness or height	m
h_{Crit}	Critical thin film thickness	m
h_{Est}	Initial thin film thickness estimate	m
$\mathbf{I}$	Identity tensor	-
M	Mass flow rate through thin film	-
$\mathbf{n}$	Outward unit normal vector	-
N	Number of dispersed volumes	-
p	Pressure	$\mathrm{kgm}^{-1}\mathrm{s}^{-2}$
R	Radius of sphere	m
$\mathbb{R}^3$	Real three-dimensional space	-
S	Source term	-
$\bar{S}$	Average value of source term	-
t	Time	s
t_d	Drainage time	s
$\mathbf{u}$	Fluid velocity	ms^{-1}

$\mathbf{v}$	Interface velocity	ms^{-1}
V	Volume of domain Ω	m^3
w_i	Experimental impact/terminal velocity	ms^{-1}
$\mathbf{x}$	Position vector in space	m
X	Indicator function	-

Greek Letters

α	Volume fraction field	-
β	Thin film region indicator	-
Γ	Interface separating two fluids	-
δ	Distance between adjacent cell centres	m
δh	Mesh spacing length	m
δ_s	Surface delta function	-
Δ	Change in a quantity	-
η	Smoothing parameter	-
κ	Interface signed curvature	m^{-1}
λ	Second coefficient of viscosity	-
μ	Dynamic viscosity	$\mathrm{kgm}^{-1}\mathrm{s}^{-1}$
ξ	Parameter for the width of thin film region	-
ρ	Density	kgm^{-3}
σ	Surface tension	kgs^{-2}
$\boldsymbol{\tau}$	Stress tensor	-
ϕ	Mass flux through face	-
χ	Number of smoothing cells	-
Ψ	General scalar or vector	-
$\langle\Psi\rangle$	Average value of Ψ	-
∇	Gradient operator	-
Ω	Domain in three-dimensional real space	-
$\partial\Omega$	Rigid boundary of Ω	-

Superscripts

m	Current time step	-
s	Smooth	-
T	Transpose	-

Subscripts

f	Face centre	-
i	Time step	-
k	Phase	-
l	Liquid	-
m	Mixture	-
N	Centroid point of neighbouring CV	-
P	Centroid point of CV	-
θ	Fluid volume	-
t	Tangential	-

For my parents

Chapter 1

Introduction

This dissertation deals with the simulation of dispersed multiphase flow. Multiphase flows consist of multiple materials either with different phases (gas and/or liquid and/or solid) or with different material properties (fluid and fluid). Dispersed multiphase flow is a class of flow in which discrete particles are suspended within a continuous phase. For our purposes particles can either be droplets suspended in a gaseous or liquid continuous phase or gas bubbles suspended in a liquid phase. Solid particles are not considered in this dissertation.

The particle-particle and particle-fluid interactions in this class of flows play an important role in the hydrodynamics and fluid transport phenomena that govern the overall flow behaviour. Accurate computational modelling of the particle-particle and particle-fluid interactions is thus required to correctly model the flow. In this dissertation we attempt to address some of the shortcomings of existing modelling techniques.

Dispersed multiphase flows are found in processes in the chemical, petrochemical, aerospace and manufacturing industries, and in nature. The discussion that follows gives various application areas where particle-particle interactions are important.

1.1 Applications

In chemical, petrochemical and biological processes, bubble column reactors are commonly used. These are multiphase reactors where a gas phase is dispersed into a liquid phase in the form of bubbles. They have wide applications as liquid contactors, by dispersing the gas phase into the liquid phase for a chemical reaction to occur. For example, in coal liquefaction – the process of changing coal into a liquid hydrocarbon

for the later production of liquid fuels – hydrogen gas is dispersed into a slurry of coal and catalysts in a bubble column reactor.

Their wide application in industry can be attributed to their simple construction (Jakobsen et al., 2005) and due to this there are few degrees of freedom that can be changed to improve their performance (Ranade, 1997). This leaves a need to understand in detail the fluid flow phenomena that occur in the columns.

Two types of flow regimes are commonly encountered depending on the reactor operating conditions, namely the homogeneous regime, characterized by uniform small spherical bubbles with no coalescence or breakup and low superficial gas velocities, and the heterogeneous or churn turbulent regime, characterized by high superficial gas velocities which encourage coalescence and breakup, and which leads to a wide bubble size distribution (Jakobsen et al., 2005, Krishna et al., 1999).

The bubbles in a bubble column reactor play a crucial role in providing the energy needed for mixing through interfacial momentum transfer. The complex bubble interactions that lead to coalescence or break-up of bubbles make it difficult to simulate bubble column reactors since the hydrodynamic behaviour is poorly understood. This has limited the optimal scale-up and design of the reactors (Jakobsen et al., 2005). Coalescence and break-up are responsible for the bubble size distribution which directly influences the interfacial momentum transfer between the liquid and gas phases. This in turn greatly affects the optimal operating conditions of the reactor.

In contrast to the bubble-bubble and bubble-fluid interactions in a bubble column reactor, droplet-fluid and droplet-droplet interactions are found in atomized mixtures. Atomization is a process whereby a liquid solution is split into tiny droplets to form a spray (Gorokhovski and Herrmann, 2008). Atomized mixtures are found in various processes including but not limited to spray drying, propulsion systems in the aerospace industry, and in combustion engines.

In spray drying the liquid solution is fed into the spraying chamber and atomized into tiny droplets which come into contact with the drying medium to form a powder. The spray drying process occurs in four distinct stages: (1) atomization of the liquid into the drying chamber, (2) spray contact with hot air, (3) moisture evaporation from the droplets producing the powder, and lastly (4) separation of the powder from the air stream (Kuriakose and Anandharamakrishnan, 2010). This process can be applied to the production of food (e.g. powdered milk, instant coffee, soup) and pharmaceutical products (Pawar et al., 2015).

Droplet-droplet interactions which result in either coalescence or rebound are common in stage 2 of the spray drying process and influence the particle distribution in the

spray chamber, which in turn greatly affects the properties of the powder produced. Computational fluid dynamics (CFD) modelling of the droplet-droplet and droplet-fluid interactions is a powerful tool that can be used to understand this complex hydrodynamic behaviour.

In turbojet and diesel engines the fuel is atomized and injected into the combustion chamber. Droplet-droplet collisions determine the characteristics of the spray and influence to a degree the stability of flame ignition (Murrone and Villedieu, 2011).

Bubble-bubble, bubble-fluid and bubble-solid interactions are found in a flotation cell. Flotation is used, for example in the treatment of waste water and in the extraction of minerals from an ore in the mining industry.

In the minerals industry the mineral ore is ground and mixed with liquids and catalysts in a flotation cell which is similar to a bubble column reactor. Air is dispersed in the form of bubbles at the bottom of the tank and as the bubbles rise to the top of the reactor the mineral particles attach to the bubbles. The bubble size distribution directly affects the overall gas hold up which has major implications on the flotation rate (Gorain et al., 1995).

Multiphase microfluidics is becoming an increasingly popular research area that is characterized by manipulating fluids inside micrometer (μm) length scale channels (Zhao and Middelberg, 2011). A microfluidic chip is commonly used in many applications. It is made of a material etched with μm channels connected to an input and an output. The channels can be T-junctions where the fluid from the input can be separated into droplets. Droplet interactions which result in coalescence influence the chemical reactions and mixing.

1.2 Computational modelling of multiphase flow

The industrial processes and applications highlighted above demonstrate the need to understand and study particle-particle and particle-fluid interactions. In most of these applications the particle-fluid phase ratio is high; this results in an increase in particle collision. Coalescence greatly affects the size distribution and shapes which are important aspects that affect the optimal operating conditions. This calls for accurate modelling of the collision event with its associated coalescence and rebound.

The collision process results in either rebound or coalescence of the particles depending on particle size, velocity, shape etc. The vastly different outcomes and their sensitive

dependence on the aforementioned parameters make the accurate modelling of collision very important in predicting the macroscopic properties of the flow.

The collision process can be described in three stages by the film drainage theory (Chen et al., 1984) and is considered very complex. Consider two interacting particles; Stage 1 is when they approach each other, and as they do so a thin liquid film of the surrounding fluid is trapped between them; Stage 2 is when this liquid film drains out; and lastly in Stage 3 the particles will either coalesce if the thin film becomes unstable, leading to rupture or bounce apart if the liquid film does not attain this critical film thickness.

The governing equations for the particle-particle interactions in a dispersed multiphase fluid are the Navier-Stokes equations. The complexity in multiphase flow modelling comes from the discontinuity of fluid properties across the interface.

CFD is widely used alongside experimentation as a tool to study in detail the transport phenomena that govern multiphase flow. The modelling approaches used differ in their description and treatment of the dispersed particles. The most widely employed techniques are the Euler-Euler, Euler-Lagrange, front tracking and front capturing methods.

The first two methods rely heavily on prior knowledge of the flow structures in the form of empirical correlations when modelling particle-particle interactions. Front capturing and front tracking methods provide a Direct Numerical Simulation (DNS) approach that explicitly tracks the motion of the interface between phases. This makes it easier to model particle-particle interactions from first principles, but at far greater computational cost. DNS provides a fundamental level modelling approach to study the hydrodynamic behaviour.

1.2.1 Euler-Euler and Euler-Lagrange formulation

In the Euler-Euler formulation both phases are described as inter-penetrating continuous media. An Eulerian description of fluid properties is used for both phases. The different phases are defined by a phase fraction field and the volume averaged mass conservation equations are assembled and solved for each individual phase. It describes the motion of the two phases in a macroscopic sense (Chen et al., 2004) in which a continuous field is used to represent the concentration of dispersed particles, and is typically used for large scale flow structures.

Closure relations are required to close the system of governing equations in the Euler-Euler formulation (Jakobsen, 2014). The coupling between the phases is achieved by introducing empirical or simplified theoretical models for the drag and lift forces on the dispersed particles (Jakobsen, 2014).

In contrast to the Euler-Euler formulation, the Euler-Lagrange formulation uses an Eulerian description for the continuous phase only and a Lagrangian description is used for the dispersed phase. An equation of motion is solved to track the motion of each individual particle, with the particles often assumed to be hard spheres. Similar to the Euler-Euler formulation, empirical correlations are required for the Euler-Lagrange formulation in order to represent the coupling between the continuous and dispersed phases.

Studies with the Euler-Euler formulation include the study of Sokolichin and Eigenberger (1994) who solved numerically for the gas-liquid bubble flow in a loop reactor or bubble column reactor using a laminar two-dimensional dynamic model. Their model assumed a single bubble class and ignored bubble coalescence and re-dispersion. Coupling of the two phases was achieved by using an interaction force term which they noted could not be considered in detail in the Euler-Euler formulation but would need to be approximated with an empirical correlation.

The study of Grevskott et al. (1996) on bubble column reactors included a sub-model for bubble size into the Euler-Euler model. Although the bubble size distribution in the heterogeneous regime qualitatively agreed with experiments, the radial size profiles did not and they suggested the use of a bubble size distribution model based on the population balance equation. The population balance equation is an equation that solves for the number density of particles. It requires numerical values of collision frequency which is determined by empirical models.

Fleischer et al. (1996) used a one-dimensional dynamic two-phase model to study the transient behaviour of a bubble column reactor and calculated the bubble size distribution using a population balance equation that included terms for growth, breakup and coalescence of the bubbles. The results obtained were able to predict qualitatively the transient behaviour. Colella et al. (1999) used a bubble-bubble interaction model to obtain correct breakage and coalescence rates to include into the population balance equation for accurate prediction of bubble size distribution in a bubble column reactor. Chen et al. (2005) compared different coalescence and breakup closures for the population balance equation in the heterogeneous regime; the results showed that the different closures did not produce significantly different results.

Although the population balance equation coupled to the Euler-Euler model has helped researchers obtain good agreement with experimental results, most of the closures that are needed for the equations are not fundamental but empirical correlations that have been derived from phenomenological models. This leaves some of the models only valid for a specific flow regime (homogeneous or heterogeneous) and specific experimental conditions.

In the Euler-Lagrange model the particle-particle interactions are directly modelled. Delnoij et al. (1997b) coupled to the Euler-Lagrange model a hard nondeformable sphere collision model from gas-fluidized beds with the aim of modelling the direct bubble-bubble interactions. The assumption of nondeformable bubbles was not valid for the heterogeneous regime and most studies including those by Delnoij et al. (1999) and Darmana et al. (2005) have been limited to the homogeneous regime. Larger bubbles may have complex shapes and may be poorly represented.

An advantage of the Euler-Euler formulation is the computational efficiency it provides for practical applications, but at the cost of accuracy (Jakobsen et al., 1997). The Euler-Lagrange model is computationally intensive, but tracking particle clusters instead of individual particles can reduce computational cost (O'Rourke et al., 2009). The main advantage of the Euler-Lagrange method is that particle-particle and particle-liquid interactions can be individually modelled (Sokolichin and Eigenberger, 1994) while still assuming a particle shape (e.g. hard sphere) and empirical drag correlations.

According to a comparison between the two formulations, Lapin and Lübbert (1994) found that the results of the Euler-Euler model were corrupted with numerical diffusion when applied to a bubble column reactor and suggested that the tracking of individual bubbles or bubble clusters as done in the Euler-Lagrange model could be a solution to this problem. However, a comparison of the two models again by Sokolichin et al. (1997) showed that the use of second-order discretization based on the total variation diminishing method instead of first-order upwind in the solution of the gas hold-up equation considerably reduced the numerical diffusion.

Both the Euler-Euler and Euler-Lagrange formulations have their weaknesses and their strong points. They both are deficient however in that they use empirical closure models whenever coalescence of particles is included in a model, and are thus not viable candidates in studying particle-particle interactions on a fundamental level.

When modelling a bubble column reactor, Lubbert et al. (1996) suggested using three different length scales; the bubble, the bubble swarm and the reactor scale with the mechanisms in each scale independent of each other, which allows for a separation of the transport properties according to length scale. Delnoij et al. (1997a) noted that using a generalized CFD model is not efficient in modelling the bubble column reactor and suggested using a "hierarchy of models". This hierarchy would include a tracking method to be used to give detailed data on particle-particle and particle-fluid interactions which can be used to validate the closure models used in Euler-Euler and Euler-Lagrange type simulations. This multi-scale modelling technique is the approach of the present study.

We turn our attention to DNS type approaches because it is difficult to do sufficiently well controlled experiments and/or to extract detailed enough data to set all the empirical parameters in the Euler-Euler and Euler-Lagrange methods correctly. A formulation similar to the Euler-Euler can be identified that describes the flow in an Eulerian framework, but which uses a tracking technique to describe the particle-fluid interface.

Each particle is simulated by tracking its interface instead of using an average particle distribution. The small resolution of the fluid velocity is obtained and particle coalescence, break-up, merging and topology changes that are of importance in particle-particle modelling can be accurately captured (Delnoij et al., 1997b). The tracking methods discussed here fall under two categories: the interface tracking methods, and interface capturing methods.

1.2.2 Interface tracking methods

Interface tracking and Lagrangian type methods involve computational elements moving through a stationary Eulerian grid (de Sousa et al., 2004), where the computational mesh is moved with the interface. Examples include the Marker-and-Cell technique of Harlow and Welch (1965) where marker particles are used to track the interface, and the front-tracking method developed by Unverdi and Tryggvason (1992) which also explicitly tracked the interface using computational elements. Unverdi and Tryggvason (1992) used two grids; a three-dimensional Cartesian and stationary grid defined the computational domain while a two-dimensional triangular moving grid over-set on the three-dimensional grid was used to describe the interface.

Unverdi and Tryggvason (1992) studied the rise of a steady-state gas bubble and the collision of two equal sized bubbles and noted that the front tracking method has a limitation when two interfaces interact. The bubbles remained separate domains and could not merge together unless the interface between them was explicitly removed. Nobari et al. (1996) studied a binary head-on collision of equal sized droplets using a front tracking method with fluids that have low density and viscosity ratios. The coalescence was performed artificially by removing the interfaces at a prescribed time. Unverdi and Tryggvason (1992) and Nobari et al. (1996) suggested that a sub-grid model that calculated the pressure and the velocities in the thin film region to predict the coalescence time would provide a model with good predictive capabilities.

The greatest advantage of the front-tracking technique is that the surface tension can be incorporated into the method in a natural way. However, modelling the coalescence of particles is complex. The front-tracking method is computationally expensive and exhibits mesh entanglement whenever there are large topology changes.

1.2.3 Interface capturing methods

In contrast to the front-tracking technique, interface capturing methods can be described as methods where the interface is reconstructed from field variables. Examples include the Level Set (LS) method (Sethian and Smereka, 2003), the Volume of Fluid (VOF) method (Hirt and Nichols, 1981) and other variations and the Composite Level Set and Volume of Fluid (CLSVOF) method (Sussman and Puckett, 2000).

In the LS method the interface is defined as the zero level-set of a characteristic function ϕ with the initial function chosen as the signed distance function to the interface (Sethian and Smereka, 2003). In general the LS method can be described as the advection of a smooth function by the velocity field. The advantage of the LS method is its accuracy in the computation of the surface normal and curvature because it uses a smooth function ϕ in the calculation of gradients (Sussman and Puckett, 2000). The main disadvantage of the LS method is that it does not conserve mass in cases of high interface deformations (Denner et al., 2014). The collision between particles can result in very high shape deformations and so the LS method has not been considered in this work.

The VOF method can be generalized as the advection of a discontinuous field (Denner et al., 2014). The discontinuous field is the volume fraction field α, described as the ratio of the volume of the first fluid to the total fluid volume in a cell. The value of α is 1 in the first fluid and 0 in the second with the interface denoted by cells with values between 0 and 1 (Hirt and Nichols, 1981). An interface advection equation uses the velocity to propagate the interface. The advantage of the VOF method is that it conserves mass. The main disadvantage of the VOF method is that the computation of the normal and curvature are inaccurate since α is a discontinuous function. This can result in parasitic currents (Lafaurie et al., 1994), which will be referred to as nonphysical velocities in this dissertation.

To maintain a sharp interface of the volume fraction field, various techniques have been developed to reconstruct the interface such as the simple line interface calculation (SLIC) (Noh and Woodward, 1976), Young's VOF (Youngs, 1982), compressive interface capturing for arbitrary meshes (CICSAM) (Ubbink and Issa, 1999) and piecewise linear interface calculation (PLIC) (Renardy and Renardy, 2002).

The aim of the CLSVOF method is to combine the strengths of both the LS and VOF method. It defines the interface as the zero level set of ϕ. A translation is done through the Heaviside function to represent α in terms of ϕ. The new method combines both the ability of the LS method to correctly compute curvature from a smooth function and the VOF mass conservation property. The CLSVOF can be computationally expensive with the need to re-initialize the distance function and various studies have been done

on ways to re-initialize ϕ to keep it smooth (Cho et al., 2011, Sussman and Fatemi, 1999, Sussman et al., 1998).

The VOF method is used in this study because it solves for the simulated motion of the particle-fluid interface from a fundamental level at a reasonable computational cost and the LS method on its own does not conserve mass. In the section to follow, the VOF method will be discussed in detail.

1.2.4 Volume-Of-Fluid method

In the VOF method an Eulerian description is used for both phases and the solution process performed on an Eulerian or arbitrary Eulerian-Lagrangian grid. A volume averaged indicator function $\alpha(\mathbf{x}, t)$ is assigned for each computational cell and advected through space by the velocity obtained from solving the Navier-Stokes equations. The two main numerical challenges with the VOF method are computing correctly the curvature, and nonphysical coalescence that occurs when interfaces are within a mesh cell spacing.

The curvature computation is a result of the surface tension model used. In this study this model is the Continuum Surface Force (CSF) formulation of Brackbill et al. (1992). The surface tension force which would otherwise be obtained from jump conditions across the interface is reformulated as a volume force and introduced into the momentum equation as a body force. Problems arise in the computation of the curvature. Due to the calculation of second-order spatial derivatives of the step function, the VOF method poorly estimates the curvature (Cummins et al., 2005). The applicability of the CSF method to surface tension-dominated flows is limited because of the generation of nonphysical velocities (Denner et al., 2014, Harvie et al., 2006, Lafaurie et al., 1994) that do not decrease with an increase in the mesh refinement (Harvie et al., 2006).

The static sphere in a two-dimensional square with negligible gravity is a common test used to verify that the surface tension force has been correctly calculated. In the ideal situation all the terms of the Navier-Stokes equation involving velocity and gravity would be zero, leaving the pressure gradient to balance the surface tension forces. But in the case of the CSF method the curvature is incorrectly calculated, leaving the pressure gradient unable to balance the surface tension force. Some of the velocity terms are required to restore the balance but at the cost of introducing nonphysical velocities whose magnitude can introduce oscillations to the solution.

Of the different techniques that have been used in the literature to reduce the magnitude of the nonphysical velocities, smoothing techniques are the most popular and they differ

in the smoothing kernels used. An example is the work of Cummins et al. (2005). In this study a diffusive type smoother as implemented by Heyns et al. (2011) is used with a variable user defined coefficient to specify the number of cells to smear the interface over.

Studies of particle interactions using the VOF method include those by Tomiyama et al. (1993) who used the VOF method to study the rising of a single bubble in a stationary fluid with the aim of analysing the feasibility of using DNS. They noted that in the case of skirted and spherical cap bubbles, the bubble interface was broken because the lower and upper droplet interfaces were within a single cell. Their conclusion was that a finer computational mesh was needed to simulate skirted and spherical cap bubbles. Lin et al. (1996) were among the first authors to study the flow in a bubble column reactor using a two-dimensional model based on the VOF method. They noted that this method provides a simple and economical way to study individual bubbles. Their model however did not account for bubble collision. Delnoij et al. (1997b) used the VOF method to study the dynamics of multiple deformable gas bubbles. In their subsequent study, Delnoij et al. (1998) studied the rise, formation and coalescence of skirted spherical cap bubbles in liquids and included a CSF model for the surface tension force.

Nikolopoulos et al. (2009b) studied a non-central binary collision between equal sized droplets using a VOF method with adaptive mesh refinement to correctly model the gas-liquid interface region. Nikolopoulos et al. (2012) again used the VOF methodology to study the impact that the Weber number has on the outcome of a binary collision between unequal sized droplets. Adaptive mesh refinement was used to resolve the thin film. Liu et al. (2013) used an axi-symmetric grid to simulate numerically the head-on collision of binary gel propellant droplets using the VOF method, and investigated the coalescence of the droplets. Albadawi et al. (2014) studied the free rise, collision and rebound of an isolated bubble on a wall using axi-symmetric and three-dimensional simulations. Their finding was that a refined mesh close to the solid surface provided accurate quantitative results.

When two particles collide the surrounding fluid is trapped in a thin film between them. This thin film is at a smaller length scale compared to that of the particles. In the study of Tomiyama et al. (1993) the skirted and spherical cap bubble interfaces were broken because the interfaces were too close to each other. There was not enough resolution provided for the VOF method to capture the small fluid velocities in order to accurately capture the interface. To resolve the existence of this thin film later studies opted to use very fine computational grids in order to resolve the small scale fluid velocities (Albadawi et al., 2014, Nikolopoulos et al., 2009b, 2012).

Researchers that have reported this inability of the VOF method to accurately capture interfaces that are within a single mesh cell spacing without artificially merging them include Coyajee and Boersma (2009), Gauer et al. (2009), van Sint Annaland et al. (2005).

Adaptive mesh refinement at the particle-fluid interface has been the solution of choice with the increase in computational power when simulating particle-particle interactions with the VOF method. Even with a single particle the mesh resolution required is very high due to the thickness of the thin film that must be resolved. A finer computational grid would provide more cells between interfaces such that the interfaces will not be within a mesh cell spacing for the artificial merging to take place. This is not the approach of the present study, as adaptive mesh refinement can become computationally expensive when the particle numbers increase and storage requirements become a problem.

Coyajee and Boersma (2009) proposed a multiple marker method in the framework of the CLSVOF method to simulate droplet impact without artificial coalescence. The method used multiple LS functions corresponding to multiple volume fraction fields to represent individual droplets. Validation was done using a droplet falling under the influence of gravity and impacting an interface. The method managed to successfully prevent the droplet from automatically coalescing into the liquid layer. Kwakkel et al. (2012) improved this method to accommodate the simulation of a large number $O(10^2 - 10^3)$ of droplets dispersed in a turbulent fluid.

Nikolopoulos et al. (2009a) studied a central binary collision of equal droplets on an axi-symmetric grid using a two indicator VOF method with the aim of preserving the identity of each droplet up to the point of coalescence. Adaptive mesh refinement was used as well to accurately capture the region around the interface. Focke et al. (2013) used a DNS formulation based on a VOF method together with experiments to study the binary collision of unequal sized droplets – a small droplet with high viscosity and a large droplet with low viscosity. Their experimental results showed a delay in the coalescence of the two droplets. They extended their VOF method to include the multiple marker VOF technique of Coyajee and Boersma (2009) to temporarily delay the coalescence in the simulation. This method was also introduced in the framework of the LS method by Balcázar et al. (2015), with the aim of preventing nonphysical coalescence.

The multiple marker method is simple and straightforward to implement computationally, and simulates non-coalescing collisions without the need for excessively refined grids. Its main disadvantage is that it inhibits coalescence even when this should result from the underlying physics (Coyajee and Boersma, 2009). Thus, to correctly model both coalescence and rebound with this method, a surface thin film model as suggested

by Unverdi and Tryggvason (1992) and Nobari et al. (1996) that determines the outcome of the collision is required.

Introducing this surface thin model would result in a less computationally intensive DNS method since the thin film model would be used to resolve the flow between the particles instead of resolving the thin film explicitly.

1.2.5 Surface thin film model

The surface thin film model suggested here is based on the Reynolds equation from lubrication theory. Lin and Slattery (1982) and Chen et al. (1984) were among the first to develop a hydrodynamic theory of a thinning film between a small bubble approaching a liquid-liquid interface based on the Reynolds equation from lubrication theory.

Yeo et al. (2003) demonstrated the feasibility of applying lubrication theory to study film drainage by adopting a simplified lubrication theory approach to model the film drainage between surfactant coated colliding droplets approaching at a constant velocity. Zhang and Law (2011) also noted that lubrication theory for continuum flow is applicable in solving the gas flow in the thin film region during early stages of coalescence by theoretically analysing the binary head on collision of droplets in a gaseous environment.

Chen et al. (1984) extended the theory developed by Lin and Slattery (1982) by including London-van der Waals forces to determine the rate of thinning and calculated the film drainage time. In their derivation the interfaces were assumed to be tangentially immobile with a planar interface shape. Tsekov and Ruckenstein (1994) noted that this assumption of plane parallel interfaces in the Reynolds equation assumption gives it the disadvantage of not being capable of modelling interfaces that form a dimple.

In their development of a hydrodynamic model based on lubrication theory to study deformable interfaces at nanometre separation distances, Manica et al. (2008) ignored the dis-joining pressure due to van der Waals forces. Malavé et al. (2009) ignored London-van der Waals forces and concluded that inclusion of the forces in the model does not assist in dimple formation. London-van Der Waals forces are ignored in the present study and the assumption of locally plane parallel interfaces is adopted. Although the van der Waals forces play an important role on thin film thinning, they are only applicable when the thin film is in the nanometre scale range (Pan et al., 2008).

Studies that have demonstrated approaches of solving the Reynolds equation include Benjamin Steinhaus and Shen (2006) who took into account both dimpling and van der Waals forces to calculate the rate of film thinning with the corresponding film drainage time of a droplet approaching a solid surface. The numerical solution was obtained by

solving for the thin film thickness by providing an initial thin film estimate and final film thickness. They noted that the film thickness had an exponential decay and coalescence was independent of their initial estimate.

Other studies include Jiang and James (2006) who used an axisymmetric VOF method to study the effect of the van der Waals force on the head-on collision of equal sized droplets. A modified Navier-Stokes equation that incorporated the van der Waals forces was solved with a symmetry boundary condition imposed on the volume fraction field to manipulate the instant of coalescence. Kwakkel et al. (2013) who applied the method of Zhang and Law (2011) coupled to a CLSVOF method to study the collision in droplet laden flow. Quan (2012) used a DNS approach based on the front tracking method to study a deformable droplet falling through a fluid to approach a planar solid wall, their results of the thinning of the thin film agreed well with results from lubrication theory.

Mason et al. (2014) studied the interaction between a droplet and an interface driven by buoyancy. Their model coupled the CSF method in the framework of a LS method to a lower dimensional thin film equation based on lubrication theory with assumed negligible electrostatic forces. A solution was obtained by solving for the pressure in the thin film region given the time variation in velocities obtained from the flow simulation, and coupling this back to the flow solution (Mason et al., 2012). The numerical results were compared to the experiment of Pan et al. (2008) but the obtained critical film thickness was a considerable underestimate of the actual experimental estimate.

A comprehensive numerical method based on solving the Reynolds equation independently for the film thickness given the pressure obtained from the Navier-Stokes equations and an initial thin film thickness estimate is used in this study. This enables the numerical model to provide an estimate of the drainage time. It is the view of the present study that solving for the film thickness evolution given the pressure is more advisable as the interface-thickness boundary velocity is very small compared with the velocities present in the fluid.

1.3 Motivation

The importance of particle-particle interactions (which result in coalescence or rebound) in industrial applications has been highlighted. Coalescence greatly affects the particle size distribution in reactors, thereby affecting the overall operating conditions. But it has shortcomings in relation to computationally modelling coalescence.

1.3.1 Limitations of current models

Of the various multiphase flow modelling techniques that were considered, Euler-Euler and Euler-Lagrange models were found lacking in that they require empirical correlations when studying coalescence. Using these models does not provide any fundamental insights into the coalescence process since the correlations are determined from experiments and phenomenological models. These methods do not offer a generalized way to model coalescence.

Interface tracking methods and interface capturing methods have been reviewed. In interface tracking, the description of the interface is done by computational elements and the need for mesh movements and information storage on each computational element can be computationally expensive. During particle-particle interaction large deformations and topology changes occur and mesh entanglement make it difficult to capture large topology changes. The method requires explicit interface merging descriptors when modelling coalescence. Thus for these reasons interface tracking has been ruled out for use in this study.

The interface capturing VOF method provides a DNS approach to modelling particle-particle interactions. Although it is straightforward to implement computationally it has two major drawbacks: firstly the inability to correctly model the surface tension force, and secondly the inherent nonphysical coalescence that results when two particles are very close to each other.

To resolve the interface correctly, most studies of particle-particle interaction using the VOF method have resorted to using adaptive mesh refinement to provide enough resolution to capture the dynamics of the thin liquid film that forms. This is computationally expensive as re-meshing and mesh updates are required between successive time steps. Due to this inability to resolve small scale flow variables, inherent to the VOF method is nonphysical coalescence. There is a need to prevent the nonphysical merging of interfaces so that particle rebound can be modelled correctly.

The multiple marker VOF method presents a solution that prevents the artificial merging of interfaces; however, its major disadvantage is that it inhibits coalescence even when the particles should physically coalesce. Existing coalescence models which use film drainage models are based on experimental observations of coalescence frequencies to give an estimate of drainage time. Previous computational studies that have accounted for coalescence have been limited to using the experimentally determined drainage time in their simulations to obtain the correct physical behaviour.

Solving the Reynolds equation by prescribing velocity boundary conditions as in the approach of Mason et al. (2012) is fraught with difficulty given the difference in scale between the particles and the film. The numerical results only demonstrated one test case out of the four sets of experiments, leaving in doubt the predictive power of their model for a wide variety of collision outcomes. A model that can be proved to work for all of the data available is required.

1.3.2 Need for additional research

The surface tension force plays an important role in the modelling of particle-particle interactions. Although the existence of nonphysical velocities which arise during its calculation has been well documented, very complex methods have been developed to reduce their magnitudes. Thus, given the VOF method's inability to accurately model the curvature due to the volume fraction field discontinuity, there is a need to implement a solution that will improve the curvature computation.

This should reduce the influence of nonphysical velocities in limiting interface oscillations so that they do not affect the modelling of the collision event. Such solutions should not increase the complexity of the model and should be relatively straightforward to implement.

The film drainage theory of coalescence is used to describe the collision event between particles in this study. Most previous studies of particle coalescence have focused on either resolving the three-dimensional flow in the thin film region using extremely high mesh densities, or on artificially merging the particles at a pre-specified time. Limited and inconclusive attempts have so far been made to predict the film drainage process by modelling the thin film as a separate entity. The thin liquid film that forms during the film drainage stage introduces complexity since the resolution at very small scales of the flow velocity and pressure are required to study the dynamics of the film which determines the outcome of the collision. The premise of this dissertation is that thin film equations, similar to those employed in lubrication theory, could be derived to model the film drainage process explicitly but without the need for excessive mesh resolution.

With this approach, the numerical multiphase flow techniques used to study particle-particle interaction would be able to correctly resolve the particle-fluid interface from the moment of impact up to the moment of either coalescence or rebound.

1.4 Research objectives

The objective of this study is to develop and use a DNS approach based on a smoothed VOF method to model particle-particle interactions in a dispersed multiphase flow at a fundamental level, and employing a surface thin film model, to drastically reduce the computational effort required. The study is restricted to gas-liquid systems where particles could either be bubbles or droplets; rigid particles are not considered. The specific objectives are as follows:

1. To study the effect of smoothing of the volume fraction field on reducing the magnitude of nonphysical velocities
    - To develop a smoothed VOF method based on a diffusive type smoother of the volume fraction field and implement into the OpenFOAM® framework
    - To validate the diffusive type smoother using a static droplet against the analytic Young-Laplace equation
    - To utilize the validated smoothed VOF method as a basis to study particle-particle interactions
2. To study nonphysical coalescence inherent in the VOF method
    - To develop a comprehensive Smoothed Multiple Marker VOF (SMMVOF) numerical method based on the smoothed VOF method to prevent nonphysical coalescence
    - To implement the SMMVOF method into the OpenFOAM® framework
    - To test the SMMVOF method against experimental results of a droplet falling under the influence of gravity onto a liquid-liquid interface
    - To utilize the SMMVOF method as a basis for modelling particle-particle interaction
3. To study particle coalescence based on the film drainage theory
    - To develop a surface thin film model to couple to the SMMVOF method
    - To validate the model against experimental results of the head-on collision of hydrocarbon droplets

1.5 Dissertation outline

The remainder of the dissertation is structured as follows. Chapter 2 introduces in detail the VOF method in the context of the Finite Volume Method (FVM) of discretization.

The Navier-Stokes equations for an incompressible viscous multiphase Newtonian fluid undergoing laminar and isothermal three-dimensional flow are summarized. In Chapter 3 the SMMVOF method is introduced as a means for preventing the nonphysical coalescence inherent in the VOF method. The derivation of a surface thin film model that calculates the thickness of the thin film between two particles is also presented. The next chapter, Chapter 4 presents the numerical results. The diffusive type smoother introduced in Chapter 2 is tested using a static sphere test case in a two-dimensional box with negligible gravity. The SMMVOF method presented in Chapter 3 is also tested by simulating a droplet falling under the influence of gravity onto a liquid-liquid interface. The surface thin film model presented in Chapter 3 is validated by simulating the impact of hydrocarbon droplets that result in either coalescence or rebound and the results compared to experiments. Chapter 5 is the concluding chapter, summarizes the highlights of the previous four chapters, gives recommendations for future work, and a conclusion.

Chapter 2

Multiphase flow modelling

Different numerical modelling techniques as discussed in Chapter 1 are used to model multiphase flow. A continuum approach with volume averaging (Whitaker, 1973) is used in this study. The procedure of Wörner (2003) is used to derive the model equations which are the Navier-Stokes equations for an incompressible viscous multiphase Newtonian fluid undergoing laminar and isothermal three-dimensional flow.

The outline of this chapter is as follows: In Section 2.1 the principles of volume averaging are outlined. The conservation equations[1] are stated for individual phases separated by an interface in Section 2.2. It is shown in Section 2.3 that summation of the governing equations in each phase gives the equations that govern a two-phase mixture. The VOF method is introduced to provide closure for the governing equations in Section 2.4 and the transport equation for the volume fraction is deduced. Section 2.5 introduces the CSF method of Brackbill et al. (1992) to compute the surface tension force.

Sections 2.6 and 2.7 focus on the discretization and the numerical solution procedure of the governing equations. Section 2.6 discusses the discretization of the solution domain. In Section 2.7 the governing equations are discretized using Gauss' divergence theorem. The individual terms of the governing equations are grouped into convective, diffusive and source terms. An Euler time integration is used with different differencing schemes chosen to ensure boundedness and stability of the solution. Section 2.8 derives the pressure equation from the semi-discretized equations and the solution algorithm is outlined. Implementation in the open source software OpenFOAM® is discussed in Section 2.9.

[1] It is assumed that the reader is familiar with conservation of mass and momentum equations and a derivation is not given.

2.1 Volume averaging

Let us consider two immiscible fluids in a domain $\Omega \subset \mathbb{R}^3$ decomposed into two time dependent ($\Omega = \Omega_1(t) \cup \Omega_2(t)$), and non-overlapping ($\Omega_1 \cap \Omega_2 = \varnothing$) sub-domains. Let $\partial\Omega$ denote the rigid boundary of Ω and $\Gamma = \Gamma(\mathbf{x}, t)$ the interface separating the two fluids which is assumed to be thin and massless. Define an indicator function $X_k = X_k(\mathbf{x}, t)$ (where $k \in \{1, 2\}$) at a position in Ω by

$$X_k(\mathbf{x}, t) = \begin{cases} 1 & \mathbf{x} \in \Omega_k(t), \\ 0 & \text{otherwise.} \end{cases} \tag{2.1}$$

The indicator functions are related through the condition

$$X_1 + X_2 = 1. \tag{2.2}$$

Let V denote the volume of Ω, which is constant over time, and V_k the volume of fluid in Ω_k. The volume average of the indicator function gives the volume fraction $\alpha_k(\mathbf{x}, t)$ of phase k; that is,

$$\alpha_k = \frac{1}{V} \int_V X_k(\mathbf{x}, t) dV \tag{2.3}$$

$$= \frac{V_k}{V}. \tag{2.4}$$

The compatibility of α_k follows from (2.2):

$$\alpha_1 + \alpha_2 = 1. \tag{2.5}$$

Let Ψ_k denote a general scalar or vector quantity. The volume averaged values over Ω and Ω_k , $\langle \Psi_k \rangle$ and $\langle \Psi_k \rangle^k$ are defined by

$$\langle \Psi_k \rangle = \frac{1}{V} \int_V \Psi_k X_k(\mathbf{x}, t) \; dV, \tag{2.6}$$

and

$$\langle \Psi_k \rangle^k = \frac{1}{V_k} \int_V \Psi_k X_k(\mathbf{x}, t) \; dV. \tag{2.7}$$

It follows that (2.6) and (2.7) are linearly related through (2.4):

$$\langle \Psi_k \rangle = \alpha_k \langle \Psi_k \rangle^k. \tag{2.8}$$

2.2 Single-phase volume averaged equations

The equations of conservation of mass and momentum that govern the flow in Ω_k are given by

$$\frac{\partial \rho_k}{\partial t} + \nabla \cdot (\rho_k \mathbf{u}_k) = 0 \tag{2.9}$$

and

$$\frac{\partial (\rho_k \mathbf{u}_k)}{\partial t} + \nabla \cdot (\rho_k \mathbf{u}_k \mathbf{u}_k) = \nabla \cdot \boldsymbol{\tau}_k + \mathbf{f}_k. \tag{2.10}$$

Here $\rho_k = \rho_k(\mathbf{x}, t)$ is the density, $\mathbf{u}_k = \mathbf{u}_k(\mathbf{x}, t)$ is the velocity, $\mathbf{f}_k$ represents body forces acting on the fluid and assumed to be gravity, so that

$$\mathbf{f}_k = \rho_k \mathbf{g}. \tag{2.11}$$

Here $\mathbf{g}$ is the gravitational acceleration. $\boldsymbol{\tau}_k$ is the stress tensor; assuming that the fluids are Newtonian, the stress is a linear function of the rate of deformation and can be decomposed into pressure and viscous terms according to

$$\boldsymbol{\tau}_k = -p_k \mathbf{I} + 2\mu_k \mathbf{E}_k. \tag{2.12}$$

$\mathbf{I}$ is the identity tensor, $p_k = p_k(\mathbf{x}, t)$ is the pressure, $\mu_k = \mu_k(\mathbf{x}, t)$ is the dynamic viscosity, and $\mathbf{E}_k$ is the rate of deformation tensor, given by

$$\mathbf{E}_k = \frac{1}{2}(\nabla \mathbf{u}_k + (\nabla \mathbf{u}_k)^T) \tag{2.13}$$

where $(\cdot)^T$ is the transpose operator.

Applying the theorems of averaging (A.1) and (A.3) (Whitaker, 1973) to the mass conservation equation (2.9), we obtain

$$\frac{\partial \alpha_k \rho_k}{\partial t} + \nabla \cdot (\alpha_k \rho_k \langle \mathbf{u}_k \rangle^k) = -\frac{1}{V} \int_{\Gamma \cap V} \rho_k (\mathbf{u}_k - \mathbf{v}_k) \cdot \mathbf{n}_k \, dA. \tag{2.14}$$

The term on the righthand side is a result of averaging and represents mass transfer through phase change, $\mathbf{v}_k$ is the velocity of the interface, $\mathbf{n}_k$ is the outward unit normal vector to the interface, and $\Gamma \cap V$ is the part of the interface inside the volume V. In the absence of phase change the term on the righthand side is zero and the conservation of mass equation reduces to

$$\frac{\partial \alpha_k \rho_k}{\partial t} + \nabla \cdot (\alpha_k \rho_k \langle \mathbf{u}_k \rangle^k) = 0. \tag{2.15}$$

Substitution of (2.12) and (2.13) into (2.10) and averaging the momentum equation with (A.1)-(A.5) results in

$$\frac{\partial(\alpha_k\rho_k\langle\mathbf{u}_k\rangle^k)}{\partial t} + \nabla\cdot(\alpha_k\rho_k\langle\mathbf{u}_k\rangle^k\langle\mathbf{u}_k\rangle^k) = -\nabla(\alpha_k\langle p_k\rangle^k) + \alpha_k\rho_k\mathbf{g} + \frac{1}{V}\int_{\Gamma\cap V}\tau_k\cdot\mathbf{n}_k\,dA + \nabla\cdot\mu_k\left[\nabla(\alpha_k\langle\mathbf{u}_k\rangle^k) + \left[\nabla(\alpha_k\langle\mathbf{u}_k\rangle^k)\right]^T\right] \quad (2.16)$$

where the last term on the first line of equation (2.16) represents momentum transfer across the interface.

2.3 Two-phase mixture volume averaged equations

Equations (2.15) and (2.16) govern the flow in each domain Ω_k. To obtain equations that govern the flow in Ω the equations in Ω_k are summed. Summing the continuity equation (2.15),

$$\sum_{k=1}^{2}\left[\frac{\partial\alpha_k\rho_k}{\partial t} + \nabla\cdot(\alpha_k\rho_k\langle\mathbf{u}_k\rangle^k)\right] = 0, \quad (2.17)$$

and defining a mixture density and centre of mass velocity by

$$\rho_m = \alpha_1\rho_1 + \alpha_2\rho_2 \quad (2.18)$$

and

$$\mathbf{u}_m = \frac{1}{\rho_m}\sum_{k=1}^{2}\alpha_k\rho_k\langle\mathbf{u}_k\rangle^k, \quad (2.19)$$

(2.17) can be rewritten as

$$\frac{\partial\rho_m}{\partial t} + \nabla\cdot(\rho_m\mathbf{u}_m) = 0. \quad (2.20)$$

Summing the momentum equation (2.16),

$$\sum_{k=1}^{2}\left[\frac{\partial(\rho_k\alpha_k\langle\mathbf{u}_k\rangle^k)}{\partial t}\right] + \sum_{k=1}^{2}\left[\nabla\cdot(\rho_k\alpha_k\langle\mathbf{u}_k\rangle^k\langle\mathbf{u}_k\rangle^k)\right] = \sum_{k=1}^{2}\left[-\nabla(\alpha_k\langle p_k\rangle^k)\right] + \sum_{k=1}^{2}\nabla\cdot\left(\mu_k\left[\nabla(\alpha_k\langle\mathbf{u}_k\rangle)^k + \left[\nabla(\alpha_k\langle\mathbf{u}_k\rangle^k)\right]^T\right]\right) + \sum_{k=1}^{2}[\rho_k\alpha_k\mathbf{g}] + \sum_{k=1}^{2}\left[\frac{1}{V}\int_{\Gamma\cap V}\tau_k\cdot\mathbf{n}_k\,dA\right]. \quad (2.21)$$

This reduces to

$$\frac{\partial(\rho_m \mathbf{u}_m)}{\partial t}+\nabla\cdot\left(\rho_m \mathbf{u}_m \mathbf{u}_m+\frac{\alpha_1\rho_1\alpha_2\rho_2}{\rho_m}\left(\langle\mathbf{u}_2\rangle^2-\langle\mathbf{u}_1\rangle^1\right)\left(\langle\mathbf{u}_2\rangle^2-\langle\mathbf{u}_1\rangle^1\right)\right)=-\nabla(\alpha_1 p_1+\alpha_2 p_2)$$
$$+\nabla\cdot\mu_m\left(\nabla\mathbf{u}_m+(\nabla\mathbf{u}_m)^T\right)+\nabla\cdot\left[\rho_1\alpha_2\mu_2\left(\nabla\frac{\alpha_1}{\rho_m}(\langle\mathbf{u}_2\rangle^2-\langle\mathbf{u}_1\rangle^1)+\left(\nabla\frac{\alpha_1}{\rho_m}(\langle\mathbf{u}_2\rangle^2-\langle\mathbf{u}_1\rangle^1)\right)^T\right)\right]$$
$$+\nabla\cdot\left[\rho_2\alpha_1\mu_1\left(\nabla\frac{\alpha_2}{\rho_m}(\langle\mathbf{u}_2\rangle^2-\langle\mathbf{u}_1\rangle^1)+\left(\nabla\frac{\alpha_2}{\rho_m}(\langle\mathbf{u}_2\rangle^2-\langle\mathbf{u}_1\rangle^1)\right)^T\right)\right]+\sum_{k=1}^{2}\left[\frac{1}{V}\int_{\Gamma\cap V}\tau_k\cdot\mathbf{n}_k\,dA\right]$$
$$+\rho_m\mathbf{g}, \quad (2.22)$$

where the mixture viscosity μ_m is given by

$$\mu_m=\alpha_1\mu_1+\alpha_2\mu_2. \quad (2.23)$$

The second last term of (2.22) can be evaluated using the jump conditions across the interface. The pressure and viscous forces at the interface are in equilibrium with surface tension forces, so that

$$\sum_{k=1}^{2}\left[\frac{1}{V}\int_{\Gamma\cap V}\tau_k\cdot\mathbf{n}_k\,dA\right]=\frac{1}{V}\int_{\Gamma\cap V}(\sigma\kappa\mathbf{n}+\nabla_s\sigma)\;dA. \quad (2.24)$$

Here σ is the surface tension coefficient, κ is the signed curvature

$$\kappa=-\nabla\cdot\mathbf{n}, \quad (2.25)$$

and ∇_s is the gradient in surface coordinates.

2.4 VOF method

In the previous section the governing transport equations for a viscous multiphase Newtonian fluid were given. It was noted that the equations governing the motion can be combined to obtain equations for an effective fluid. The governing equations for the VOF method are similar to those obtained above.

The system of equations derived above is underdetermined and certain relations are needed to close the system. Assume that the density, viscosity and surface tension coefficient are known and that the latter two are constant. Assuming a homogeneous flow model by neglecting relative motion, the fluid velocity and pressure of each phase is continuous across the interface, we have

$$\langle\mathbf{u}_1\rangle^1=\langle\mathbf{u}_2\rangle^2=\mathbf{u}_m$$

and

$$\langle p_1 \rangle^1 = \langle p_2 \rangle^2 = p_m.$$

The momentum equation (2.22) reduces to

$$\frac{\partial(\rho_m \mathbf{u}_m)}{\partial t} + \nabla \cdot (\rho_m \mathbf{u}_m \mathbf{u}_m) = -\nabla p_m + \mu_m \nabla \cdot \left(\nabla \mathbf{u}_m + (\nabla \mathbf{u}_m)^T\right) + \rho_m \mathbf{g} + \frac{1}{V} \int_{\Gamma \cap V} \sigma \kappa \mathbf{n} \, dA. \tag{2.26}$$

The averaged volume fractions of each fluid can be written in terms of a single volume fraction that is averaged by the cell volume. Let $\alpha_1 = \alpha$; then from equation (2.5) we can write $\alpha_2 = 1 - \alpha$. The mathematical description of α, viz.

$$\alpha(\mathbf{x}, t) = \begin{cases} 1 & \text{fluid 1}, \\ 0 & \text{fluid 2}, \\ 0 < \alpha < 1 & \text{interface}, \end{cases} \tag{2.27}$$

is similar to the description of the indicator function (2.1). Writing the mixture density (2.18) and viscosity (2.23) as

$$\rho_m = \alpha \rho_1 + (1 - \alpha) \rho_2 \tag{2.28}$$

and

$$\mu_m = \alpha \mu_1 + (1 - \alpha) \mu_2 \tag{2.29}$$

and substituting into (2.20) with the assumption that the densities ρ_1 and ρ_2 are constant (resulting in incompressible flow $\nabla \cdot (\rho_m \mathbf{u}_m) = 0$), we obtain the equation for the volume fraction

$$\frac{\partial \alpha}{\partial t} + \mathbf{u}_m \cdot \nabla \alpha = 0 \tag{2.30}$$

which describes the evolution of the interface.

Henceforth the subscript m will be dropped. The governing Navier-Stokes equations for an incompressible viscous multiphase Newtonian fluid undergoing laminar and isothermal three-dimensional flow in the framework of the VOF method are given by:

$$\nabla \cdot (\rho \mathbf{u}) = 0 \tag{2.31}$$

$$\frac{\partial(\rho \mathbf{u})}{\partial t} + \nabla \cdot (\rho \mathbf{u} \mathbf{u}) = -\nabla p + \nabla \cdot (\mu \nabla \mathbf{u}) + \rho \mathbf{g} + \frac{1}{V} \int_{\Gamma \cap V} \sigma \kappa \mathbf{n} \, dA \tag{2.32}$$

$$\rho = \alpha \rho_1 + (1 - \alpha) \rho_2 \tag{2.33}$$

$$\mu = \alpha \mu_1 + (1 - \alpha) \mu_2 \tag{2.34}$$

$$\frac{\partial \alpha}{\partial t} + \nabla \cdot (\alpha \mathbf{u}) = 0 \tag{2.35}$$

2.5 Surface tension modelling with CSF

In the previous sections the interface separating the two fluids was considered thin and massless, and jump conditions were used to relate properties across the interface. The surface tension relationship was obtained by using the stress balance at the interface. In this section the CSF method (Brackbill et al., 1992) is used to compute the surface tension force.

In the CSF method the assumption of a thin interface is replaced by an interface with a finite thickness where there is a continuous transition of the volume fraction field α. The surface tension force has a continuous three-dimensional effect across the interface and thus the interfacial jump conditions are not required. The surface force is reformulated as a volume force (Brackbill et al., 1992) that is introduced into the momentum equation as a body force $\mathbf{f}_\sigma$; that is,

$$\mathbf{f}_\sigma = \sigma\kappa\mathbf{n}\delta_s, \tag{2.36}$$

here δ_s is the surface delta function that restricts the surface tension force to the interface region and $\mathbf{n}$ the outward unit normal at the interface is given by

$$\mathbf{n} = \frac{\nabla\alpha}{|\nabla\alpha|}. \tag{2.37}$$

The term $\mathbf{n}\delta_s$ can be replaced by $\nabla\alpha$ to give the surface tension force as

$$\mathbf{f}_\sigma = \sigma\kappa\nabla\alpha. \tag{2.38}$$

The applicability of the CSF method to surface tension dominated flows is limited because of the generation of nonphysical velocities (Denner et al., 2014, Harvie et al., 2006, Lafaurie et al., 1994). These velocities scale with surface tension and viscosity (Lafaurie et al., 1994) and occur in the region of the interface and could be a result of either an imbalance of the surface tension force and pressure gradient or an inaccurate curvature calculation. The curvature calculation involves computing the first derivatives of the volume fraction, which is a step function.

It has been shown that the magnitude of the nonphysical velocities does not decrease with a decrease in mesh spacing or a decrease in the time step (Harvie et al., 2006) and for some situations the currents can dominate the solution and lead to interface break-up.

Lafaurie et al. (1994) suggested the use of a smoothed volume fraction field α^s to reduce the magnitude of the nonphysical velocities. A diffusive type smoother (Heyns et al., 2011) is used in this study with the equation for the smoothed volume fraction field

given by

$$\frac{\partial \alpha^s}{\partial t} = \nabla^2 \left(\eta \alpha^s\right) \tag{2.39}$$

where η is the smoothing coefficient that determines the distance that the smoothing is performed over. The smoothed volume fraction field α^s is always reinitialized to the unsmoothed volume fraction field α.

Here we extend the formulation of Heyns et al. (2011) above to be independent of the time step size, and to smooth over a given number of mesh cells rather than a given distance. This prevents the need to tune the smoothing parameter for each case considered. Therefore, we replace equation (2.39) with

$$\alpha^s - \alpha = \nabla^2(\eta \alpha^s) \tag{2.40}$$

where the coefficient η is given by

$$\eta = \chi \left(\mathbf{A}_f \cdot \delta\right)^2, \tag{2.41}$$

and χ ($\chi \geq 0$) is a user input that specifies the number of cells over which the volume fraction field should be smoothed, $\mathbf{A}_f$ gives the normalized surface area vector and δ gives the distance between the cell centres of adjacent cells. The smoothed volume fraction field is used to calculate the curvature to give a smoothed curvature κ^s:

$$\kappa^s = -\nabla \cdot \left(\frac{\nabla \alpha^s}{|\nabla \alpha^s|}\right). \tag{2.42}$$

The smoothed surface tension force equivalently becomes

$$\mathbf{f}_\sigma^s = \sigma \kappa^s \nabla \alpha. \tag{2.43}$$

With smoothing the governing system of equations become

$$\nabla \cdot (\rho \mathbf{u}) = 0 \tag{2.44}$$

$$\frac{\partial (\rho \mathbf{u})}{\partial t} + \nabla \cdot (\rho \mathbf{u}\mathbf{u}) = -\nabla p + \nabla \cdot (\mu \nabla \mathbf{u}) + \rho \mathbf{g} + \sigma \kappa^s \nabla \alpha \tag{2.45}$$

$$\rho = \alpha \rho_1 + (1 - \alpha)\rho_2 \tag{2.46}$$

$$\mu = \alpha \mu_1 + (1 - \alpha)\mu_2 \tag{2.47}$$

$$\frac{\partial \alpha}{\partial t} + \nabla \cdot (\alpha \mathbf{u}) = 0 \tag{2.48}$$

$$\alpha^s - \alpha = \nabla^2 \left(\eta \alpha^s\right) \tag{2.49}$$

$$\kappa^s = \frac{\nabla \alpha^s}{|\nabla \alpha^s|} \tag{2.50}$$

Discretization follows the FVM on a collocated computational mesh with dependent variables defined at the cell centres. The discretization results in a system of algebraic equations that are solved iteratively using an implicit scheme with a pressure correction algorithm.

The basic idea behind the FVM method is the discretization of the integral form of the governing equations over a Control Volume (CV) with finite size (Versteeg and Malalasekera, 2007). This results in mass and momentum being conserved at the discrete level (Jasak, 1996). Since discretization is done directly on the physical domain no transformations are required. Discretization involves both the solution domain and the system of governing equations.

2.6 Discretization of solution domain

In the FVM method, discretization in space involves dividing it into a finite number of non-overlapping CVs to form a grid or computational mesh. Time t is discretized by splitting the time interval into finite time-steps Δt and marching forward with increments of $0 = t_1 < t_2 \ldots < \ldots < t_N = T$ with $\Delta t = t_n - t_{n-1}$. In general the CVs can have any polyhedral shape and their arrangement could either be structured or unstructured. Each CV has a central node where values of all the dependent variables are stored. Figure 2.1 shows a CV with central node P and bounded by faces with face centre f that are either shared between CVs or coincide with the boundary. The neighbouring CV has centroid N and the distance between P and N is given by δ. Each face has a face area vector $\mathbf{A}_f$ whose magnitude is given by the area of the face and whose direction is pointing outward normal to the face.

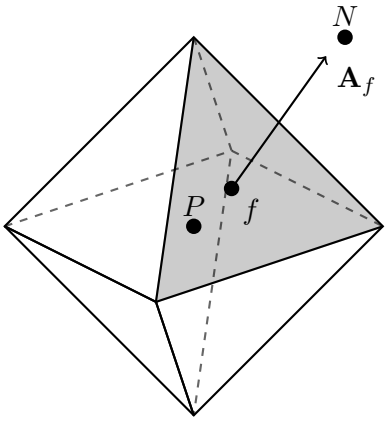

FIGURE 2.1: A general polyhedral shaped Control Volume in three dimensions

2.7 Discretization of governing equations

Discretization of the governing equations produces a system of algebraic equations defined on all points of the discretized domain. Equations (2.44)-(2.50) give the partial differential equations that govern multiphase dispersed flow. Consider again the CV in Figure 2.1. Let V_P denote its volume and ∂V_P its boundary surface. FVM requires that the equations (2.44)-(2.50) be satisfied over V_P around the point P in integral form (Jasak, 1996):

Momentum equation

$$\int_{t_n}^{t_n+\Delta t}\left[\frac{\partial}{\partial t}\int_{V_P}\rho\mathbf{u}\,dV+\int_{V_P}\nabla\cdot(\rho\mathbf{uu})\,dV-\int_{V_P}\nabla\cdot(\mu\nabla\mathbf{u})\,dV\right]dt= \int_{t_n}^{t_n+\Delta t}\left[-\int_{V_P}\nabla p\,dV+\int_{V_P}\rho\mathbf{g}\,dV+\int_{V_P}\sigma\kappa^{\mathbf{s}}\nabla\alpha\,dV\right]dt \tag{2.51}$$

VOF advection equation

$$\int_{t_n}^{t_n+\Delta t}\left[\frac{\partial}{\partial t}\int_{V_P}\alpha\,dV+\int_{V_P}\nabla\cdot(\alpha\mathbf{u})\,dV\right]dt=0 \tag{2.52}$$

Smooth VOF equation

$$\int_{t_n}^{t_n+\Delta t}\left[\int_{V_P}(\alpha^s-\alpha)\,dV\right]dt=\int_{t_n}^{t_n+\Delta t}\left[\int_{V_P}\nabla^2\left(\eta\alpha^s\right)\,dV\right]dt \tag{2.53}$$

Here $n=1\ ,\ \ldots\ ,\ N$. The terms in the above equations will be evaluated with the aid of Gauss' theorem. Consider a general vector or scalar $\mathbf{\Psi}$. Gauss' theorem translates volume integrals into surface integrals. Integration over the boundary is equivalent to integration over each individual face and summing all n contributions from each face (where n is the number of faces);

$$\int_{V_P}\nabla\cdot\mathbf{\Psi}dV=\oint_{\partial V_P}\mathbf{\Psi}\cdot d\mathbf{A} \tag{2.54}$$

$$=\sum_f\left(\int_f\mathbf{\Psi}\cdot d\mathbf{A}\right) \tag{2.55}$$

$$\approx\sum_f(\mathbf{A}\cdot\Psi)_f, \tag{2.56}$$

$$\int_{V_P} \nabla \boldsymbol{\Psi} dV = \oint_{\partial V_P} \boldsymbol{\Psi} d\mathbf{A} \tag{2.57}$$

$$= \sum_f \left(\int_f \boldsymbol{\Psi} d\mathbf{A} \right) \tag{2.58}$$

$$\approx \sum_f (\mathbf{A}\Psi)_f. \tag{2.59}$$

Here $(\cdot)_f$ denotes quantities evaluated at the face centre of the CV. The face centre values $\boldsymbol{\Psi}_f$,

$$\boldsymbol{\Psi}_f = a\boldsymbol{\Psi}_P + (1-a)\boldsymbol{\Psi}_N \tag{2.60}$$

are obtained by linear interpolation of the values at the centroid P ($\boldsymbol{\Psi}_P$) and the centroid of the neighbour N ($\boldsymbol{\Psi}_N$), where

$$a = \frac{fN}{\delta}, \tag{2.61}$$

is an interpolation ratio of the distance between the face centre f and N – denoted by fN – to the distance between P and N, δ. Unless stated otherwise linear interpolation is used in this study.

2.7.1 Momentum equation

To discretize the momentum equation the terms that are neither diffusive or convective will be grouped as a source term S,

$$S = (\rho \mathbf{g})_P + (\sigma \kappa^s \nabla \alpha)_P. \tag{2.62}$$

Assume that V_P remains constant in time. Then integration and differentiation can be interchanged in the first term of the momentum equation. Applying Gauss' divergence theorem (2.56) and (2.59) and taking into consideration (2.62), the volume integrals in the momentum equation can be written as

$$\begin{aligned} \int_{t_n}^{t_n+\Delta t} \left[\left(\frac{\partial \rho \mathbf{u}}{\partial t} \right)_P V_P + \sum_f \phi_f \mathbf{u}_f - \sum_f \mu_f \mathbf{A}_f \cdot (\nabla \mathbf{u})_f \right] dt = \\ - \int_{t_n}^{t_n+\Delta t} \sum_f \mathbf{A}_f p_f + \int_{t_n}^{t_n+\Delta t} \bar{S} V_P \, dt, \end{aligned} \tag{2.63}$$

where ϕ_f is the mass flux through the face defined as

$$\phi_f = \mathbf{A}_f \cdot (\rho \mathbf{u})_f, \tag{2.64}$$

and $\bar{S}$ is the average value of the source term over V_P which is linearized (Versteeg and Malalasekera, 2007) as

$$\bar{S}V_P = S_u + S_p \mathbf{u}_P. \tag{2.65}$$

The values of ρ_f, μ_f, $\mathbf{u}_f$ and $(\nabla \mathbf{u})_f$ are required to compute the mass flux through the face and for the momentum equation in a manner that conserves the mass. An upwind differencing scheme which determines the face values according to the flow direction is used to evaluate the velocities at the face centre $\mathbf{u}_f$. As mentioned, linear interpolation is used to compute the face centre values of μ_f, ρ_f and $(\nabla \mathbf{u})_f$ as in equation (2.60).

The term with the time derivative is evaluated using backward differencing with the assumption that the density is constant with respect to time in V_P. An implicit Euler method is used to obtain the discretization of the momentum equation

$$\begin{aligned} \frac{\rho_P \mathbf{u}_P^{m+1} - \rho_P \mathbf{u}_P^m}{\Delta t} + \frac{1}{V_P} \sum_f \phi_f^m \mathbf{u}_f^{m+1} - \frac{1}{V_P} \sum_f \mu_f \mathbf{A}_f \cdot (\nabla \mathbf{u})_f^{m+1} = \\ -\frac{1}{V_P} \sum_f S_f p_f^{m+1} + S_u^{m+1} + S_p^{m+1} \mathbf{u}_P^{m+1}, \end{aligned} \tag{2.66}$$

where $(\cdot)^{m+1}$ and $(\cdot)^m$ denote quantities evaluated at time $t_n + \Delta t$ and t_n respectively. The mass flux ϕ_f satisfies the continuity equation (2.44) in discrete form; that is,

$$\sum_f \phi_f^{m+1} = 0. \tag{2.67}$$

Equations (2.66) and (2.67) are used to obtain a solution for the velocity. The pressure is determined from the two equations via a pressure projection algorithm described in Section 2.8 below.

2.7.2 VOF advection equation

With the aid of Gauss' theorem, and following a similar procedure to that used for the momentum equation, the discretized form of the advection equation is

$$\begin{aligned} \int_{t_n}^{t_n+\Delta t} \left[\frac{\partial}{\partial t} \int_{V_P} \alpha \, dV + \int_{V_P} \nabla \cdot (\alpha \mathbf{u}) \, dV \right] dt = \\ \int_{t_n}^{t_n+\Delta t} \left(\frac{\partial \alpha}{\partial t} \right)_P V_P \, dt + \int_{t_n}^{t_n+\Delta t} \sum_f \alpha_f \mathbf{F}_f \, dt \end{aligned} \tag{2.68}$$

where $\mathbf{F}_f$ is the volumetric flux through the face given by

$$\mathbf{F}_f = \mathbf{A}_f \cdot \mathbf{u}_f. \tag{2.69}$$

Using the implicit Euler scheme the discretized volume fraction equation is

$$\frac{\alpha_P^{m+1} - \alpha_P^m}{\Delta t} + \frac{1}{V_P}\sum_f \alpha_f^{m+1}\mathbf{F}_f = 0. \tag{2.70}$$

2.7.3 Smooth VOF equation

Evaluating the volume integrals from (2.53) and using an implicit Euler scheme to evaluate the time integrals, the discretized smoothed volume fraction field equations are

$$\begin{aligned}\int_{t_n}^{t_n+\Delta t}\left[\int_{V_P}(\alpha^s - \alpha)\ dV - \int_{V_P}\left(\nabla^2(\eta\alpha^s)\right)\ dV\right]dt = \\ \alpha_P^{s(m+1)} - \alpha_P^m + \frac{1}{V_P}\sum_f \mathbf{A}_f\cdot(\nabla\eta\alpha^{s(m+1)})_f.\end{aligned} \tag{2.71}$$

2.8 Pressure equation

The system of equations above are non-linear and coupled by the velocity. Consider a semi-discretized form of the momentum equation with the pressure gradient,

$$\begin{aligned}\frac{\rho_P}{\Delta t}\mathbf{u}_P^{m+1} = \frac{\rho_P\mathbf{u}_P^m}{\Delta t} - \frac{1}{V_P}\sum_f \phi_f^m\mathbf{u}_f^{m+1} + \frac{1}{V_P}\sum_f \mu_f\mathbf{A}_f\cdot(\nabla\mathbf{u})_f^{m+1} + S_u^{m+1} \\ + S_p^{m+1}\mathbf{u}_P^{m+1} - \Delta t(\nabla p)_P.\end{aligned} \tag{2.72}$$

Combine all the terms on the RHS that are dependent on the velocity to form $H(\mathbf{u})$, given by

$$H(\mathbf{u}) = \frac{\rho_P\mathbf{u}_P^m}{\Delta t} - \frac{1}{V_P}\sum_f \phi_f^m\mathbf{u}_f^{m+1} + \frac{1}{V_P}\sum_f \mu_f\mathbf{A}_f\cdot(\nabla\mathbf{u})_f^{m+1} + S_u^{m+1} + S_p^{m+1}\mathbf{u}_P^{m+1}, \tag{2.73}$$

which is a function of the face interpolate of the velocity. Equation (2.72) now becomes

$$\frac{\rho_P}{\Delta t}\mathbf{u}_P^{m+1} = H(\mathbf{u}^{m+1}) - (\nabla p)_P^{m+1}. \tag{2.74}$$

Equation (2.74) gives the velocity at the centroid P of the control volume which can be interpolated to give the velocity at the face (2.75)

$$\mathbf{u}_f^{m+1} = \frac{\Delta t}{\rho_P}\left(H(\mathbf{u}^{m+1}) - (\nabla p)_P^{m+1}\right)_f. \tag{2.75}$$

The face interpolate of the velocity must satisfy the continuity equation. Taking the divergence of both sides of (2.75) and setting the result to zero gives the pressure equation

$$\nabla \cdot \left(\frac{\Delta t}{\rho_P} H(\mathbf{u}^{m+1}) \right)_f = \nabla \cdot \left(\frac{\Delta t}{\rho_P} \nabla p^{m+1} \right)_f , \tag{2.76}$$

which in discretized form is

$$\begin{aligned} &\left(\nabla \cdot \mathbf{u}_P^m - \frac{\Delta t}{\rho_P V_P} \sum_f \nabla \cdot \left(\phi_f^m \mathbf{u}_f^{m+1} \right) + \frac{\Delta t}{\rho_P V_P} \sum_f \nabla \cdot \left(\mu_f \mathbf{A}_f \cdot \nabla \mathbf{u}_f^{m+1} \right) \right)_f \\ &+ \left(\frac{\Delta t}{\rho_P} \nabla \cdot S_u^{m+1} + \frac{\Delta t^2}{\rho_P} \nabla \cdot S_p^{m+1} \mathbf{u}_P^{m+1} \right)_f = \left(\frac{\Delta t}{\rho_P V_P} \sum_f \nabla \cdot \left(\mathbf{A}_f p_f^{m+1} \right) \right)_f . \end{aligned} \tag{2.77}$$

Equation (2.77) gives a system of linear equations that is solved iteratively using a geometric-algebraic multi-grid method. The initial and boundary conditions are set-up and the momentum equation assembled with the available fluxes. The pressure is converged at each time step using a pressure correction algorithm PISO (Issa et al., 1986). The flux is updated to ensure that it satisfies the continuity equation and the updated fluxes are used to solve the VOF advection equation and the smoothed VOF equation. This is done until the final time is reached.

2.9 Implementation into OpenFOAM®

OpenFOAM® (Open Field Operation and Manipulation) is an open source C++ library of CFD tools and solvers. It is based on the FVM of discretization and is the tool of choice in this study because new models can be incorporated into existing solvers to simply modify a solver or to create new solvers altogether.

Like any standard CFD software, obtaining a numerical solution can be divided into three stages: Pre-processing, simulation and post-processing (Versteeg and Malalasekera, 2007). OpenFOAM® has utilities to pre-process, which involves the creation of a computational domain and setting up the initial and boundary conditions. Simple geometries are used in this study, therefore the inbuilt mesh generation utility *blockMesh* is used in this study.

The simulation corresponds to obtaining a numerical solution by executing a solver. The models derived in this study are implemented into the multiphase flow solver *interFoam* that solves the evolution of an interface using a standard VOF method. It comes standard with parallel processing using an MPI library. The solution domain is decomposed

and the numerical solution is obtained by executing the solver over multiple parallel processors.

Post-processing involves visualization and processing the output data from the solution. The visualization tool used is ParaView and data manipulation is done in GNU Octave.

2.10 Closure

The governing Navier-Stokes equations for an incompressible viscous multiphase Newtonian fluid undergoing laminar and isothermal three-dimensional flow have been formulated. The VOF method for modelling interfaces has been introduced with the surface tension force formulated by the CSF method. A smoothing of the volume fraction field has been introduced to reduce the magnitude of nonphysical velocities that arise when second-order gradients of the discontinuous function α are calculated in the computation of the curvature. The governing system of equations have been discretized using a FVM with an implicit time discretization to give rise to a system of equations that can be solved iteratively. The solution procedure has been discussed in the framework of the open source software OpenFOAM®.

Chapter 3

Particle Interaction Modelling

The mathematical model derived in the previous chapter represents the standard VOF method which could be described as a single marker method, where different volumes of the same fluid are assigned the same volume fraction value. In this standard implementation, numerical merging of the interfaces occurs whenever two interfaces are within a mesh cell spacing of each other. This is because the VOF method does not resolve the position of the interface to a resolution less than the mesh spacing. Thus, when two interfaces approach within the cell spacing, they are automatically merged into one. This behaviour is unrealistic.

Consider the interaction of two particles. After they collide, a thin liquid film of the surrounding fluid is squeezed between them. As the film becomes thinner, viscous forces slow down the drainage processes. Eventually, if the film reaches a critical thickness (typically $O(100\text{nm})$), instabilities cause it to break up and the particles to merge. However, during the time taken for the film to drain the particles may begin to bounce apart, resulting in no coalescence occurring. The VOF method requires extremely fine mesh resolution to model the drainage of the thin film.

Coyajee and Boersma (2009) introduced a technique to overcome numerical coalescence known as the multiple marker method in the framework of the CLSVOF method. It differs from the standard VOF and LS methods in that separate marker functions are used to represent different bodies of the same fluid. The method was successful in preventing numerical coalescence. However, the method makes no attempt to model the physical coalescence process, and, indeed, will never allow particles to merge. Another drawback is the high numerical cost of the CLSVOF method.

In this chapter, two new contributions are proposed to address these shortcomings. Firstly, the multiple marker method is applied and tested in the VOF framework in

order to provide faster solution times, and secondly the Reynolds equation is introduced as a surface model to model the thin film which forms between two Smooth Multiple Marker VOF (SMMVOF) interfaces.

The remainder of this chapter is structured as follows: in Section 3.1 the origin of the numerical coalescence is discussed in detail. The next Section, Section 3.2 introduces the SMMVOF method as a means to prevent numerical coalescence. Section 3.3 provides a detailed derivation of the Reynolds equation to model the thin film thickness. Section 3.4 the numerical discretization and solution procedure is provided. The results of the chapter are summarized in Section 3.5.

3.1 Numerical coalescence

Consider two immiscible fluids in a discretized domain $\Omega \in \mathbb{R}^3$ separated into three time dependent sub-domains, two of which are spheres with radius R as shown in Figure 3.1.

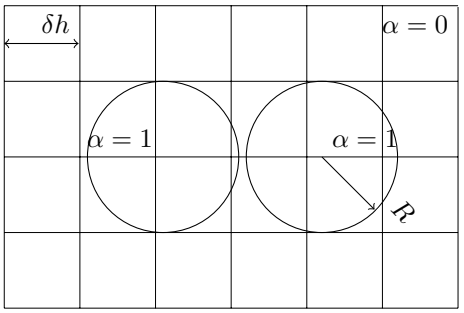

FIGURE 3.1: Two immiscible spheres with radius R in a discretized domain

The mesh spacing is denoted by δh. The volume fraction field for a sphere is equal to one within that sphere's radius and zero outside. The fluid flow equations would be solved on the entire flow domain together with the VOF advection equation at every time step.

Consider the solution of the flow equations and VOF advection equation on two different computational grids – a coarse and a fine grid. The grid resolution is quantified by the ratio of the droplet diameter D to the mesh spacing δh in one of the coordinate axes. For the two grids considered here this is given by $\frac{D}{\delta h} = 20$ and 200.

Figures 3.2 – 3.3 show how the standard VOF method performs at reconstructing the interface as the grid resolution is improved. The length between the interfaces in both grids is kept constant at $0.0025D$. From Figure 3.2 the existence of the separation distance between the interfaces is questionable. There is not enough resolution to model

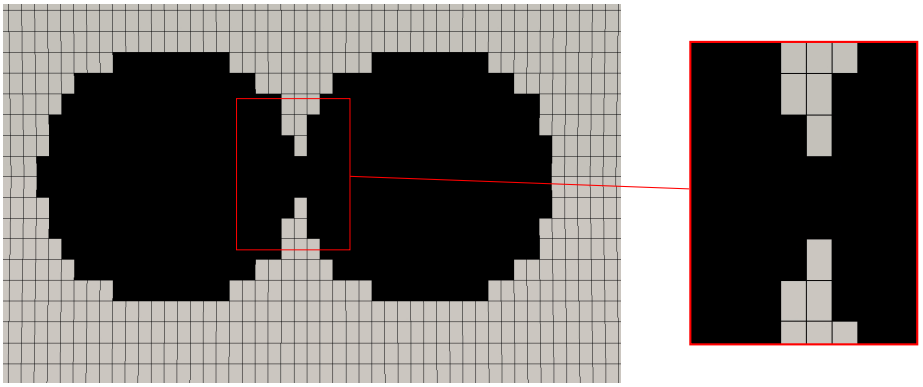

FIGURE 3.2: Two immiscible spheres with radius R in a discretized domain with $\frac{D}{\delta h} = 20$

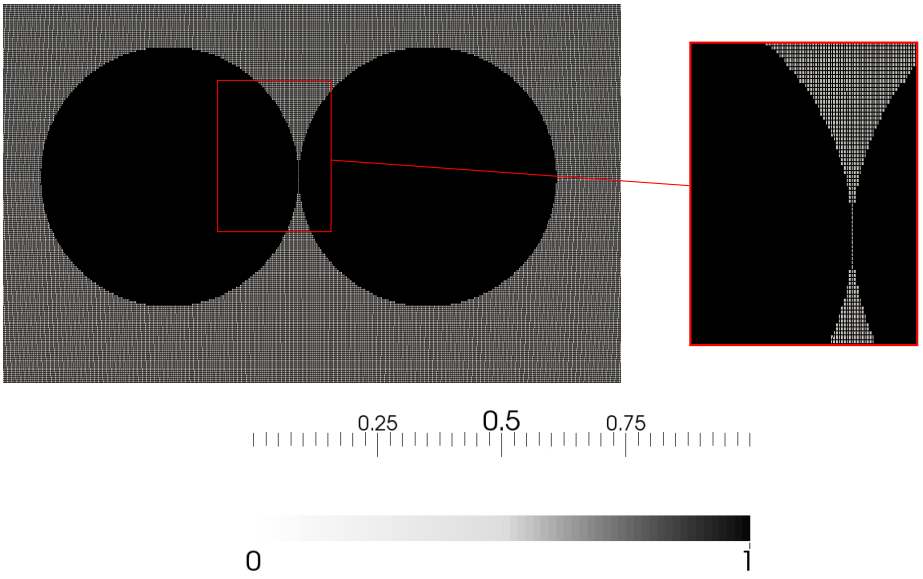

FIGURE 3.3: Two immiscible spheres with radius R in a discretized domain with $\frac{D}{\delta h} = 200$

its existence and consequently its dynamics. However as the mesh is excessively refined to a very small mesh spacing the separation distance is resolved as in Figure 3.3.

Therefore, as the droplets move close to each other the small distance that separates their interfaces is not correctly resolved by the VOF indicator field, and a liquid bridge forms between them. The surface tension force of each droplet is directed towards the centre of the droplet, acts to keep it spherical and determines its equilibrium shape. However, the presence of the liquid bridge alters this. Figure B.1 is a schematic representation of the surface tension force direction in the standard VOF implementation.

As the droplets move closer to each other, the surface tension force (shown by $\mathbf{f}^{\sigma}$ in Figure B.1) acts at the interfaces as shown. The neck of the liquid bridge introduces

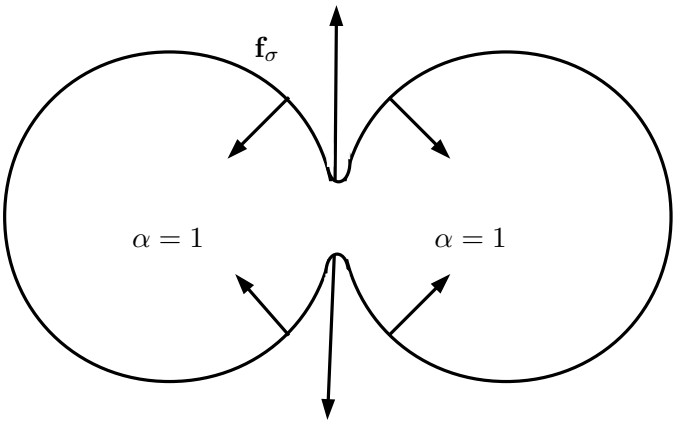

FIGURE 3.4: Schematic representation of the surface tension force directions in the standard VOF method

a region of very high curvature and the surface tension force directed outwards acts to reduce these regions of high curvature. As the simulation progresses the liquid bridge stretches open to result in the merging of the volume fraction fields in what has been observed as nonphysical coalescence. Ideally the droplets could be almost infinitely close to each other without them artificially merging because the surface tension force keeps each sphere separate.

Excessive mesh refinement is required to resolve the thin liquid film that exists between the droplets. This is important for modelling droplet hydrodynamics such as coalescence and rebound. The accuracy of simulating particle collision with the VOF method improves with refinement of the interface, but the order of refinement required is impractical. As previously mentioned, the thin film separating the particles typically persists down to a thickness of the order of $O(100\text{nm})$, requiring $\frac{D}{\delta h} \sim O(10^3 - 10^6)$ for typical particle diameters encountered. The use of adaptive mesh refinement can reduce the computational effort but it can become costly whenever one considers large numbers of particles, as is often encountered in industrial applications.

To model the close interaction of particles without nonphysical or premature coalescence at a reduced computational cost the Multiple Marker VOF method is adopted. The section that follows discusses this method in the framework of the smoothed VOF method.

3.2 Multiple Marker VOF method

Consider again the two immiscible fluids in a discretized domain introduced in the previous section. The immiscible fluids (both spheres) were assigned the same volume fraction field value of one and the continuous phase assigned a volume fraction field value of zero. The domain in figure 3.1 is redefined as in Figure 3.5.

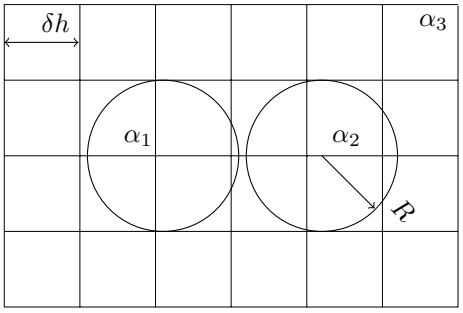

FIGURE 3.5: Two immiscible spheres with radius R in a discretized domain represented by the SMMVOF method

Let us now consider N volumes of the immiscible fluid, $\Omega_\theta(t)$, $\theta \in \{1, 2, ..., N\}$, dispersed in a continuous fluid. Define for each volume a volume fraction field value $\alpha_1, \alpha_2, ..., \alpha_N$. Each volume is represented mathematically by

$$\Omega_\theta(t) = \{\mathbf{x} \mid \alpha_\theta(\mathbf{x}, t) = 1\}, \qquad \theta \in \{1, 2, ..., N\}. \tag{3.1}$$

Similar to the single marker VOF method, the transport equation for each volume fraction field is given by

$$\frac{\partial \alpha_\theta}{\partial t} + \nabla \cdot (\alpha_\theta \mathbf{u}) = 0, \qquad \theta \in \{1, 2, ..., N\} \tag{3.2}$$

with the corresponding smoothed field obtained by solving

$$\alpha_\theta^s - \alpha_\theta = \nabla^2(\eta \alpha_\theta^s), \qquad \theta \in \{1, 2, ..., N\} \tag{3.3}$$

where α_θ^s is the smoothed volume fraction field for each individual domain Ω_θ. This method introduces N equations for the volume fraction field compared to one advection equation for the single marker VOF method. The volume fraction field α_{N+1} for the continuous phase is given by

$$\alpha_{N+1} = 1 - \sum_{\theta=1}^{N} \alpha_\theta \tag{3.4}$$

and the corresponding smoothed volume fraction field α^s_{N+1} is given by

$$\alpha^s_{N+1} = 1 - \sum_{\theta=1}^{N} \alpha^s_\theta. \tag{3.5}$$

Information about the density and dynamic viscosity is stored in a list that defines each individual phase. An effective volume fraction field defined by

$$\alpha^* = \sum_{\theta=1}^{N} \alpha_\theta, \tag{3.6}$$

is used to obtain the density $\rho = \rho(\alpha^*)$ and dynamic viscosity $\mu = \mu(\alpha^*)$ of the bulk fluid which are evaluated similarly to equations (2.46) and (2.47).

The smoothed curvature

$$\kappa^s_\theta = -\nabla \cdot \left(\frac{\nabla \alpha^s_\theta}{|\nabla \alpha^s_\theta|} \right), \tag{3.7}$$

is computed for each individual particle interface.

The surface tension force is computed from the smoothed curvature,

$$\mathbf{f}^s_\sigma = \sum_{\theta=1}^{N} \sigma \kappa^s_\theta \nabla \alpha_\theta, \tag{3.8}$$

and is a summed contribution of the force between each particle and the surrounding continuous fluid, where σ is the coefficient of surface tension between the particle fluid and continuous fluid.

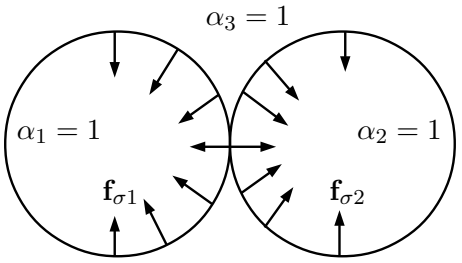

FIGURE 3.6: Schematic representation of the surface tension force in the SMMVOF method

The surface tension calculation, equation (3.8), assumes that each fluid volume (particle) is surrounded by the continuous fluid even if there is a neighbouring volume of the same fluid (an adjacent particle). At the interface of two interacting particles the direction of the surface tension force is as shown in Figure 3.6. The surface tension force acts to

keep the individual volumes separate which prevents the nonphysical coalescence that results with the standard VOF method.

The governing equations for the SMMVOF method are the Navier-Stokes equations for an incompressible viscous multiphase Newtonian fluid undergoing laminar and isothermal 3D flow together with the transport equation of each of the individual dispersed volumes.

$$\nabla \cdot (\rho \mathbf{u}) = 0 \tag{3.9}$$

$$\frac{\partial(\rho \mathbf{u})}{\partial t} + \nabla \cdot (\rho \mathbf{u}\mathbf{u}) = -\nabla p + \nabla \cdot (\mu \nabla \mathbf{u}) + \rho \mathbf{g} + \sum_{\theta=1}^{N} \sigma \kappa_\theta^s \nabla \alpha_\theta \tag{3.10}$$

$$\frac{\partial \alpha_\theta}{\partial t} + \nabla \cdot (\alpha_\theta \mathbf{u}) = 0 \tag{3.11}$$

$$\alpha_\theta^s - \alpha_\theta = \nabla^2(\eta \alpha_\theta^s) \tag{3.12}$$

$$\kappa_\theta^s = \left(-\nabla \cdot \frac{\nabla \alpha_\theta^s}{|\nabla \alpha_\theta^s|} \right) \tag{3.13}$$

The numerical solution is obtained by the same procedure discussed in Chapter 2. The FVM method is used to discretize the governing equations which are solved iteratively with the PISO algorithm. The equation for the volume fraction fields both smooth and unsmoothed is solved one at a time for each individual phase.

In the SMMVOF method the surface tension force is calculated for each individual fluid volume. Each fluid volume is always assumed to be surrounded by a different fluid and this ensures that the fluid volumes are always separate. The SMMVOF method will always prevent the nonphysical coalescence that is inherent in the VOF method. The method can thus simulate successfully the collision of particles that always result in rebound, but will not model particle collision that results in coalescence. In the next section the Reynolds equation from lubrication theory is introduced and derived as a surface thin film model to calculate the thickness of the thin film between interacting particles to provide a criterion for coalescence.

3.3 Surface thin film model of coalescence

Modelling coalescence is an important aspect of a numerical method for dispersed multiphase flow because it is responsible for droplet or bubble size evolution (Liao and Lucas, 2010) in various industrial applications.

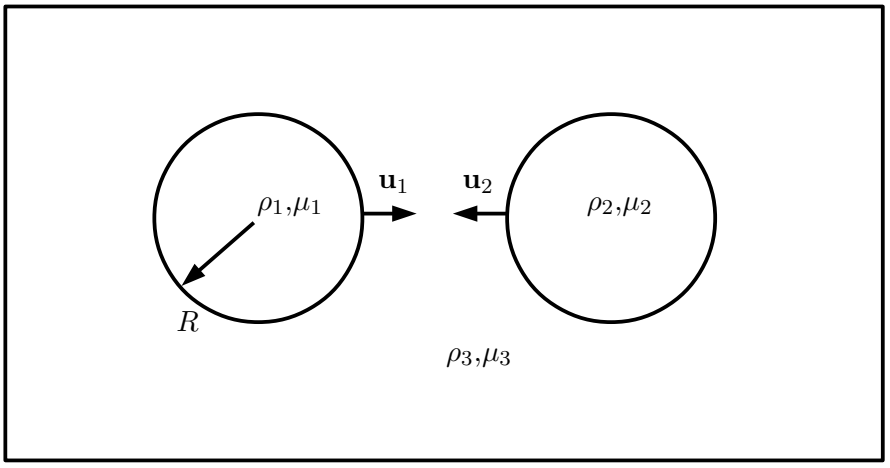

FIGURE 3.7: Two particles with radius R approaching each other with velocities $\mathbf{u}_1$ and $\mathbf{u}_2$

Liao and Lucas (2010) and Chan et al. (2011) give a comprehensive review of coalescence models that have been used. They summarize the models under three categories with the most popular being the film drainage theory. The film drainage theory of coalescence can be described in three stages. Stage 1 is when the particles approach each other (Figure 3.7), and as they do so a thin liquid film of the surrounding fluid is trapped between them; Stage 2 (Figure 3.8) is when this liquid film drains out to a film thickness h over a drainage time t_d; and lastly in Stage 3 if the film thickness attains the critical thickness, the film becomes unstable and ruptures leading to coalescence, but if the critical film thickness is not attained the particles will bounce apart.

Stage 2 is the most complex of the three stages. As the particles move closer together the thin liquid film starts to drain out. In their review of film drainage models for tangentially immobile interfaces, Coons et al. (2003) explained the evolution of the interface deformation. As the particles move closer to each other, the hydrodynamic drag increases the normal force resulting in the interface changing its shape from convex to concave in what is referred to in the literature as the "dimple" (Figure 3.9) (Jiang and James, 2006, Quan, 2012) which can evolve to form a bell shape while others evolve to a planar shape depicted in Figure 3.8.

The film thickness h at which coalescence occurs is much smaller than the radius of the dispersed fluid particles. A surface model that accounts for the thin film explicitly is suggested to model the coalescence of impacting particles to be implemented in the

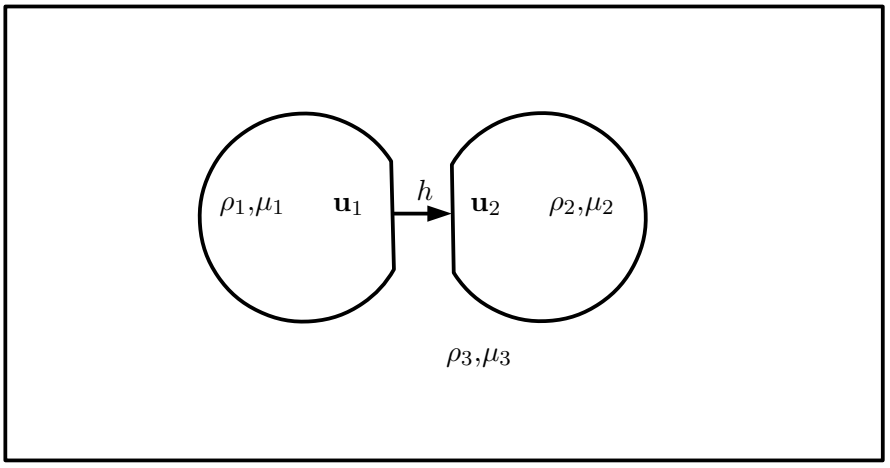

FIGURE 3.8: Two particles with radius R approaching each other with velocities $\mathbf{u}_1$ and $\mathbf{u}_2$ forming a locally planar thin film

framework of the SMMVOF method. This implementation will prevent premature numerical coalescence but will allow physical coalescence to occur whenever the thin film has drained to a critical thickness h_{Crit}.

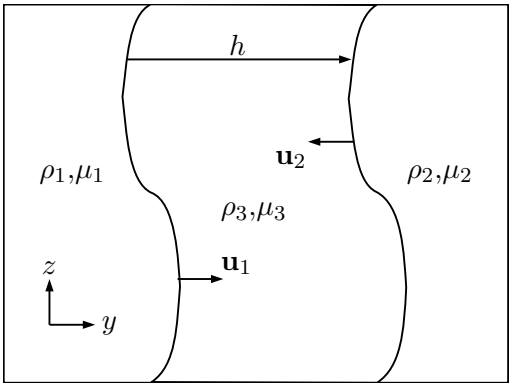

FIGURE 3.9: Dimpled thin liquid film between two interfaces

3.3.1 Problem description

Consider two mobile interfaces that are approaching each other with velocities $\mathbf{u}_1$ and $\mathbf{u}_2$ as shown in Figure 3.10. The interfaces enclose two dispersed particles described by the SMMVOF method. Let R denote the radius of the dispersed particle and h_0 the initial separation between the interfaces. The fluid bounded by each interface is assigned a volume fraction field value in the framework of the SMMVOF method. As

time progresses the two interfaces continue to approach each other and the pressure inside the thin film region forces the fluid out. When the thickness between the interfaces reaches h_{Crit} the interfaces merge to form a single fluid volume. h_{Crit} is a user input parameter into the model.

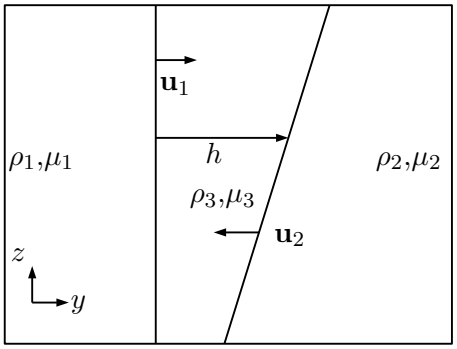

FIGURE 3.10: Close-up view of a locally planar thin film

3.3.2 Model assumptions

The following assumptions are taken into consideration when deriving the hydrodynamic Reynolds equation;

1. Since the thin film thickness is much smaller than the radius of either particle ($h \ll R$), the interfaces between each particle and the film can be assumed to be locally planar. Thus, the film locally resembles a box in three dimensions or a tube in two dimensions. In the derivation that follows, we define the $x-z$ axis to be co-planar with interface 1. The y axis is therefore in the direction of the film thickness as shown in Figure 3.10.

2. The film thickness is thus a function of the other two coordinate directions and time:
$$h = h(x, z, t). \tag{3.14}$$

3. In this tube the effects of gravity and surface tension are considered negligible.

4. Across the thickness of the thin film the pressure gradient is assumed to be constant:
$$\frac{\partial p}{\partial y} = 0. \tag{3.15}$$

5. The continuity equation holds:
$$\frac{\partial \rho}{\partial t} + \frac{\partial}{\partial x}(\rho u_x) + \frac{\partial}{\partial y}(\rho u_y) + \frac{\partial}{\partial z}(\rho u_z) = 0. \tag{3.16}$$

3.3.3 Boundary conditions

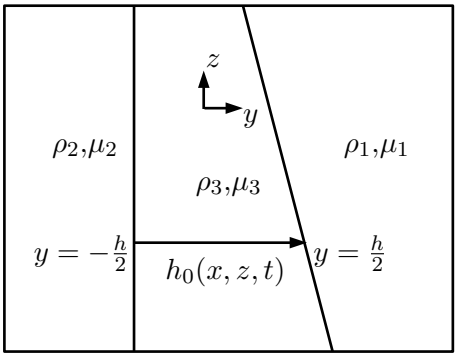

FIGURE 3.11: Boundary conditions for two-dimensional planar thin film model

With origin of the coordinate axis placed at the centre of the thin film, the tangential velocity at the boundaries is given by

$$u_x = U_1, \qquad u_z = W_1 \qquad \text{at} \qquad y = \frac{h}{2} \tag{3.17}$$

and

$$u_x = U_2, \qquad u_z = W_2 \qquad \text{at} \qquad y = -\frac{h}{2}. \tag{3.18}$$

The normal velocity u_y at the top and bottom interfaces can be related to the rate of change over time of the film thickness h:

$$\frac{dh}{dt} = u_y(x, h/2, z) - u_y(x, -h/2, z), \tag{3.19}$$

where $(x(t), h(t)/2, z(t))$ and $(x(t), -h(t)/2, z(t))$ are fixed points on the upper and lower interfaces. By assumption 2, h is a function of three variables and its temporal rate of change can be written as

$$\frac{dh}{dt} = \frac{\partial h}{\partial t} + \frac{\partial h}{\partial x}\frac{dx}{dt} + \frac{\partial h}{\partial z}\frac{dz}{dt} \tag{3.20}$$

where $\frac{dx}{dt}$ and $\frac{dz}{dt}$ are the lateral velocities u_x and u_z of the boundaries. Substituting (3.20) into (3.19) and evaluating at each boundary, the relative normal velocity is given by

$$u_y\Big|_{h/2} - u_y\Big|_{-h/2} = \frac{\partial h}{\partial t} + \frac{1}{2}\frac{\partial h}{\partial x}(U_1 + U_2) + \frac{1}{2}\frac{\partial h}{\partial z}(W_1 + W_2). \tag{3.21}$$

3.3.4 Model derivation

Applying assumption 3 to the Navier-Stokes momentum equation (3.10) written out in the three coordinate directions, these become

x-direction:

$$\rho\left(\frac{\partial u_x}{\partial t}+u_x\frac{\partial u_x}{\partial x}+u_y\frac{\partial u_x}{\partial y}+u_z\frac{\partial u_x}{\partial z}\right)=-\frac{\partial p}{\partial x}+\mu\left(\frac{\partial^2 u_x}{\partial x^2}+\frac{\partial^2 u_x}{\partial y^2}+\frac{\partial^2 u_x}{\partial z^2}\right), \tag{3.22}$$

y-direction:

$$\rho\left(\frac{\partial u_y}{\partial t}+u_x\frac{\partial u_y}{\partial x}+u_y\frac{\partial u_y}{\partial y}+u_z\frac{\partial u_y}{\partial z}\right)=-\frac{\partial p}{\partial y}+\mu\left(\frac{\partial^2 u_y}{\partial x^2}+\frac{\partial^2 u_y}{\partial y^2}+\frac{\partial^2 u_y}{\partial z^2}\right), \tag{3.23}$$

and z-direction:

$$\rho\left(\frac{\partial u_z}{\partial t}+u_x\frac{\partial u_z}{\partial x}+u_y\frac{\partial u_z}{\partial y}+u_z\frac{\partial u_z}{\partial z}\right)=-\frac{\partial p}{\partial z}+\mu\left(\frac{\partial^2 u_z}{\partial x^2}+\frac{\partial^2 u_z}{\partial y^2}+\frac{\partial^2 u_z}{\partial z^2}\right). \tag{3.24}$$

Dimensional analysis is used to determine which terms in the above equations dominate. Let the characteristic length in the x and z directions be given by the radius R of the dispersed particle, and the characteristic length in the y direction by the thin film thickness h. Let U, V and W be the characteristic velocity scale in the x , y and z directions and let the corresponding characteristic pressures be given by $\frac{\mu UR}{h^2}$, $\frac{\mu VR}{h^2}$ and $\frac{\mu WR}{h^2}$ respectively. The characteristic time scales are given by $\frac{R}{U}$, $\frac{h}{V}$ and $\frac{R}{W}$. The equations (3.22)-(3.24) in non-dimensional form are then given by

x-direction:

$$\frac{\rho Uh^2}{\mu R}\frac{\partial u_x^*}{\partial t^*}+\frac{\rho Uh^2}{\mu R}u_x^*\frac{\partial u_x^*}{\partial x^*}+\frac{\rho Vh}{\mu}u_y^*\frac{\partial u_x^*}{\partial y^*}+\frac{\rho Wh^2}{\mu R}u_z^*\frac{\partial u_x^*}{\partial z^*}= -\frac{\partial p^*}{\partial x^*}+\left(\underline{\frac{h^2}{R^2}\frac{\partial^2 u_x^*}{\partial x^{*2}}}+\frac{\partial^2 u_x^*}{\partial y^{*2}}+\underline{\frac{h^2}{R^2}\frac{\partial^2 u_x^*}{\partial z^{*2}}}\right),$$

y-direction:

$$\frac{\rho Vh}{\mu}\frac{\partial u_y^*}{\partial t^*}+\frac{\rho Uh^2}{\mu R}u_x^*\frac{\partial u_y^*}{\partial x^*}+\frac{\rho Vh}{\mu}u_y^*\frac{\partial u_y^*}{\partial y^*}+\frac{\rho Wh^2}{\mu R}u_z^*\frac{\partial u_y^*}{\partial z^*}= -\frac{R}{h}\frac{\partial p^*}{\partial y^*}+\left(\underline{\frac{h^2}{R^2}\frac{\partial^2 u_y^*}{\partial x^{*2}}}+\frac{\partial^2 u_y^*}{\partial y^{*2}}+\underline{\frac{h^2}{R^2}\frac{\partial^2 u_y^*}{\partial z^{*2}}}\right),$$

z-direction:

$$\frac{\rho W h^2}{\mu R}\frac{\partial u_z^*}{\partial t^*} + \frac{\rho U h^2}{\mu R}u_x^*\frac{\partial u_z^*}{\partial x^*}\frac{\rho V h}{\mu}u_y^*\frac{\partial u_z^*}{\partial y^*} + \frac{\rho W h^2}{\mu R}u_z^*\frac{\partial u_z^*}{\partial z^*} = -\frac{\partial p^*}{\partial x^*} + \left(\underline{\frac{h^2}{R^2}\frac{\partial^2 u_z^*}{\partial x^{*2}}} + \frac{\partial^2 u_z^*}{\partial y^{*2}} + \underline{\frac{h^2}{R^2}\frac{\partial^2 u_z^*}{\partial z^{*2}}}\right),$$

where x^*, y^*, z^*, p^*, u_x^*, u_y^*, u_z^* and t^* are the non-dimensional variables.

The terms on the LHS are negligible: they scale as $Re(h^2/R^2) \ll 1$ and $Re(h/R) \ll 1$ using assumption 1, where $Re = \frac{\rho U R}{\mu}$, $Re = \frac{\rho V R}{\mu}$ and $\frac{\rho W R}{\mu}$ in each direction respectively. Likewise, the underlined terms on the RHS are negligible as they scale as $h^2/R^2 \ll 1$. The reduced equations are thus

x-direction:

$$0 = -\frac{\partial p^*}{\partial x^*} + \frac{\partial^2 u_x^*}{\partial y^{*2}} \tag{3.25}$$

y-direction:

$$0 = -\frac{R}{h}\frac{\partial p^*}{\partial y^*} + \frac{\partial^2 u_y^*}{\partial y^{*2}} \tag{3.26}$$

z-direction:

$$0 = -\frac{\partial p^*}{\partial x^*} + \frac{\partial^2 u_z^*}{\partial y^{*2}}, \tag{3.27}$$

The equation in the y-direction can be rewritten as

$$0 = -\frac{\partial p^*}{\partial y^*} + \frac{h}{R}\frac{\partial^2 u_y^*}{\partial y^{*2}}. \tag{3.28}$$

Using assumption 1 the second term is negligible and the equation reduces to

$$0 = -\frac{\partial p^*}{\partial y^*}. \tag{3.29}$$

The pressure is thus independent of y and is a function of x,z and time t. Omitting asterisks for convenience, the equations are

x-direction:

$$0 = -\frac{\partial p}{\partial x} + \mu\frac{\partial^2 u_x}{\partial y^2}, \tag{3.30}$$

y-direction:

$$p = p(x, z, t), \tag{3.31}$$

z-direction:

$$0 = -\frac{\partial p}{\partial z} + \mu\frac{\partial^2 u_z}{\partial y^2}, \tag{3.32}$$

Integration of Equations (3.30) and (3.32) in the x and z directions across the thin film thickness yields

$$u_x = \frac{1}{2\mu}\frac{\partial p}{\partial x}y^2 + A_1 y + A_2 \tag{3.33}$$

and

$$u_z = \frac{1}{2\mu}\frac{\partial p}{\partial z}y^2 + A_3 y + A_4, \tag{3.34}$$

where A_1–A_4 are constants of integration. These are obtained by evaluating (3.33) and (3.34) at the boundaries $-\frac{h}{2}$ and $\frac{h}{2}$ to obtain

$$u_x = \frac{1}{2\mu}\frac{\partial p}{\partial x}\left(y^2 - \frac{h^2}{4}\right) + \left(\frac{U_1 - U_2}{h}\right)y + \frac{U_1 + U_2}{2}, \tag{3.35}$$

and

$$u_z = \frac{1}{2\mu}\frac{\partial p}{\partial z}\left(y^2 - \frac{h^2}{4}\right) + \left(\frac{W_1 - W_2}{h}\right)y + \frac{W_1 + W_2}{2}. \tag{3.36}$$

The above two equations give the velocity in the x and z directions. The mass flow rates in the x and z directions are defined as

$$M_x = \int_{-\frac{h}{2}}^{\frac{h}{2}} (\rho u_x)dy \tag{3.37}$$

$$= -\frac{\rho}{12\mu}\frac{\partial p}{\partial x}h^3 + \rho\left(\frac{U_1 + U_2}{2}\right)h, \tag{3.38}$$

and

$$M_z = \int_{-\frac{h}{2}}^{\frac{h}{2}} (\rho u_z)dy \tag{3.39}$$

$$= -\frac{\rho}{12\mu}\frac{\partial p}{\partial z}h^3 + \rho\left(\frac{W_1 + W_2}{2}\right)h. \tag{3.40}$$

Integration of the continuity equation (3.16) from $-\frac{h}{2}$ to $\frac{h}{2}$ using the Leibnitz rule gives

$$\frac{\partial}{\partial t}\int_{-\frac{h}{2}}^{\frac{h}{2}} \rho dy - \frac{1}{2}\rho\Big|_{\frac{h}{2}}\frac{\partial h}{\partial t} - \frac{1}{2}\rho\Big|_{-\frac{h}{2}}\frac{\partial h}{\partial t} + \frac{\partial}{\partial x}\int_{-\frac{h}{2}}^{\frac{h}{2}} (\rho u_x)dy - \frac{1}{2}\rho u_x\Big|_{\frac{h}{2}}\frac{\partial h}{\partial x}$$
$$-\frac{1}{2}\rho u_x\Big|_{-\frac{h}{2}}\frac{\partial h}{\partial x} + \rho u_y\Big|_{\frac{h}{2}} - \rho u_y\Big|_{-\frac{h}{2}} + \frac{\partial}{\partial z}\int_{-\frac{h}{2}}^{\frac{h}{2}} (\rho u_z)dy - \frac{1}{2}\rho u_z\Big|_{\frac{h}{2}}\frac{\partial h}{\partial z} - \frac{1}{2}\rho u_z\Big|_{-\frac{h}{2}}\frac{\partial h}{\partial z} = 0.$$

Evaluation of the boundary terms using (3.17), (3.18) and (3.21) together with the definitions of M_x and M_z results in

$$\frac{\partial}{\partial t}(\rho h) + \frac{\partial}{\partial x}M_x + \frac{\partial}{\partial z}M_z = 0. \tag{3.41}$$

Substituting for M_x and M_z in (3.41),

$$\frac{\partial(\rho h)}{\partial t}+\frac{\partial}{\partial x}\left(-\frac{\rho}{12\mu}\frac{\partial p}{\partial x}h^3+\rho\left(\frac{U_1+U_2}{2}\right)h\right)+\frac{\partial}{\partial z}\left(-\frac{\rho}{12\mu}\frac{\partial p}{\partial z}h^3+\rho\left(\frac{W_1+W_2}{2}\right)h\right)=0, \tag{3.42}$$

and rearranging the above we have the Reynolds equation from lubrication theory:

$$\frac{\partial(\rho h)}{\partial t}+\left(\frac{U_1+U_2}{2}\right)\frac{\partial}{\partial x}(\rho h)+\left(\frac{W_1+W_2}{2}\right)\frac{\partial}{\partial z}(\rho h)=\frac{\partial}{\partial x}\left(-\frac{\rho h^3}{12\mu}\frac{\partial p}{\partial x}\right)+\frac{\partial}{\partial z}\left(-\frac{\rho h^3}{12\mu}\frac{\partial p}{\partial z}\right). \tag{3.43}$$

In the above the axes have been chosen to be locally aligned with the film. Now (3.43) is expressed in a form that is independent of the coordinate system chosen. For this purpose, $\mathbf{n}$ is defined as a unit vector normal to interface 1. Equation (3.43) can then be written in terms of $\mathbf{n}$ as

$$\frac{\partial(\rho h)}{\partial t}+\mathbf{Q}\cdot[\nabla\rho h-(\nabla\rho h\cdot\mathbf{n})\mathbf{n}]=\nabla\cdot\left[\frac{-\rho h^3}{12\mu}[\nabla p-(\nabla p\cdot\mathbf{n})\mathbf{n}]\right] \tag{3.44}$$

where $\mathbf{Q}$ is the interface velocity vector

$$\mathbf{Q}=\frac{\mathbf{u}_1+\mathbf{u}_2}{2}, \tag{3.45}$$

with $\mathbf{u}_1$ and $\mathbf{u}_2$ the velocity of interface 1 and 2 respectively.

3.4 Numerical Implementation

The equation (3.44) that governs the dynamics of the thin film has been derived in the previous section. The model equations that govern the multiphase flow of interacting particles are the Navier-Stokes equations in the SMMVOF framework coupled with the Reynolds equation. Following a multiscale approach, the SMMVOF method is used to obtain the flow variables while the Reynolds equation is used to solve for the thickness of the thin film.

The solution to equation (3.44) gives the thickness h of the thin film between two interfaces. Typically, the Reynolds equation (3.44) is solved for pressure given a known time variation of the film thickness. In this study, however, the pressure is obtained from the solution of the Navier-Stokes equation and used together with an initial film thickness to obtain a new estimate of the film thickness.

In the derivation it is assumed that $h \ll R$, thus the Reynolds equation (3.44) is only valid when the film is thin; it is not valid when particles are far apart. Thus to obtain a solution, we need to detect when the thin film is thin enough and initialize the equation

with an initial thickness. The solution procedure involves firstly devising a way to measure the separation distance h_{Est} between particles that is valid for separation of a few mesh cells or greater. The length of this distance defines a region in space and time that will be used to determine when and where the Reynolds equation is valid. Secondly once the separation distance has been obtained the Reynolds equation is solved iteratively only in the region between the interfaces. In this section these two aspects of obtaining the numerical solution to equation (3.44) are discussed.

3.4.1 Initial separation distance

The solution domain and the governing equations for the SMMVOF method are discretized using the FVM as discussed in Chapter 2, Section 2.7. The computational domain is discretized to form cells with width δh which can be larger or smaller than the thin film thickness h.

A graphical approach based on measuring the distance from each volume fraction is used to obtain the separation h_{Est} between the particles. Consider two interfaces that enclose fluids described by the volume fraction fields α_1 and α_2 which are close to each other in a computational domain. Consider lines which start from the interfaces pointing in the direction of the outward unit normal to the interface $\mathbf{n}_1^s$ and $\mathbf{n}_2^s$,

$$\mathbf{n}_1^s = \frac{\nabla(\alpha_1^s)}{\mid \nabla(\alpha_1^s) \mid}, \qquad \mathbf{n}_2^s = \frac{\nabla(\alpha_2^s)}{\mid \nabla(\alpha_2^s) \mid}. \tag{3.46}$$

Define the length from a point on the interface $\mathbf{x}_i$ to a point $\mathbf{x}$ on a ray by the path integral along the ray in the direction $\mathbf{n}^s$,

$$h_{Est_1} = \int_{\mathbf{x}_i}^{\mathbf{x}} (1-\alpha_1)\mathbf{n}_1^s \cdot d\mathbf{l}, \tag{3.47}$$

and

$$h_{Est_2} = \int_{\mathbf{x}_i}^{\mathbf{x}} (1-\alpha_2)\mathbf{n}_2^s \cdot d\mathbf{l}. \tag{3.48}$$

Equations (3.47) and (3.48) can be expressed in differential form to aid in discretization:

$$\nabla h_{Est_1} \cdot \mathbf{n}_1^s = (1-\alpha_1) \tag{3.49}$$

and

$$\nabla h_{Est_2} \cdot \mathbf{n}_2^s = (1-\alpha_2). \tag{3.50}$$

The path integrals (3.47) and (3.48) start from the interface so a switch is used to set the initial value at the interface to zero. The above two equations need to be replaced by

$h_{Est_1} = 0$ and $h_{Est_2} = 0$ inside the particle, so we multiply both sides of equations (3.49) and (3.50) by a positive boolean switch ($[1 - \text{pos}(\alpha_1 - 0.95)]$ and $[1 - \text{pos}(\alpha_2 - 0.95)]$), and add $[\text{pos}(\alpha_1 - 0.95)h_{Est_1}]$ and $[\text{pos}(\alpha_2 - 0.95)h_{Est_2}]$ to the respective equations so that when $\alpha_1 > 0.95$ and $\alpha_2 > 0.95$ we end up with $h_{Est_1} = 0$ and $h_{Est_2} = 0$. The function $\text{pos}(s)$ is a positive Boolean given by

$$\text{pos}(s) = \begin{cases} 1 & s \geq 0, \\ 0 & s < 0. \end{cases} \tag{3.51}$$

Equations (3.49) and (3.50) are then replaced by

$$[1 - \text{pos}(\alpha_1 - 0.95)]\,(\nabla h_{Est_1} \cdot \mathbf{n}_1^s) = [1 - \text{pos}(\alpha_1 - 0.95)]\,(1 - \alpha_1) + \text{pos}(\alpha_1 - 0.95)h_{Est_1} \tag{3.52}$$

and

$$[1 - \text{pos}(\alpha_2 - 0.95)]\,(\nabla h_{Est_2} \cdot \mathbf{n}_2^s) = [1 - \text{pos}(\alpha_2 - 0.95)]\,(1 - \alpha_2) + \text{pos}(\alpha_2 - 0.95)h_{Est_2}. \tag{3.53}$$

The scalar product can be expanded using a divergence identity[1] to give

$$\begin{aligned} [1 - \text{pos}(\alpha_1 - 0.95)]\,(\nabla \cdot (h_{Est_1}\mathbf{n}_1^s) - h_{Est_1}(\nabla \cdot \mathbf{n}_1^s)) = \\ [1 - \text{pos}(\alpha_1 - 0.95)]\,(1 - \alpha_1) + \text{pos}(\alpha_1 - 0.95)h_{Est_1} \end{aligned} \tag{3.54}$$

and

$$\begin{aligned} [1 - \text{pos}(\alpha_2 - 0.95)]\,(\nabla \cdot (h_{Est_2}\mathbf{n}_2^s) - h_{Est_2}(\nabla \cdot \mathbf{n}_2^s)) = \\ [1 - \text{pos}(\alpha_2 - 0.95)]\,(1 - \alpha_2) + \text{pos}(\alpha_2 - 0.95)h_{Est_2}, \end{aligned} \tag{3.55}$$

which will simplify the discretization process even further. Evaluating the integral form of the equations and applying Gauss' divergence theorem (2.56), the discretized equations for the separation distance are

$$\begin{aligned} [1 - \text{pos}(\alpha_1 - 0.95)] \left(\sum_f (\mathbf{A} \cdot h_{Est_1}\mathbf{n}^s)_f - h_{Est_1} \sum_f (\mathbf{A} \cdot \mathbf{n}^s)_f \right) = \\ \Big([1 - \text{pos}(\alpha_1 - 0.95)]\,(1 - \alpha_1) + \text{pos}(\alpha_1 - 0.95)h_{Est_1} \Big)_P V_P \end{aligned} \tag{3.56}$$

[1] Let c be a scalar and $\boldsymbol{\Psi}$ a vector, then $\nabla \cdot (c\boldsymbol{\Psi}) = c\nabla \cdot \boldsymbol{\Psi} + \nabla c \cdot \boldsymbol{\Psi}$

and

$$[1-\text{pos}(\alpha_2-0.95)]\left(\sum_f(\mathbf{A}\cdot h_{Est_2}\mathbf{n}^s)_f - h_{Est_2}\sum_f(\mathbf{A}\cdot\mathbf{n}^s)_f\right) = \left([1-\text{pos}(\alpha_2-0.95)]\,(1-\alpha_2)+\text{pos}(\alpha_2-0.95)h_{Est_2}\right)_P V_P. \tag{3.57}$$

The discretized equations give a system of equations which are solved iteratively with the source terms on the LHS treated implicitly.

In the region between the two interfaces, the sum of h_{Est_1} and h_{Est_2} gives the separation distance between the interfaces. Thus the estimate h_{Est} is obtained from

$$h_{Est} = h_{Est_1} + h_{Est_2} \tag{3.58}$$

since this gives the sum of the distance to interface 1 along the ray in direction $\mathbf{n}_1^s$ and the distance to interface 2 along the ray in direction $\mathbf{n}_2^s$ from any given point. This approach cannot however be used to obtain distances that are smaller than a mesh cell spacing since the SMMVOF method does not provide enough resolution at that scale. The value of h_{Est} is used as an initial condition for the Reynolds equation.

3.4.2 Thin film region

With the initial separation distance between the interfaces calculated, a region where the Reynolds equation is valid is calculated. An estimate of the mesh spacing δh in the direction normal to the thin film,

$$\delta h = \frac{\sum_f |\mathbf{n}^{s*}\cdot\mathbf{A}_f|\frac{V}{|\mathbf{A}_f|}}{\sum_f |\mathbf{n}^{s*}\cdot\mathbf{A}_f|} \tag{3.59}$$

is calculated for each cell. Here, V is the volume of the cell, $\mathbf{n}^{s*}$ the unit normal vector obtained from the smoothed volume fraction field values of both interfaces

$$\mathbf{n}^{s*} = \frac{\nabla(-\alpha_1^s+\alpha_2^s)}{|\,\nabla(-\alpha_1^s+\alpha_2^s)\,|}, \tag{3.60}$$

and $\mathbf{n}^{s*}\cdot\mathbf{A}_f$ is the projected face area in the direction normal to the interface.

A multiple of the mesh spacing estimate is used to restrict and define the mesh location where equation (3.44) is actually calculated. This restricts the calculation of the equation to areas that are very close to the thin film region. The boolean switch which identifies

the region is defined by

$$\beta = \text{pos}\left(\xi\delta h - h_{Est}\right)\text{pos}(\alpha_1^s - 0.001)\text{pos}(\alpha_2^s - 0.001) \tag{3.61}$$

where ξ is a parameter that determines the width of the region where the thin film equation is solved as a multiple of the mesh spacing.

The region β is set to one (turned on) whenever $h_{Est} < \xi\delta h$, i.e. whenever the initial separation distance is less than the width of ξ cells. In addition, in regions where either α_1^s or α_2^s are very close to zero, β is set to zero (turned off); this allows for the calculation to hold even when the smoothed volume fraction field values α^s are constant and hence $\mathbf{n}^s$ and δh are not correctly calculated. These regions are sufficiently far from the particle interfaces (where $\alpha^s = 0.5$), that the thin film equation is not valid in these regions and is not solved. In order for h_{Est} to be used as initial value of h to solve the Reynolds equation, h is set equal to h_{Est} outside the thin film region, i.e. where $\beta = 0$. The thin film equation (3.44) now becomes

$$\begin{aligned}\beta\left(\frac{\partial(\rho h)}{\partial t} + \mathbf{Q}\cdot[\nabla\rho h - (\nabla\rho h\cdot\mathbf{n})\mathbf{n}]\right) + (1-\beta)h = \\ \beta\left(\frac{-\rho h^3}{12\mu}\nabla\cdot\nabla p_t\right) + \beta\left(-\frac{3\rho\nabla p_t h^2}{12\mu}\nabla h\right) + (1-\beta)h_{Est}\end{aligned} \tag{3.62}$$

where the divergence term on the RHS has been simplified and $\nabla p_t = \nabla p - (\nabla p\cdot\mathbf{n})\mathbf{n}$ denotes the tangential pressure gradient.

There is a numerical discontinuity between the values of h inside the thin film region β and those outside that have been pegged to h_{Est}. Evaluation of the gradient of h in the second last term of (3.62) would be incorrect for computational cells that surround the thin film region. To avoid the discontinuity of the gradient of h at the boundary of the thin film region the gradient of h is evaluated in a reduced thin film region $\beta_{reduced}$ defined by

$$\beta_{reduced} = \text{pos}\left(\frac{\sum_f \beta|\mathbf{A}_f|}{\sum_f|\mathbf{A}_f|} - 0.99\right), \tag{3.63}$$

which is a single mesh cell spacing less than β. This will only consider the gradient of h in cells that are within the thin film region itself only. The second last term that includes the gradient of h in (3.62) is evaluated in $\beta_{reduced}$ to obtain

$$\begin{aligned}\beta\left(\frac{\partial(\rho h)}{\partial t} + \mathbf{Q}\cdot[\nabla\rho h - (\nabla\rho h\cdot\mathbf{n})\mathbf{n}]\right) + (1-\beta)h = \\ \beta\left(\frac{-\rho h^3}{12\mu}\nabla\cdot\nabla p_t\right) + \beta_{reduced}\left(-\frac{3\rho\nabla p_t h^2}{12\mu}\nabla h\right) + (1-\beta)h_{Est}.\end{aligned} \tag{3.64}$$

The smoothing of the volume fraction fields smears the interface which means the pressure gradient obtained from the Navier-Stokes equations in the interface region is a combination of the gas and liquid pressure. The two pressures differ by the surface tension pressure jump. In addition, pressure fluctuations in the liquid are much greater than in the gas, and smoothing was found to help counter the effects of this numerical noise.

The surface tension pressure jump is removed by removing the surface tension force from the tangential pressure

$$\overline{\nabla p_t} = \nabla p_t - \mathbf{f}_\sigma^s. \tag{3.65}$$

The pressure $\overline{\nabla p_t}$ is smoothed using a similar procedure as in Section 2.5 to give $\overline{\nabla p_t}^s$. Thus (3.64) becomes

$$\begin{aligned} \beta\left(\frac{\partial(\rho h)}{\partial t} + \mathbf{Q}\cdot[\nabla\rho h - (\nabla\rho h\cdot\mathbf{n})\mathbf{n}]\right) + (1-\beta)h = \\ \beta\left(\frac{-\rho h^3}{12\mu}\nabla\cdot\overline{\nabla p_t}^s\right) + \beta_{reduced}\left(-\frac{3\rho\overline{\nabla p_t}^s h^2}{12\mu}\nabla h\right) + (1-\beta)h_{Est}. \end{aligned} \tag{3.66}$$

The discretization of (3.66) follows the FVM method. The integral form of the governing equations is

$$\begin{aligned} \int_{t_n}^{t_n+\Delta t}\beta\left[\int_{V_P}\frac{\partial\rho h}{\partial t}\,dV + \int_{V_P}\mathbf{Q}\cdot[\nabla\rho h - (\nabla\rho h\cdot\mathbf{n})\mathbf{n}]\,dV\right]dt + \\ \int_{t_n}^{t_n+\Delta t}\left[\int_{V_P}(1-\beta)h\,dV\right]dt = \int_{t_n}^{t_n+\Delta t}\beta\left[\int_{V_P}\frac{-\rho h^3}{12\mu}\nabla\cdot\overline{\nabla p_t}^s\,dV\right]dt + \\ \int_{t_n}^{t_n+\Delta t}\beta_{reduced}\left[\int_{V_P}\frac{-3\rho\overline{\nabla p_t}^s h^2}{12\mu}\nabla h\,dV\right]dt\int_{t_n}^{t_n+\Delta t}\left[\int_{V_P}(1-\beta)h_{Est}\,dV\right]dt \end{aligned} \tag{3.67}$$

which can be simplified using Gauss' divergence theorem using a similar procedure as in Chapter 2 Section 2.7:

$$\begin{aligned} \int_{t_n}^{t_n+\Delta t}\beta\left(\frac{\partial\rho h}{\partial t}\right)_P V_P\,dt + \int_{t_n}^{t_n+\Delta t}\beta\left(\mathbf{Q}\cdot[\nabla\rho h - (\nabla\rho h\cdot\mathbf{n})\mathbf{n}]\right)_P V_P\,dt + \\ \int_{t_n}^{t_n+\Delta t}(1-\beta)h_P V_P\,dt = \int_{t_n}^{t_n+\Delta t}\beta\left(\frac{-\rho h^3}{12\mu}\sum_f\mathbf{A}_f\cdot\overline{\nabla p_t}^s\right)_f dt + \\ \int_{t_n}^{t_n+\Delta t}\beta_{reduced}\left(\frac{-3\rho\overline{\nabla p_t}^s h^2}{12\mu}\mathbf{A}_f h_f\right)\,dt + \int_{t_n}^{t_n+\Delta t}(1-\beta)(h_{Est})_P V_P\,dt \end{aligned} \tag{3.68}$$

Evaluating the time integrals with an implicit Euler method with the assumption that the density remains constant results in

$$\beta\frac{\rho_P h_P^{m+1}-\rho_P h_P^m}{\Delta t}V_P+\beta\mathbf{Q}\cdot\left[\nabla\rho_P h_P^{m+1}-\left(\nabla\rho_P h_P^{m+1}\cdot\mathbf{n}\right)\mathbf{n}\right]V_P+(1-\beta)h_P^{m+1}V_P=$$
$$\beta\frac{-\rho_f(h_f^{m+1})^3}{12\mu_f}\sum_f\mathbf{A}_f\cdot(\overline{\nabla p_t}^s)_f^{m+1}+\beta_{reduced}\frac{-3\rho_f(\overline{\nabla p_t}^s)_f^{m+1}(h_f^{m+1})^2}{12\mu_f}\mathbf{A}_f h_f^{m+1}+$$
$$(1-\beta)(h_{Est})_P^{m+1}V_P \tag{3.69}$$

which is solved using an algebraic multi-grid solver. The velocity at the particle interfaces is extrapolated to obtain the interface velocity vector $\mathbf{Q}$ throughout the thin film region using a graphical approach in a manner similar to the thin film thickness estimate in the previous section.

A flow chart of the solution procedure of the SMMVOF method coupled with the surface thin film method is provided in Appendix B. The procedure summarised there is as follows;

- Set-up the initial and boundary conditions
- Calculate the available fluxes and the multiple volume fraction fields
- Obtain the smoothed volume fraction field values and calculate the smoothed curvature
- Assemble the momentum equation
- Assemble and solve the pressure equation using a pressure correction algorithm
- Calculate h_{Est}
- Where $h_{Est} \leq \xi\delta h$
  - Solve the surface thin film model in the region β to advance h in time
  - If $min(h) < h_{Crit}$
    - Merge the volume fraction fields
- Where $h_{Est} > \xi\delta h$
  - set $h = h_{Est}$
  - Do not solve the surface film model
- Move on to the next time step and repeat until the final time is obtained

3.5 Closure

In this Chapter the SMMVOF has been introduced as a means to prevent nonphysical coalescence that is inherent in the VOF method. This method is based on a smoothed VOF method that can accurately calculate the interface curvature with minimal nonphysical velocities. A surface thin film model that determines coalescence has been derived and implemented into the OpenFOAM® framework. In the next chapter the model is tested.

Chapter 4

Validation

The objective of this study is to develop and use a DNS approach based on a smoothed VOF method to model particle-particle interactions in a dispersed multiphase flow at a fundamental level, and employing a surface thin film model, to drastically reduce the computational effort required. Three aspects were identified that limited the numerical modelling of particle-particle interaction using the VOF method from the moment of impact to resulting coalescence or rebound: the nonphysical velocities that arise as a result of inaccurate calculation of the curvature; the inherent nonphysical coalescence that arises when interfaces enclosing separate particles are within a single mesh cell spacing; and consequently the inability of the VOF method to model coalescence correctly without using excessively refined computational grids.

Each of these aspects was discussed in detail in the previous two chapters. Each aspect forms a building block and when combined they provide a model that can be used to study particle-particle coalescence and rebound. In this chapter the proposed model implemented into the open source software OpenFOAM® is tested.

The remainder of this chapter is structured as follows: In Section 4.1 the diffusive type smoother coupled to the VOF method is tested by simulating a static two-dimensional sphere with negligible gravity. The effect of the smoothing parameter χ on reducing the magnitude of the nonphysical velocities is studied to determine its optimal value. The chosen optimal value is then used for the remainder of the tests.

In Section 4.2 the SMMVOF method is tested by simulating the gravity driven droplet impact onto a liquid-liquid interface and the results compared to the experiment of Mohamed-Kassim and Longmire (2003). In Section 4.3, the Reynolds equation coupled to the previous two sub-models is validated by simulating the collision of hydrocarbon

droplets in 1 atm Nitrogen from the experiment of Pan et al. (2008). Lastly Section 4.4 summarizes the findings from the three test cases.

4.1 Test case: static sphere

In this section the implementation of the diffusive type smoother coupled to the VOF method to reduce the magnitude of the nonphysical velocities for surface tension driven flows is validated using a static two-dimensional sphere. A static droplet or bubble test case is frequently used in the literature to study the magnitude of the nonphysical velocities and to validate implementations to reduce their magnitude. Ideally the pressure gradient is balanced by the surface tension force. The pressure difference across the droplet is given by the Young-Laplace equation

$$\Delta p = \sigma\kappa, \tag{4.1}$$

where R is the radius and κ is the radius of curvature: $\kappa = \frac{2}{R}$ in three dimensions and $\kappa = \frac{1}{R}$ in two dimensions.

4.1.1 Computational set-up

In two dimensions consider a sphere with a radius $R = 1$mm in a 6mm by 6mm square domain of air with negligible gravity and material properties given by Table 4.1. The

Quantity		Liquid	Gas
ρ	(kgm^{-3})	1000	1
μ	$(\text{kgm}^{-1}\text{s}^{-1})$	1×10^{-03}	1.5×10^{-05}

TABLE 4.1: Material Properties of a two-dimensional sphere in a square domain

mesh is composed of 120×120 two-dimensional cells. Initially zero velocity is imposed in the interior of the domain with no slip conditions at the boundaries and the gravity set to 0ms^{-2}. The centre of the sphere is placed at the centre of the domain and the simulation is run up a time of 0.05 seconds.

The effect of the user defined smoothing variable χ is studied by varying it from 0 to 4, with 0 corresponding to no smoothing or solving the standard VOF method using the standard OpenFOAM® solver *interFoam*, and 4 corresponding to smoothing the volume fraction field over 4 cells. Three different surface tension coefficients are studied: $\sigma = 0.001$, 0.01 and 0.1 kgs^{-2}.

The analytical result for the pressure difference across the droplet is given by the Young-Laplace equation (4.1). A comparison of the numerical and analytic pressure is made. The results of all the physical quantities that follow in the next section are time averaged.

4.1.2 Numerical results

The results of the pressure estimate obtained by using the different values of χ for each of the surface tension coefficients are shown in Figures 4.1-4.3.

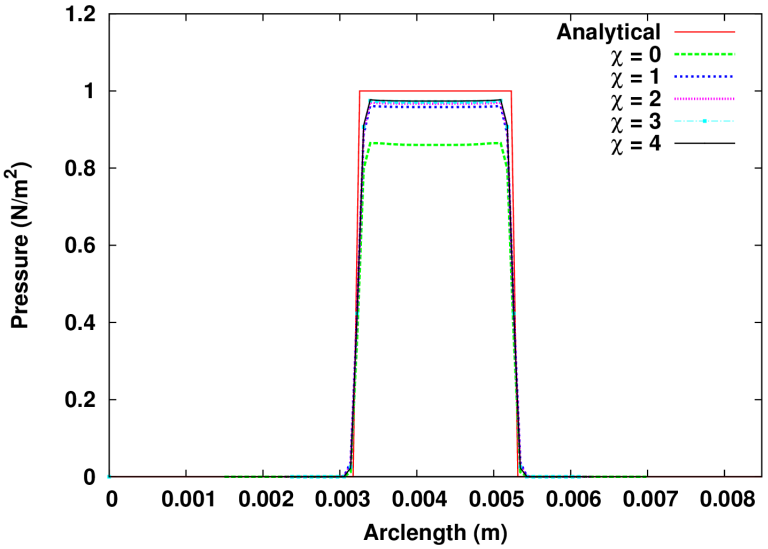

FIGURE 4.1: Pressure at different values of χ for $\sigma = 0.001$ kgs^{-2}

For the values of $\chi = 0$ for the three different test cases the pressure is underestimated (Figures 4.1-4.3). This is as expected and the result supports the observations made in the literature that the standard VOF method inaccurately computes the curvature in the CSF framework. An inaccurate curvature calculation will result in an incorrect prediction of the pressure from the Young-Laplace equation. As the surface tension coefficient is increased the pressure estimate is still underestimated. The percentage error in the pressure for $\chi = 0$ for $\sigma = 0.001$ kgs^{-2} is 12.59%, for $\sigma = 0.01$ kgs^{-2} is 13.01% and for $\sigma = 0.1$ kgs^{-2} is 12.19%.

As χ is increased from 1 to 4 a drastic improvement is seen in the ability of the smoothed VOF method to correctly compute the curvature compared to $\chi = 0$. Table 4.2 shows the difference in error percentages between successive values of χ for the case when $\sigma = 0.001$ kgs^{-2}. The difference in error percentages is seen to decrease drastically with each successive increase of χ. A similar trend is observed for $\sigma = 0.01$ kgs^{-2} and $\sigma = 0.1$ kgs^{-2}; the successive percentage error difference is always large between $\chi = 0$ and $\chi = 1$ but only decreases gradually as χ increases. It can be postulated from this

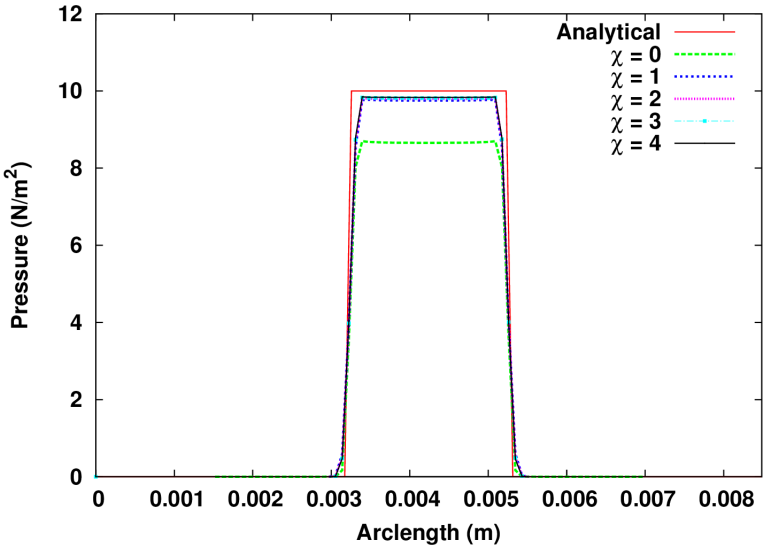

FIGURE 4.2: Pressure at different values of χ for $\sigma = 0.01$ kgs^{-2}

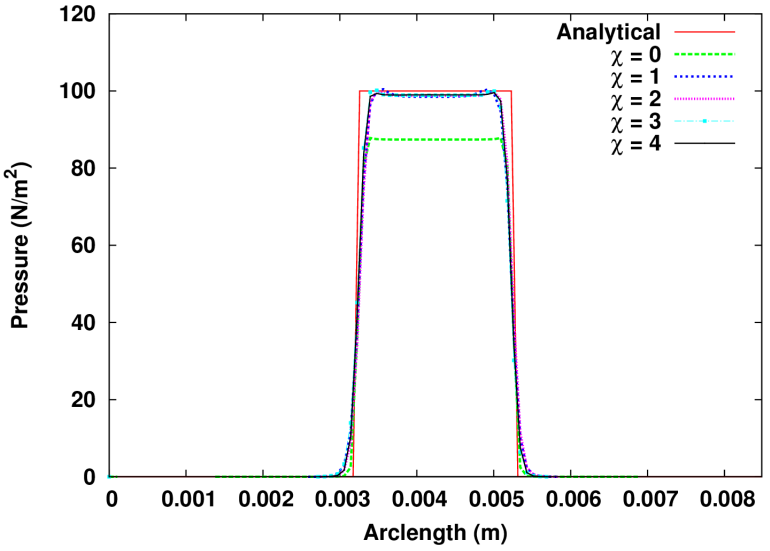

FIGURE 4.3: Pressure at different values of χ for $\sigma = 0.1$ kgs^{-2}

trend that at a certain value of χ the pressure estimate will converge to a certain result and no changes will be observed.

	Percentage error difference
$\chi = 0$ and $\chi = 1$	8.69%
$\chi = 1$ and $\chi = 2$	0.9%
$\chi = 2$ and $\chi = 3$	0.46%
$\chi = 3$ and $\chi = 4$	0.27%

TABLE 4.2: Percentage error difference between successive values of χ for $\sigma = 0.001$ kgs^{-2}

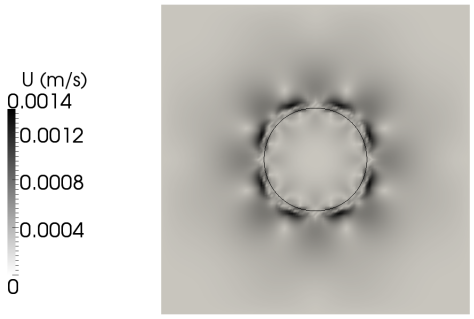

(a) Nonphysical velocities at $\sigma = 0.001$ kgs^{-2} and $\chi = 0$

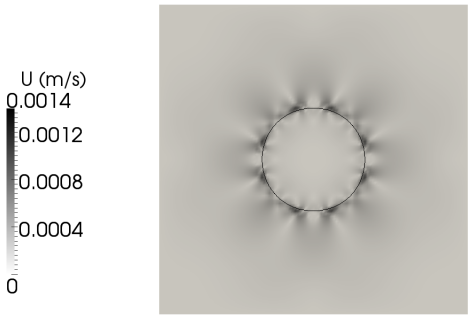

(b) Nonphysical velocities at $\sigma = 0.001$ kgs^{-2} and $\chi = 3$

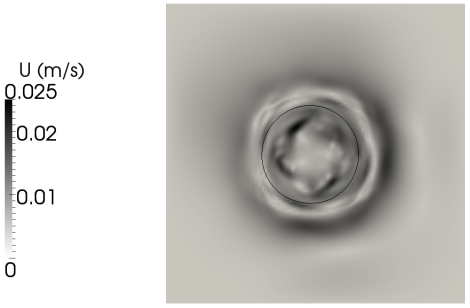

(c) Nonphysical velocities at $\sigma = 0.1$ kgs^{-2} and $\chi = 0$

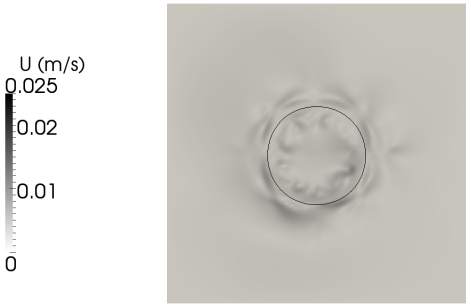

(d) Nonphysical velocities at $\sigma = 0.1$ kgs^{-2} and $\chi = 3$

FIGURE 4.4: Comparison between the nonphysical velocity estimates from the unsmoothed (left) to the smoothed (right) volume fraction

Though this is the case, choosing a value of χ that is very large will result in over-smoothing of the volume fraction field which will result in a loss of the resolution of the curvature. Under-smoothing will also result in the pressure either being underestimated or overestimated. To avoid over-smoothing or under-smoothing of the volume fraction field a value of $\chi = 3$ is chosen as the optimal smoothing variable as the difference in error percentages between $\chi = 3$ and $\chi = 4$ is very small.

A comparison of the time averaged nonphysical velocities contour plots is shown in Figure 4.4(a-d). When the surface tension coefficient is kept constant and χ is varied it is observed that the magnitude of the nonphysical velocities is decreased. A decrease in the nonphysical velocities gives a better estimate of the pressure difference. The magnitude of the nonphysical velocities is found to increase with the surface tension coefficient (c-d). At $\sigma = 0.1$ kgs^{-2} the magnitude of the nonphysical velocities is high

enough to introduce oscillations at the interface such that at the end of the simulation the sphere begins to move.

4.2 Test case: droplet impact onto a liquid-liquid interface

The SMMVOF method was introduced primarily to prevent the numerical/nonphysical coalescence that is inherent in the standard VOF method. It was shown in Chapter 3, Section 3.1 that the standard VOF method would require a high resolution computational grid to resolve the existence of the thin film that prevails between two particles that make contact during a collision. To test the method it is essential to demonstrate that the nonphysical coalescence that will otherwise result with the VOF method is prevented.

Mohamed-Kassim and Longmire (2003) studied experimentally the effect of the Reynolds number on the impact of a single droplet onto a liquid-liquid interface. The droplet fell through the liquid and on impact deformed together with the liquid-liquid interface. The surrounding fluid was trapped between the interfaces to form a thin liquid film which prevented immediate coalescence. The secondary purpose of the experiment was to provide the experimental data needed "to test numerical simulations that attempt to resolve or model effects associated with the thin film." In the next section the experimental set-up considered by Mohamed-Kassim and Longmire (2003) is discussed in detail.

4.2.1 Experimental set-up

A 0.4 m square cross section transparent tank with a height of 0.3m was filled with a mixture of water and glycerine up to a height of 0.13 m. A large tank was used to ensure that the interfacial waves that formed during impact on the liquid-liquid interface were negligible. Silicon oil was then poured into the tank for a height of 0.1 m. Two types of silicon oils that differed in fluid viscosity were used in the experiment. In this study the silicon oil with the higher viscosity is considered: this corresponds to Combination 1 of the experimental set-up and results of Mohamed-Kassim and Longmire (2003). Table 4.3 gives the experimental material properties. A water and glycerine mixture droplet with an effective diameter of 0.0103 m was injected with a syringe into the Silicon oil. Titanium dioxide particles were seeded into the tank to track the motion of the liquid and PIV was used to determine interface locations and fluid velocities.

The droplet was observed to impact the liquid-liquid interface at a normal impact velocity of $w_i = 0.132$ ms^{-1} which was also observed to be the experimental terminal velocity

	Units	Silicon oil	Water/Glycerin
ρ	kgm^{-3}	949	1128
μ	Pas	0.019	0.0063
σ	kgs^{-2}	0.0291	

TABLE 4.3: Material Properties of silicon oil (Dow Corning Fluid 200®) and water/glycerine mixture (Mohamed-Kassim and Longmire, 2003)

w_t. The moment of impact was defined as the moment when the lower droplet interface reached the 0.13 m height of the water/glycerine mixture with the corresponding impact time t_i. Length was scaled by the droplet diameter D, time was scaled by $t_i = w_i/D$. The scaled quantity $t/t_i = 0$ was set to define the time when the lower droplet interface reached the interface layer at 0.13 m. Table 4.4 gives the experimental parameters.

Parameter	Units	Combination 1
D	m	0.0103
w_i	m/s	0.132
t_i	s	0.078
Re_i		68.0
We_i		7.0
Fr_i		1.0
Eo		6.4

TABLE 4.4: Experimental Parameters (Mohamed-Kassim and Longmire, 2003)

4.2.2 Computational set-up

The published computational studies that have been compared against the above experiment include those by Zheng et al. (2005), Néstor Balcázar et al. (2014), Mohamed-Kassim et al. (2004) and Coyajee and Boersma (2009).

Zheng et al. (2005) used a two-dimensional numerical simulation to test their adaptive re-meshing for a finite-element LS simulation using a square computational domain. The droplet impact time was delayed and they shifted their results by -1.1s. Néstor Balcázar et al. (2014) used Combination 1 of the experiment to test the accuracy of their Multiple-Marker Level Set method (MLS). A cylindrical domain with dimensions $8D \times 10D$ and a total of 6×10^6 hexahedral cells were used with no-slip boundary conditions at the top and bottom of the cylindrical domain. The material properties and experimental parameters matched those of the experiment exactly.

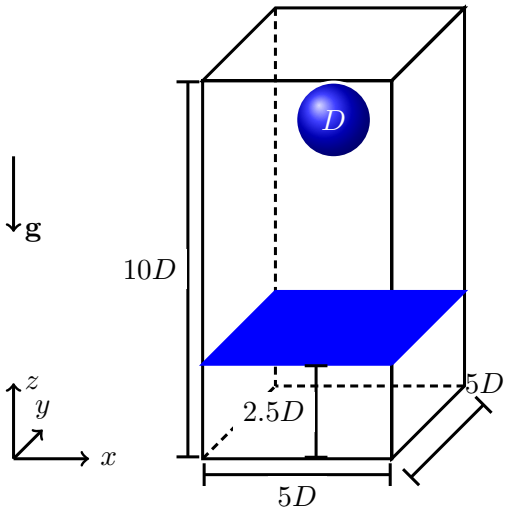

FIGURE 4.5: Schematic representation of the computational set-up

In the work of Mohamed-Kassim et al. (2004) a phase field approach was compared to a LS method with adaptive mesh refinement. The droplet was placed at an initial distance of $3D$ to the interface and similar to Zheng et al. (2005) an initial droplet velocity of $-w_i$ was set inside the droplet and zero everywhere else. They observed that the distance between the lower droplet interface and the liquid-liquid interface was smaller compared to the experiment and concluded that it was a consequence of initializing the droplet too close to the liquid-liquid interface. In the experiment the droplet reached a terminal velocity and shape before impact. Coyajee and Boersma (2009) tested their Multiple-Marker CLSVOF method with three-dimensional simulations of both Combination 1 and Combination 2 (the lower viscosity ratio) on a $5D \times 5D \times 10D$ computational domain. The computational arrangement of Coyajee and Boersma (2009) is adopted for this work with the droplet initialized at a height of $9D$ to ensure that terminal velocity is attained before impact.

The computational domain is defined to have dimensions of $5D \times 5D \times 10D$ with the liquid-liquid interface at $2.5D$ and the initial droplet height at $9D$. Figure 4.5 shows the computational arrangement with the description of the multiple volume fraction fields and the coordinate axes. The droplet itself is assigned the value $\alpha_1 = 1$, the liquid layer assigned $\alpha_2 = 1$ and the surrounding silicon oil $\alpha_3 = 1$. A $150 \times 150 \times 300$ structured cartesian mesh is used.

The initial velocity of the droplet and the surrounding fluid is initialized to 0 ms^{-1} and the gravitational acceleration set to 9.8 ms^{-2} downwards. A no-slip velocity boundary condition is employed with zero gradient pressure boundary condition on all walls.

The solution is obtained by the SMMVOF method with $\chi = 3$. The computational domain is decomposed into 16 domains and run in parallel for 31 hours.

4.2.3 Numerical results

As mentioned before all the results are reported in non-dimensional units. The experimental results provide detailed interface deformation information of the droplet trajectory before and after the impact. Figure 4.6 shows the shape profiles of the drop and interface from the experiment (left) (Mohamed-Kassim and Longmire, 2003) and the simulation (right).

At $t/t_i = 0$ (Figure 4.6 (b)) the shape profiles between the experimental and numerical results differ, which may suggest that the droplet has not attained a terminal velocity or terminal shape. As the simulation proceeds there is qualitative agreement in the shape profiles. The normalized centre line location of the upper, lower and liquid-liquid interfaces are shown in Figure 4.7 (a) and the normalized droplet thickness D_h/D (D_h is defined as the distance between the upper and lower droplet interfaces) is shown in Figure 4.7 (b). The horizontal line in Figure 4.7 (a) at $z/D = 0$ corresponds to the position of the liquid-liquid interface while the vertical line at $t/t_i = 0$ corresponds to the impact time defined earlier as the time when the lower droplet interface crosses the quiescent liquid layer.

The experimental results show that the liquid-liquid interface starts to deform before the lower droplet interface crosses $z/D = 0$. The numerical centre line location of the liquid-liquid interface also starts to deform before the actual impact but exhibits a much higher deformation from time -2 to 0. From time 0 to 2 the liquid-liquid interface attains its maximum deformation and the corresponding centre line position of the lower droplet interface also attains its minimum position. The maximum deformation of the liquid-liquid interface is underestimated. The centre line position at the upper droplet interface undergoes very small oscillations as the droplet continues to descend into the interface.

From time 2 to 6 the droplet completes a single oscillation cycle. An overestimation of the centre line position of all the interfaces is observed. After the droplet attains its lowest position it ascends more rapidly for the numerical results compared to the experiment. Excellent agreement is observed after the droplet ascends as it starts to settle to a resting position at times 4 to 8. The droplet settles at a slightly lower position as seen from times 8 to 10.

The difference between the centre line position of the lower and upper droplet interface gives the droplet height as shown in Figure 4.7 (b). The measure of drop deformation is given by the normalized droplet width and height. There is excellent agreement between experimental and numerical results. At impact $t/t_i = 0$ the droplet height does not agree with the experimental result – there is an underestimate in the centre line positions of

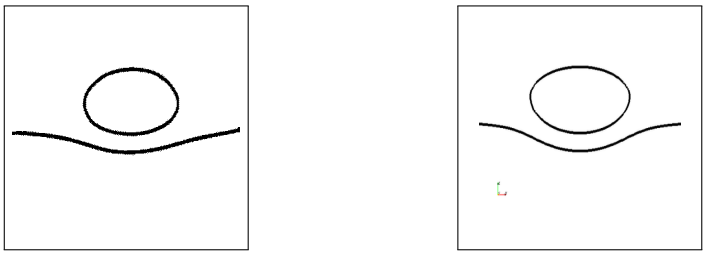

(a) $t/t_i = 0.0$

(b) $t/t_i = 0.0$

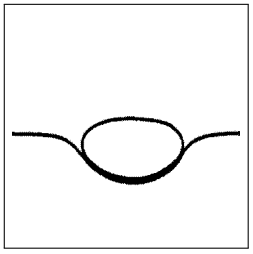

(c) $t/t_i = 0.5$

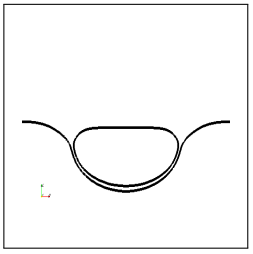

(d) $t/t_i = 0.5$

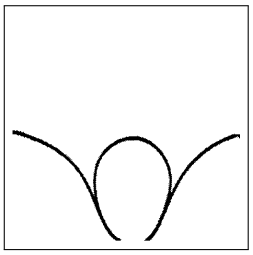

(e) $t/t_i = 1.8$

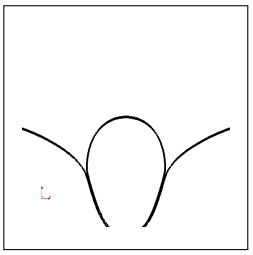

(f) $t/t_i = 1.8$

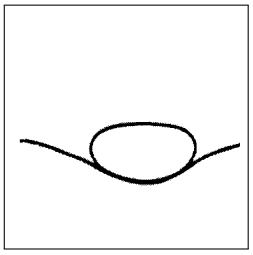

(g) $t/t_i = 3.0$

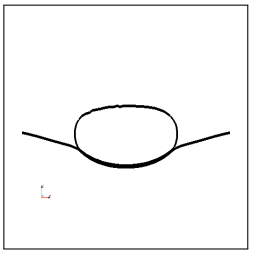

(h) $t/t_i = 3.0$

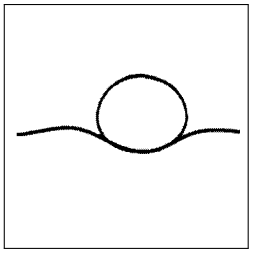

(i) $t/t_i = 5.0$

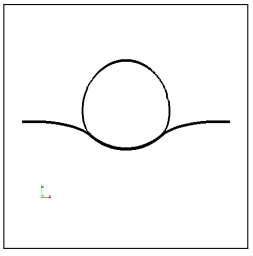

(j) $t/t_i = 5.0$

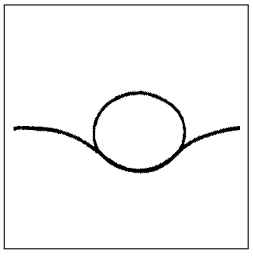

(k) $t/t_i = 7.0$

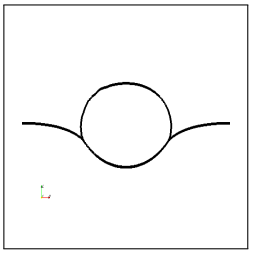

(l) $t/t_i = 7.0$

FIGURE 4.6: Shape profile of droplet and liquid-liquid interface before and during droplet impact: experimental (left) and numerical (right)

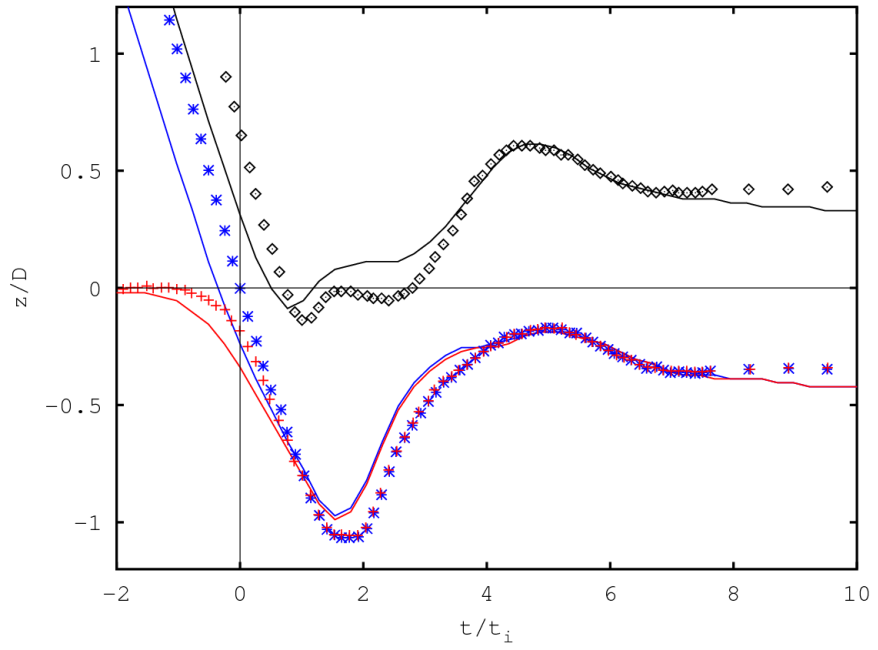

(a)

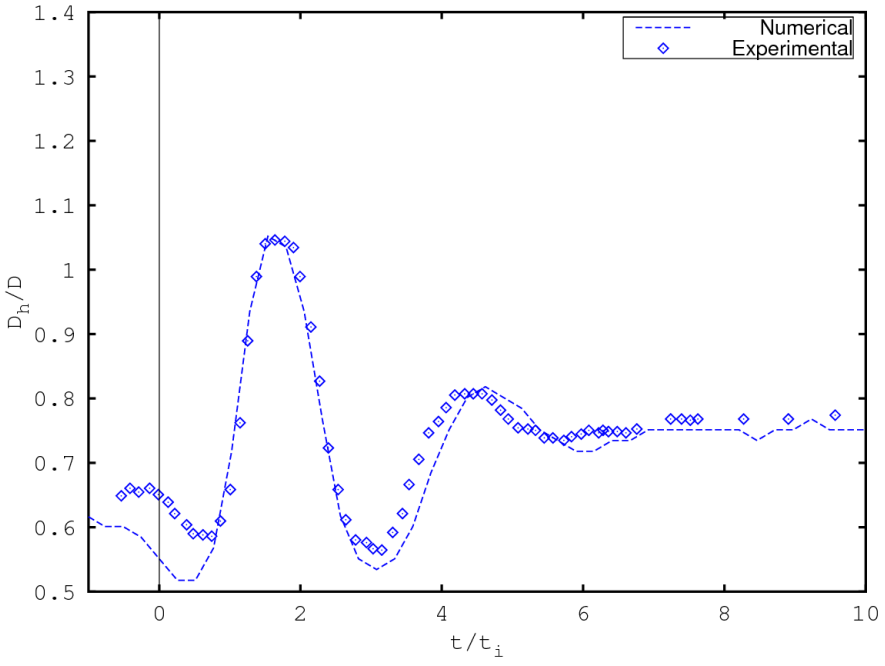

(b)

FIGURE 4.7: Numerical and experimental results (solid lines and tic marks respectively); (a) Normalized center line position of upper ($\Diamond$), lower ($*$) and liquid-liquid interface ($+$), (b) Experimental and numerical (solid lines and tic marks respectively) normalized droplet height

the lower droplet interface at impact. This is evident in the very oblate shape profile seen at impact in Figure 4.6 (b).

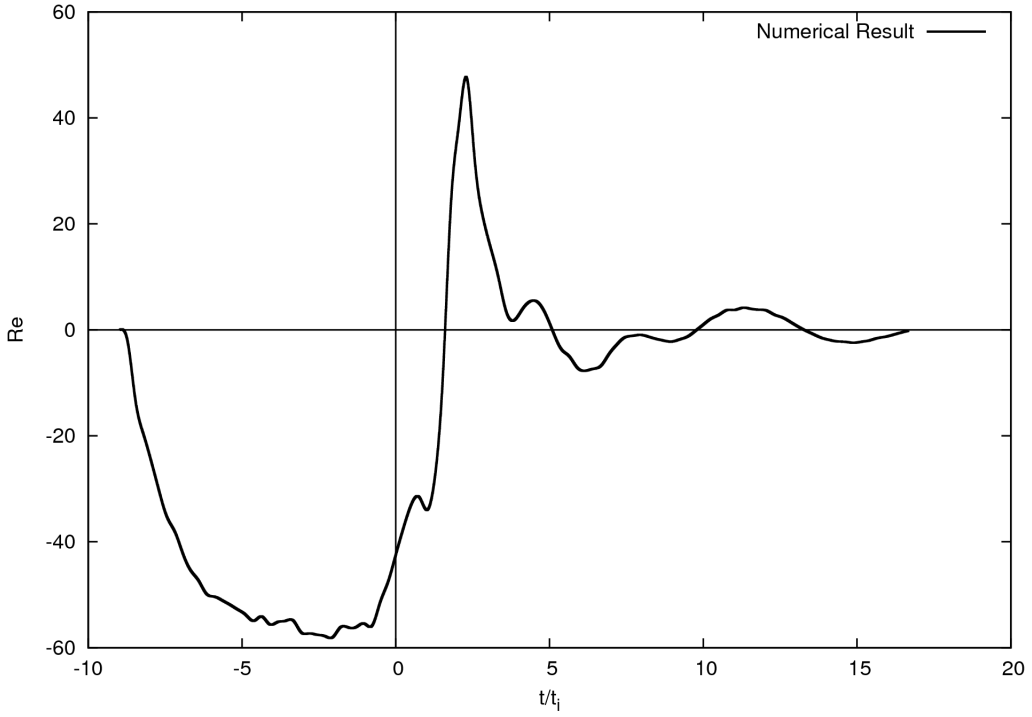

FIGURE 4.8: Droplet Reynolds number

Figure 4.8 gives the Reynolds number Re as a function of time. At the start of the simulation Re is zero, corresponding to the initial droplet velocity. It decreases as the simulation proceeds, almost achieving a terminal velocity. From the experiment the droplet attains a terminal velocity before it impacts the liquid-liquid interface. At impact time $t/t_i = 0$, Re starts to increase as the droplet comes into contact with the liquid-liquid interface. After impact the droplet is slowed down and undergoes a complete oscillation cycle before coming to a resting position.

From Figure 4.8 the droplet numerical impact velocity is found to be 0.082ms^{-1} downwards which is an underestimate of the experimental impact velocity by 38.2%.

	Current study	Coyajee and Boersma (2009)
Number of cells	6.75×10^6	8.2×10^6
Number of nodes	16	80
Number of time steps	4624	≈ 7500[1]
Execution time	$\approx$ 31 hours	$\approx$ 120 hours

TABLE 4.5: Computational arrangement comparison between current study and the numerical results of Coyajee and Boersma (2009)

[1]The numerical results of Coyajee and Boersma (2009) are quoted for the two test cases. The total number of time steps for both test cases amounted to 15000 which was performed within 240 hours. The values quoted in the table are therefore the mean values.

Table 4.5 gives a comparison between the current study to the numerical results of Coyajee and Boersma (2009). The numerical results obtained by Coyajee and Boersma (2009) agreed with the experimental results but at a higher computational cost. They simulated both combinations from Mohamed-Kassim et al. (2004) over 10 days. In the present work the numerical simulation is obtained in 31 hours. The reduced computational time may be a result of using a SMMVOF method rather than using a CLSVOF method which is computationally intensive as it requires re-initialization of the distance function to keep the LS function smooth every time step.

Overall there is a good qualitative agreement of the numerical and experimental results. The SMMVOF method is able to provide reasonable results with a practical grid size.

4.3 Test case: Tetradecane droplet impact in 1 atm Nitrogen

The validation test case used here is a binary collision of hydrocarbon droplets (Pan et al., 2008) with different Weber numbers that result in either coalescence or rebound. The experimental results provide detailed interface deformation information of the collision event. The experiment is chosen because detailed interface deformation of the collisions that result in coalescence will demonstrate the ability of the Reynolds equation to model the drainage of the thin liquid film up to the point of determined rupture. The numerical results will demonstrate that the surface thin film model coupled to the SMMVOF method is capable of simulating collisions that result in physical coalescence at a reduced computational cost.

4.3.1 Experimental set-up

Here we describe the experiment of Pan et al. (2008) involving the head-on collision of two Tetradecane ($C_{14}H_{30}$) droplets in 1 atm Nitrogen. The experimental set-up was such that identical droplets were generated by nozzles and time resolved images of their motion and collisions taken. The outcome – either coalescence or rebound – together with the film drainage times are known from the experiment. Four test cases were studied: the first two describe droplet coalescence and rebound with minimal droplet deformation while the last two describe these processes with large deformations in the droplet shapes. The material properties of Tetradecane and air are shown in Table 4.6 and a set of physical quantities, viz. individual droplet velocity U_0, droplet radius R and the Weber number $We = \frac{2\rho U_0^2 D}{\sigma}$ for each case are shown in Table 4.7. An increase in the We quantifies the degree of deformation during the collision of the droplets. The

	Liquid (Tetradecane)	Gas (Nitrogen)
Density (kgm^{-3})	762	1.225
Viscosity (μm)	107.2	170.6
Surface Tension (kgs^{-2})	0.0265	

TABLE 4.6: Material Properties for Tetradecane and Nitrogen at 20°C (Pan et al., 2008)

experimental results were normalized by the droplet oscillation period $T = 2\pi \left(\frac{\rho_l R^3}{8\sigma}\right)^{1/2}$ (Pan et al., 2008) where ρ_l is the density of Tetradecane. The drainage time was es-

Quantity	Case I	Case II	Case III	Case IV
U_0 (ms^{-1})	0.302	0.24	0.496	0.596
R (μm)	107.2	170.6	167.6	169.7
We	2.25	2.26	9.33	13.63
T (ms)	0.415	0.831	0.811	0.826

TABLE 4.7: Physical Quantities (Pan et al., 2008)

timated by determining the time from when the droplets made first contact up to the point of rupture for each of the cases that lead to coalescence. The nondimensionalized drainage time was determined to be $t_d = 0.935$ for Case I and $t_d = 0.446$ for Case IV.

4.3.2 Computational set-up

(a) Droplet set-up

(b) End on slice through mesh

FIGURE 4.9: Axisymmetric case set-up

In this study axisymmetric simulations are performed on a structured, cartesian and uniform mesh. The domain dimensions are $4D \times 2D$ where D is the corresponding droplet diameter and the initial separation between droplet centres is $1.5D$. The computational mesh is discretized into 360×80 cells in the x and z directions (Figure 4.9).

The boundary conditions for the pressure are set to zero gradient at the walls with an internal air pressure set to 101.325 kPa. A no-slip velocity boundary condition is imposed at the walls. Since the droplet radii are of the order $O(10^{-6})$, gravity is negligible in comparison with surface tension forces and the term ρg in the momentum equation is neglected.

4.3.3 Numerical results

The numerical solution is obtained by following the solution procedure outlined in Chapter 3 Section 3.4.2. The solution as described there requires the knowledge of two parameters: ξ and h_{Crit}. ξ affects the geometric determination of h_{Est} and h_{Crit} determines the width at which the thin liquid film is ruptured. The parameter ξ is a universal setting for the method, and h_{Crit} is a universal property of the materials involved, independent of the type of collision. We now turn our attention to the determination of these constants.

4.3.3.1 Selection of parameter ξ

In the calculation of the thin film region β, the parameter ξ is required to determine the mesh cell spacing at which to switch from the geometric determination of the initial separation distance between droplet interfaces h_{Est} to the solution through the surface thin film model. The restrictions on ξ are that it should be big enough that the geometric determination spans several mesh cells to make it valid, but it should not be too big (resulting in β spanning too many mesh cells) because the surface thin film model is valid when the spacing between the droplets is small compared to their radii: $h \ll R$.

It is thus essential that the results are not sensitive to the value of ξ used in the simulations. The switch-over point from the geometric determination to the solution of the surface thin film equations should take place at a separation distance where both methods are valid. The necessary condition for this is that the results should not be sensitive to the switch-over point in this range.

The values of ξ are chosen from the set of natural numbers excluding zero, one and two. A value of zero corresponds to the thin film region reducing to $\beta = 0$ which will not allow for the geometric determination of h_{Est} and thus the surface thin film model will never switch on. The cases of $\xi = 1, 2$ are not considered because it is assumed that these are too few mesh cells to provide a valid and realistic estimate for the geometrically determined h_{Est}.

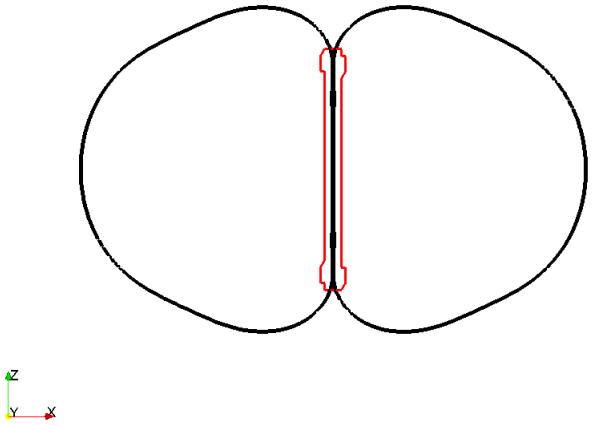

FIGURE 4.10: Thin film region β (region in red) for Case I with $\xi = 3$

The selection of ξ is determined by considering the sensitivity of the minimum predicted thin film thickness to the selection of ξ. Therefore, to determine ξ, the value of h_{Crit} is set to zero, and the numerical solution to Cases I-IV is obtained with $\xi = 3, 4, 5$. The minimum film thickness is obtained at every time step and plotted over non-dimensional time as shown in Figure 4.11(a-d). Since the minimum film thickness will not equal zero the interfaces will not be merged and a behaviour of the thin film thickness as a function of ξ is observed. The physical representation of β is shown in Figure 4.10 with $\xi = 3$ for Case I of the experiment.

The variation over non-dimensional time of the minimum film thickness with varying values of ξ is plotted in Figure 4.11(a-d) for the four test cases. In all the four test cases, as the droplets move closer to each other ($h_{Est} \leq \xi \Delta x$) the switch over from the geometric determination to the solution of h using the surface thin film model occurs. The thin film thickness decreases as can be seen from Figure 4.11(a-d). The case for $\xi = 3$ gives a higher estimate of the minimum film thickness compared to the estimate provided by $\xi = 4$ and $\xi = 5$. The film drains and subsequently the thickness starts to increase as the droplets begin to move apart in preparation for rebound.

ξ	Case I	Case II	Case III	Case IV
3	3.363×10^{-7}	5.619×10^{-7}	4.716×10^{-7}	2.078×10^{-7}
4	1.618×10^{-7}	3.872×10^{-7}	2.573×10^{-7}	1.382×10^{-7}
5	1.649×10^{-7}	3.296×10^{-7}	2.146×10^{-7}	1.094×10^{-7}

TABLE 4.8: Minimum film thickness h_{Min} (m) for Case I, Case II, Case III and Case IV

Table 4.8 gives the numerical values of the minimum film thickness for different values of ξ. An increase in the value of ξ improves the estimate to the thin film thickness. A

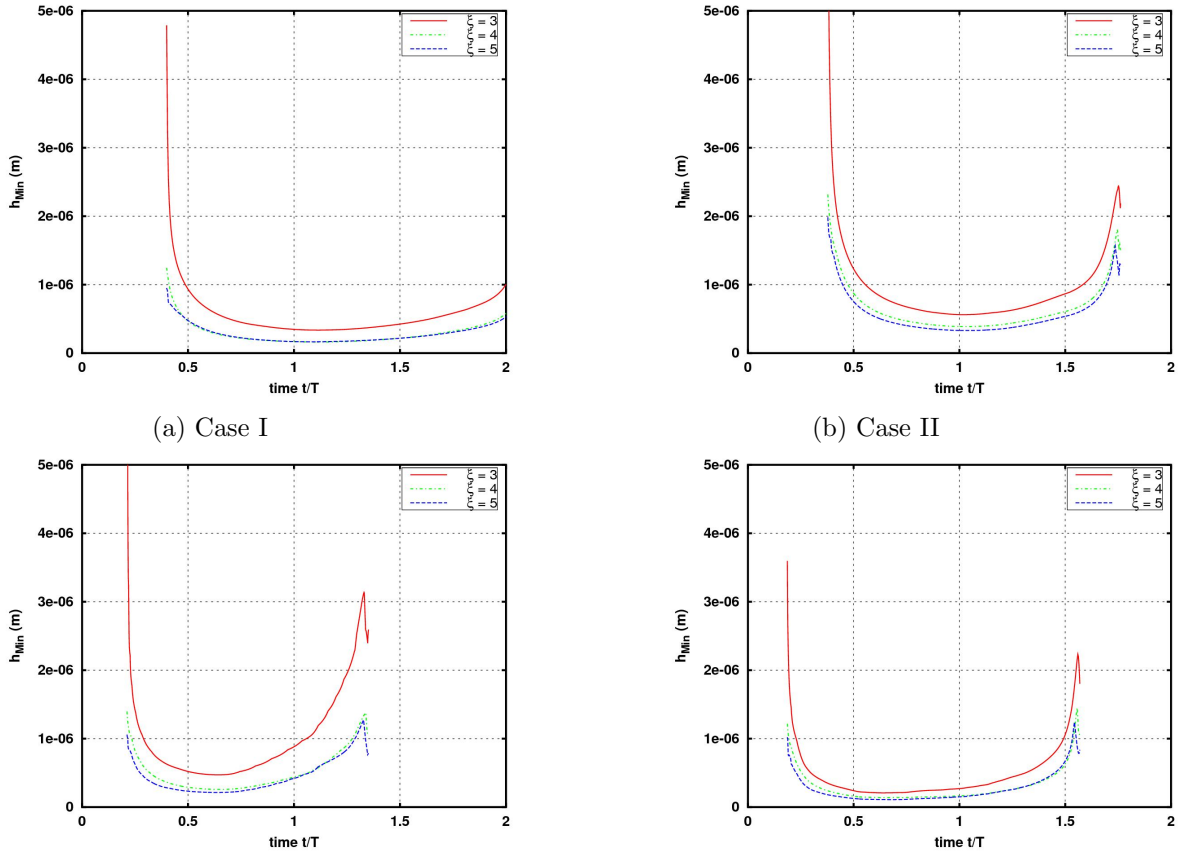

(a) Case I

(b) Case II

(c) Case III

(d) Case IV

FIGURE 4.11: Variation of parameter ξ with time for (a) Case I, (b) Case II, (c) Case III and (d) Case IV

very small change is observed between $\xi = 4$ and $\xi = 5$. It is therefore deduced that the results become independent of ξ in the region of $4 \leq \xi \leq 5$, and a value of $\xi = 4$ is chosen.

4.3.3.2 Selection of parameter h_{Crit}

The parameter h_{Crit} defines the critical thin film thickness at which the film becomes unstable and ruptures. The values of the minimum thin film thickness for $\xi = 4$ for the coalescence test cases as highlighted in Table 4.8 are used to determine h_{Crit}.

The determination of h_{Crit} is similar to that of ξ, h_{Crit} is initially set to zero and the numerical results at $\xi = 4$ are obtained for the four test cases. From Table 4.8, for coalescence to occur for Case I the critical film thickness should be greater than 1.618 $\times 10^{-7}$m while for Case IV the critical film thickness should be greater than 1.382 $\times 10^{-7}$m. On the other hand, to prevent coalescence in Case II, the critical film thickness should be less than 3.872×10^{-7}m and in Case III it should be less than 2.573×10^{-7}m.

A global h_{Crit} that is applicable to all four test cases is sought: a value such that $1.618\times10^{-7}\text{m} < h_{Crit} < 2.573\times10^{-7}\text{m}$ must be selected. The critical film thickness selected to obtain the numerical results is $h_{Crit} = 1.650\times10^{-7}\text{m}$. Thus according to the solution procedure of the surface thin film model outlined in Chapter 3, Section 3.4.2, when $min(h) < h_{Crit} = 1.650\times10^{-7}\text{m}$ the volume fraction fields are merged.

Pan et al. (2008) calculated the minimum film thickness for the cases resulting in merging to be $2\times10^{-7}\text{m}$. In this study the minimum film thickness for the cases that result in merging is $1.618\times10^{-7}\text{m}$ for Case I and $1.382\times10^{-7}\text{m}$ for Case IV. The current study under predicts the minimum thin film thickness by 19.1% for Case I and by 30.9% for Case IV compared to the study of Pan et al. (2008). The numerical results of Mason et al. (2014) used a critical film thickness of $0.4\times10^{-7}\text{m}$ in obtaining the numerical results.

Chen and Yang (2014) used the head-on collision resulting in bouncing to test their adaptive mesh refinement technique using an axisymmetric simulation. Their minimum cell spacing used in their simulations was roughly $0.15\times10^{-7}\text{m}$ and a minimum gas film thickness of $3\times10^{-7}\text{m}$ was calculated. In the current study the minimum thin film thickness obtained for the bounce test cases is $3.872\times10^{-7}\text{m}$ for Case II and $2.573\times10^{-7}\text{m}$ for Case III with a minimum mesh cell spacing of $0.682\times10^{-3}\text{m}$. The present study over-predicts the minimum film thickness by 29.1% for Case II and under predicts by 14.2% for Case III compared to the study of Chen and Yang (2014) but at a much more reasonable minimum mesh cell spacing.

4.3.3.3 Droplet time series plots

The chosen parameters of ξ and h_{Crit} in the previous two sub-sections are used to obtain the numerical solution. The time series droplet interface shape plots for the four test cases are given in Figure 4.12 – Figure 4.16. The time series is given at nondimensional times, normalized by the droplet oscillation period T.

The simulated results of Case I qualitatively agree well with the experimental results before coalescence occurs. The droplet deformation is a function of the film drainage time, the time at which the thin film becomes unstable and ruptures. In their numerical simulation using the front tracking method, (Pan et al., 2008) noted that an earlier or later film drainage time results in significantly different physical deformation features. They obtained the correct physical deformation by setting the rupture time to the experimental rupture time. The film is ruptured when the critical film thickness is $h_{Crit} = 1.650\times10^{-7}\text{m}$.

Mason et al. (2014) studied the interaction between a droplet and an interface driven by buoyancy. Their model coupled the CSF method in the framework of a LS method to a lower dimensional thin film equation based on lubrication theory. Their numerical results also showed a sensitive dependence of the collision dynamics to the film drainage time as observed from the results leading to coalescence of the present study.

The time series droplet interface shapes of Case II agree qualitatively with the experimental results with a slight delay in the dynamics after the droplets attain maximum deformation while they are still together. This delay is evident from 1.250 – 1.500 during the rebound stage. The droplets in this test case never attain the critical film thickness and thus the α equations are never set equal and thus no merging occurs.

As with Case II, the time series droplet interface shapes of Case III agrees qualitatively with the experimental results during the first two stages. As the droplets approach each other a larger deformation in the droplet shape is observed compared to Case II. During time period 1.083 – 1.806 is when the droplets start to rebound, there is evident delay in the dynamics.

Cases II and III demonstrate the ability of the SMMVOF method to successfully simulate collisions that result in rebound. The minimum film thickness in these cases was found to be of the order $O(10^{-7})$ which is much less than a single mesh cell spacing – the minimum mesh cell spacing being of the order $O(10^{-3})$.

Similar to Case I, Case IV numerical results agree qualitatively only up to coalescence. The coalescence in the simulation occurs earlier than the experimental coalescence which results in a lag in the deformation features after the coalescence as seen from time 0.606 – 0.703.

4.4 Closure

In this chapter the three aspects to the model for simulating particle-particle interactions that result in either coalescence or rebound were tested and validated.

The diffusive type smoother was applied to a static two-dimensional sphere to test whether the magnitude of nonphysical velocities would decrease. The numerical results of the time averaged pressure were compared to the analytic Young-Laplace equation and it was found that an increase in the smoothing parameter χ provided a better estimate for the pressure. This demonstrated that the curvature was being correctly calculated. This resulted in a significant decrease in the magnitude of the nonphysical velocities.

The validated diffusive type smoother with a smoothing parameter value of $\chi = 3$ was used as a basis for the SMMVOF method.

The SMMVOF method was tested by simulating the gravity driven droplet impact onto a liquid-liquid interface. Excellent qualitative results of the droplet deformation were observed and compared to the experiment of Pan et al. (2008). The results were obtained at a reduced computational cost compared to the numerical study of Coyajee and Boersma (2009). The numerical results demonstrated that the SMMVOF method was capable of simulating interactions that result in rebound.

The validated SMMVOF method was used as a basis for the reduced-order surface thin film model. It was demonstrated that coupled to the SMMVOF method the surface thin film model provides a model that is capable of simulating droplet-droplet interaction that results in coalescence. The droplet time series plots agreed qualitatively with the experimental results. The model parameter ξ was chosen so that overall the thin film model does not exhibit sensitive dependence on the initial thin film thickness estimate h_{Est}.

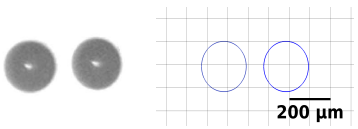

(a) t = 0

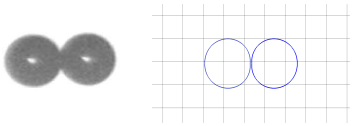

(b) t = 0.298

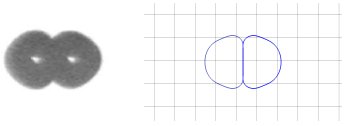

(c) t = 0.622

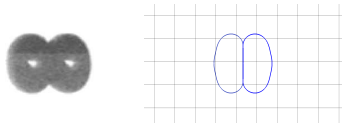

(d) t = 0.916

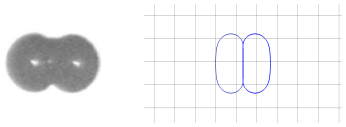

(e) t = 0.953

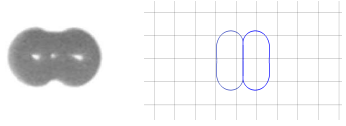

(f) t = 0.984

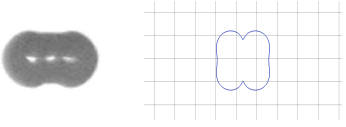

(g) t = 1.013

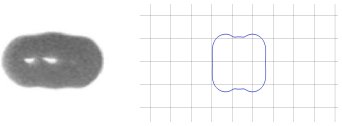

(h) t = 1.076

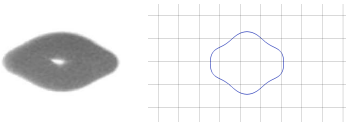

(i) t = 1.362

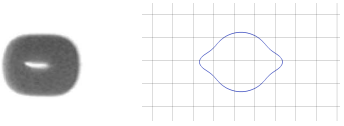

(j) t = 1.637

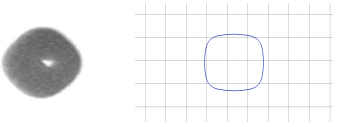

(k) t = 1.944

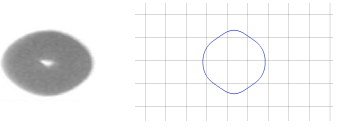

(l) t = 2.390

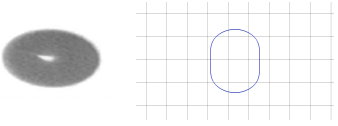

(m) t = 2.923

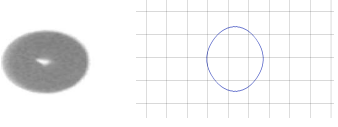

(n) t = 3.280

FIGURE 4.12: Time series interface shape deformations for Case I

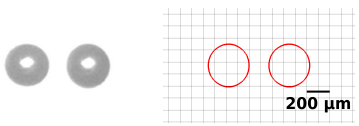

(a) t = 0

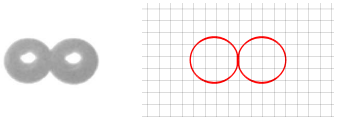

(b) t = 0.361

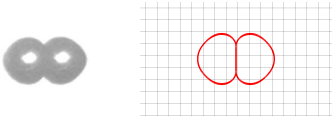

(c) t = 0.722

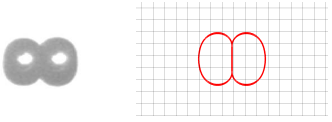

(d) t = 0.843

(e) 1.083

(f) t = 1.264

(g) t = 1.384

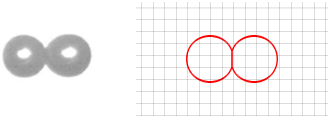

(h) 1.505

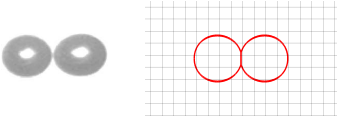

(i) t = 1.565

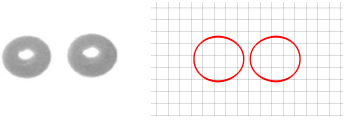

(j) t = 1.806

FIGURE 4.13: Time series interface shape deformations for Case II

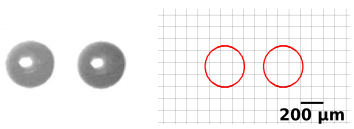

(a) t = 0.370

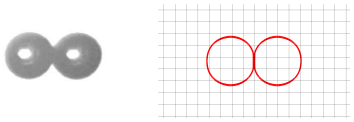

(b) t = 0.580

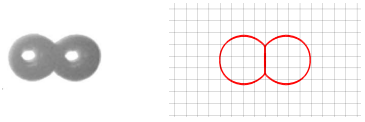

(c) t = 0.617

(d) t = 0.740

(e) t = 0.802

(f) t = 0.864

(g) t = 0.975

(h) t = 1.049

(i) t = 1.116

(j) t = 1.172

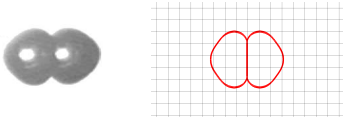

(k) t = 1.234

(l) t = 1.295

(m) t = 1.357

(n) t = 1.480

(o) t = 1.585

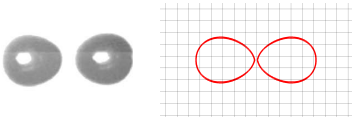

(p) t = 1.727

FIGURE 4.14: Time series interface shape deformations for Case III

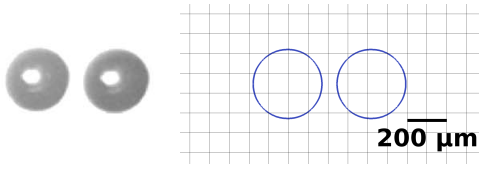

(a) t = 0.061

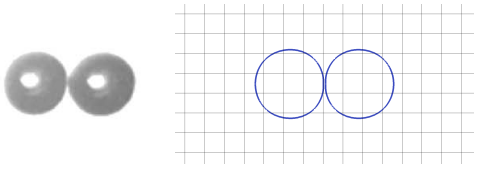

(b) t = 0.133

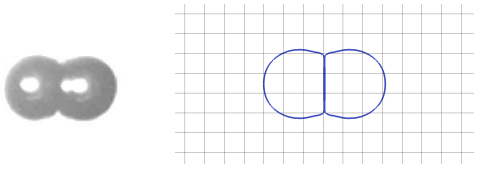

(c) t = 0.218

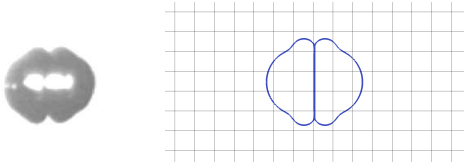

(d) t = 0.363

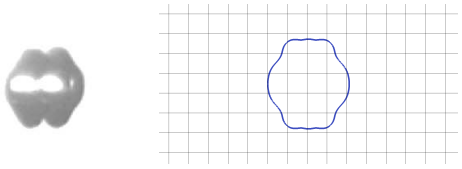

(e) t = 0.443

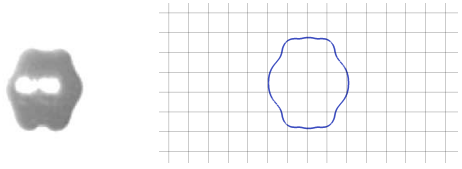

(f) t = 0.448

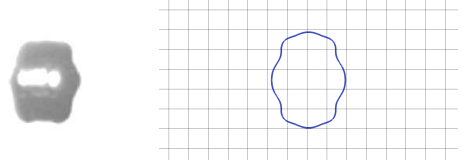

(g) t = 0.485

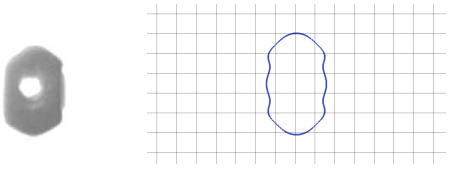

(h) t = 0.545

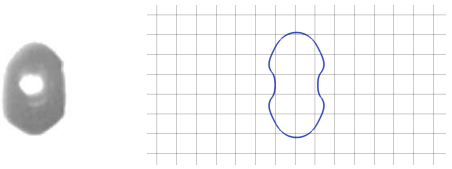

(i) t = 0.606

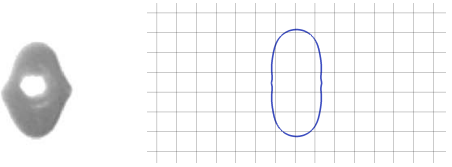

(j) t = 0.666

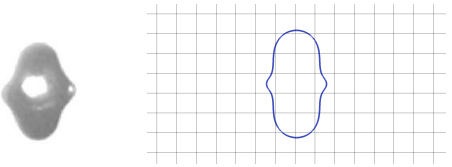

(k) t = 0.703

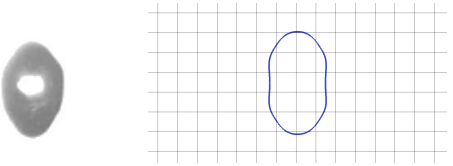

(l) t = 0.818

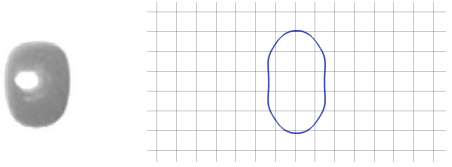

(m) t = 0.933

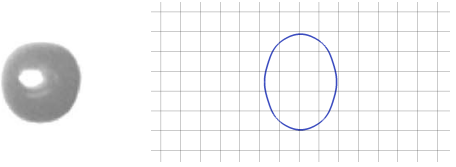

(n) t = 1.041

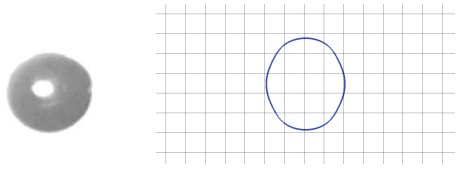

(a) t = 1.090

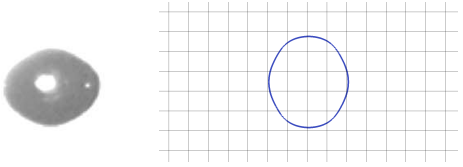

(b) t = 1.151

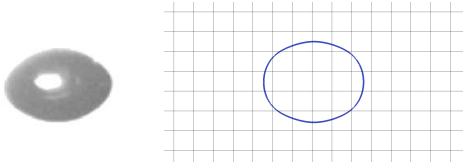

(c) t = 1.266

(d) t = 1.393

FIGURE 4.16: Time series interface shape deformations for Case IV

Chapter 5

Conclusions

The focus of this study has been to develop, implement and test a computational model in the OpenFOAM® framework, that determines the outcomes of particle-particle interactions. The goal has been to follow a multiscale method by using a DNS approach based on a smoothed VOF method that correctly computes interface curvatures to model the particle-particle interactions on the particle scale at a fundamental level, but by employing a surface thin film model to study the dynamics on the thin liquid film scale, to drastically reduce the computational effort that would otherwise be required.

5.1 Summary

5.1.1 Motivation

Particle-particle interactions within dispersed multiphase flows are a common occurrence in industrial processes. The hydrodynamic interaction of these particles which can lead to either coalescence or rebound influence the overall particle density in a multiphase reactor which in turn influences the operating efficiency. The CFD methods such as the Euler-Euler and the Euler-Lagrange formulations used to study these processes often on a large scale are known to use empirical correlations whenever modelling the interactions that result in either coalescence or rebound. Understanding and correctly modelling the underlying physics of the collision event at a fundamental level could vastly improve the operating efficiency of such processes.

The multiphase volume tracking conservative VOF method was chosen as it solves for the simulated motion of the particle-fluid interface at a fundamental level with reasonable computational cost. As it stands however, the VOF method has two major

drawbacks: the inability to compute interface curvatures accurately and the inability to model particle coalescence correctly.

5.1.2 Fluid flow modelling

The governing equations for dispersed multiphase flow were deduced from volume averaging the conservation equations for each individual phase. The resultant equations were the Navier-Stokes equations for an incompressible viscous multiphase Newtonian fluid undergoing laminar and isothermal three-dimensional flow. The VOF method was introduced to provide closure to the system of governing equations while the surface tension force was introduced using the CSF method.

Discretization followed the FVM using an implicit Euler method which resulted in a system of algebraic equations solved iteratively with the pressure being converged at every time step using a pressure correction algorithm (PISO).

Inherent to the VOF method are the nonphysical velocities that arise from a numerical inconsistency of inaccurately calculating interface curvatures with the CSF method. To reduce their magnitude a diffusive type smoother was introduced and coupled to the standard VOF method. This introduced an artificial smoothed volume fraction field that was smeared over a number of mesh cells χ. The smoothed volume fraction field was defined over more mesh cells compared to the standard volume fraction field which gave it a smooth transition rather than a step function.

This method was implemented into OpenFOAM® and a numerical static sphere test case was simulated. The sphere was placed in a two-dimensional square with assumed negligible gravity. The effect of the smoothing parameter ξ on the ability of the method to calculate the pressure difference across the sphere was evaluated together with the effect this has on the magnitude of the nonphysical velocities. A sensitivity study was done to determine the optimal value of ξ.

5.1.3 Particle interaction modelling

The film drainage theory was adopted in this study to argue the presence of a thin liquid film between interfaces of two particles and the resultant need to resolve the flow variables at very small length scales.

A test was performed that checked how well the VOF method correctly reconstructed the interfaces of two particles that are within half a mesh cell spacing of each other. It was found that the VOF accuracy increased with the number of computational cells

used. This highlighted the need to excessively refine the computational grid in the region of the thin liquid film if the smoothed VOF method is used to study particle interaction. For coarse computational grids the interfaces were observed to merge in what has been referred to in the literature as "artificial" or "numerical coalescence".

The governing equations for the smoothed VOF method were extended to include multiple volume fraction fields to form the SMMVOF method. This method differs from previous methods in the literature because it uses a smooth VOF method to accurately compute curvatures while other methods are based on a CLSVOF or a LS method. The SMMVOF method was implemented in OpenFOAM® and tested by simulating the gravity-driven three-dimensional droplet impact onto a liquid interface.

Although successful in preventing numerical coalescence, the SMMVOF method is incapable of simulating interactions that result in coalescence. A surface thin film model based on the Reynolds equation from lubrication theory was coupled to the SMMVOF method to calculate the critical film thickness that would determine the outcome of a collision. The equation resolved the thin film explicitly thus there was no need to use very fine computational grids.

The method was validated by simulating the collisions of Tetradecane droplets which result in either coalescence or rebound, and predicted a critical film thickness in agreement with the experimental results of Pan et al. (2008).

The implementation in this study uses the pressure from the Navier-Stokes equations as an input into the thin-film model. The film model is initialised with a grid-scale film thickness and thereafter allowed to solve independently on the sub-grid scale with pressure as the only input. This is in contrast to the similar technique of Mason et al. (2012) where velocity boundary conditions from the grid-scale flow model are applied to the film model, which is then used to solve for pressure. For this work, this approach was considered as problematic given the attempt to maintain tight coupling between velocities on different scales, and the great difference in magnitude between flow velocities and the small boundary velocity of the thinning film.

5.2 Findings

The following were the main findings of this work:

- The diffusive type smoother was successful in reducing the magnitude of nonphysical velocities and providing an accurate pressure difference estimate.

- The success of the diffusive type smoothing algorithm can be attested by the reduction of the nonphysical velocities compared to the standard OpenFOAM® solver interFoam. The smoothing algorithm was highly dependent on the number of cells over which the smoothing was performed with the parameter χ, the ideal value being $\chi = 3$.

- An increase in the smoothing coefficient decreased the magnitude of the nonphysical velocities. As reported in the literature, an increase in the surface tension coefficient increased the magnitude of the velocities. This supports claims that the VOF method struggles to simulate surface tension driven flows, examples including microfluidic flows. With the diffusive type smoother tested it was used as a basis for the multiple marker VOF method.

- The SMMVOF was tested and excellent qualitative agreement between the numerical and experimental results was observed.

- The computational time required by this implementation was drastically less than those reported in the literature for the other implementations.

- Excellent qualitative agreement in the centre line positions of the lower and upper droplet interfaces together with the droplet interface deformation shapes was observed. The SMMVOF method does not introduce any empirical or user defined parameters and was successful in preventing the numerical coalescence that is an artefact of the VOF method whenever interfaces were too close.

- The solution obtained by the SMMVOF method was found to improve with an increase in the mesh cell spacing but excellent results were obtained with relatively coarse computational grids.

- The collision of Tetradecane droplets in 1 atm Nitrogen was successfully simulated using the SMMVOF method coupled with the surface thin film model to determine the outcome of the collision event. The collision outcome was found to be highly dependent on the critical film thickness used. The actual rupture time determined the evolution and shape deformation that followed. Qualitative agreement of the collision sequence for the four Tetradecane test cases was observed.

- The calculated minimum film thickness was found to be independent of the initial film thickness estimate.

- The results of the current study demonstrated the predictive power of the surface thin film model. Although the critical flim thickness was set based on the experimental data, the results agreed with all four sets of experiments of Pan et al.

(2008) under different collision conditions. By comparison, only a single experiment was compared against in the work of Mason et al. (2012), and the result used for the critical film thickness in that study was an order of magnitude smaller than that deduced by Pan et al. from experimental data, and the value obtained in the present study. This difference is attributed to the different approach used for coupling the flow model and thin film equation, with only the pressure and not the velocity being coupled between the scales.

5.3 Recommendations for further study

A feasibility study on the number of particles the SMMVOF method can handle can be of great interest in determining its use for the study of bubble interactions in real bubble column reactors.

Further work can be directed towards performing multiscale simulations where the present model is used to validate the closure relations in the Euler-Euler or Euler-Lagrange type simulations of dispersed multiphase flow.

The surface thin film model did not include any short range forces such as the London van der Waals but the numerical results for the Tetradecane collision sequences agreed with the model. The minimum thin film thickness for the four Cases considered was of the order $O(10^{-7})$ which is much higher than the range required for the forces to be dominant. Further work would be to include the forces in the model for situations when the thickness is below $O(10^{-7})$.

Thin film dimpling was not studies because of the assumption of plane parallel interfaces, a further study comparing the numerical results of the thin film evolution with and without the assumption could give insights into dimple formation.

Appendix A

Volume averaging theorems

Let $\langle\cdot\rangle$ denote the average of a quantity. The averaging theorems are used to evaluate the average of the time derivative, the average of the gradient and the average of the divergence,

$$\langle\frac{\partial\Psi_k}{\partial t}\rangle = \frac{\partial}{\partial t}\langle\Psi_k\rangle - \frac{1}{V}\int_{\Gamma\cap V}\Psi_k\mathbf{v}_k\cdot\mathbf{n}_k dS, \tag{A.1}$$

$$\langle\nabla\Psi_k\rangle = \nabla\langle\Psi_k\rangle + \frac{1}{V}\int_{\Gamma\cap V}\Psi_k\mathbf{n}_k dS, \tag{A.2}$$

$$\langle\nabla\cdot\Psi_k\rangle = \nabla\cdot\langle\Psi_k\rangle + \frac{1}{V}\int_{\Gamma\cap V}\Psi_k\cdot\mathbf{n}_k dS, \tag{A.3}$$

where V is the averaging volume, $\mathbf{v}_k$ is the velocity of the interface, $\mathbf{n}_k$ is the outward unit normal vector and $\Gamma\cap V$ is part of the interface inside the averaging volume.

To evaluate the average of the non-linear term, a fluctuating velocity field $\mathbf{u}'_k$ is defined by

$$\langle\mathbf{u}_k\mathbf{u}_k\rangle = \alpha_k\langle\mathbf{u}_k\rangle^k\langle\mathbf{u}_k\rangle^k + \alpha_k\langle\mathbf{u}'_k\mathbf{u}'_k\rangle^k \tag{A.4}$$

where the second term is a dispersion whose contribution to the momentum equation can be ignored. Thus

$$\langle\mathbf{u}_k\mathbf{u}_k\rangle = \alpha_k\langle\mathbf{u}_k\rangle^k\langle\mathbf{u}_k\rangle^k. \tag{A.5}$$

Appendix B

Solution procedure flow chart

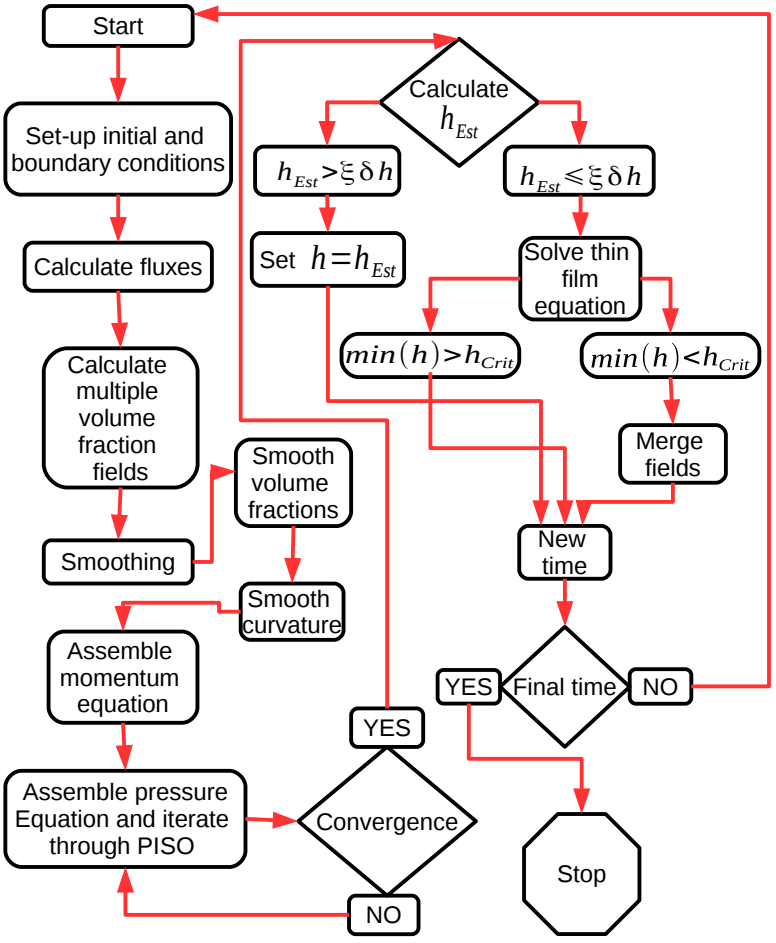

FIGURE B.1: Flow chart of numerical algorithm

Bibliography

The OpenFoam foundation. `http://openfoam.org/`. Accessed: 2016-05-15.

A. Albadawi, D. Donoghue, A. Robinson, D. Murray, and Y. Delauré. On the assessment of a VOF based compressive interface capturing scheme for the analysis of bubble impact on and bounce from a flat horizontal surface. *International Journal of Multiphase Flow*, 65:82–97, 2014.

N. Balcázar, O. Lehmkuhl, J. Rigola, and A. Oliva. A multiple marker Level-Set method for simulation of deformable fluid particles. *International Journal of Multiphase Flow*, 74:125–142, 2015.

P. T. S. Benjamin Steinhaus and A. Q. Shen. Droplet size effects on film drainage between droplet and substrate. *Langmuir*, 22(12):5308–5313, 2006.

J. Brackbill, D. B. Kothe, and C. Zemach. A continuum method for modeling surface tension. *Journal of Computational Physics*, 100(2):335–354, 1992.

D. Y. C. Chan, E. Klaseboer, and R. Manica. Film drainage and coalescence between deformable drops and bubbles. *Soft Matter*, 7:2235–2264, 2011.

J.-D. Chen, P. S. Hahn, and J. C. Slattery. Coalescence time for a small drop or bubble at a fluid-fluid interface. *American Institute of Chemical Engineers Journal*, 30(4): 622–630, 1984.

P. Chen, J. Sanyal, and M. Dudukovic. CFD modeling of bubble columns flows: implementation of population balance. *Chemical Engineering Science*, 59(22-23):5201–5207, 2004.

P. Chen, J. Sanyal, and M. Duduković. Numerical simulation of bubble columns flows: effect of different breakup and coalescence closures. *Chemical Engineering Science*, 60 (4):1085–1101, 2005.

X. Chen and V. Yang. Thickness-based adaptive mesh refinement methods for multiphase flow simulations with thin regions. *Journal of Computational Physics*, 269: 22–39, 2014.

M. H. Cho, H. G. Choi, and J. Y. Yoo. A direct reinitialization approach of Level-Set/splitting finite element method for simulating incompressible two-phase flows. *International Journal for Numerical Methods in Fluids*, 67(11):1637–1654, 2011.

D. Colella, D. Vinci, R. Bagatin, M. Masi, and E. ABu Bakr. A study on coalescence and breakage mechanisms in three different bubble columns. *Chemical Engineering Science*, 54(21):4767–4777, 1999.

J. Coons, P. Halley, S. McGlashan, and T. Tran-Cong. A review of drainage and spontaneous rupture in free standing thin films with tangentially immobile interfaces. *Advances in Colloid and Interface Science*, 105(1-3):3–62, 2003.

E. Coyajee and B. J. Boersma. Numerical simulation of drop impact on a liquid-liquid interface with a multiple marker front-capturing method. *Journal of Computational Physics*, 228(12):4444–4467, 2009.

S. J. Cummins, M. M. Francois, and D. B. Kothe. Estimating curvature from volume fractions. *Computers & Structures*, 83(6–7):425–434, 2005.

D. Darmana, N. Deen, and J. Kuipers. Detailed modeling of hydrodynamics, mass transfer and chemical reactions in a bubble column using a discrete bubble model. *Chemical Engineering Science*, 60(12):3383–3404, 2005.

F. de Sousa, N. Mangiavacchi, L. Nonato, A. Castelo, M. Tomé, V. Ferreira, J. Cuminato, and S. McKee. A front-tracking/front-capturing method for the simulation of 3D multi-fluid flows with free surfaces. *Journal of Computational Physics*, 198(2):469–499, 2004.

E. Delnoij, J. Kuipers, and W. van Swaaij. Computational Fluid Dynamics applied to gas-liquid contactors. *Chemical Engineering Science*, 52(21-22):3623–3638, 1997a.

E. Delnoij, F. Lammers, J. Kuipers, and W. van Swaaij. Dynamic simulation of dispersed gas-liquid two-phase flow using a discrete bubble model. *Chemical Engineering Science*, 52(9):1429–1458, 1997b.

E. Delnoij, J. Kuipers, and W. van Swaaij. Numerical simulation of bubble coalescence using a volume of fluid (VOF) model. In *Third International Conference on Multiphase Flows 1998, June 8-12, Lyon, France*, 1998.

E. Delnoij, J. Kuipers, and W. van Swaaij. A three-dimensional CFD model for gas–liquid bubble columns. *Chemical Engineering Science*, 54(13-14):2217–2226, 1999.

F. Denner, D. R. van der Heul, G. T. Oud, M. M. Villar, A. da Silveira Neto, and B. G. van Wachem. Comparative study of mass-conserving interface capturing frameworks

for two-phase flows with surface tension. *International Journal of Multiphase Flow*, 61:37–47, 2014.

C. Fleischer, S. Becker, and G. Eigenberger. Detailed modeling of the chemisorption of CO_2 into NaOH in a bubble column. *Chemical Engineering Science*, 51(10):1715–1724, 1996.

C. Focke, M. Kuschel, M. Sommerfeld, and D. Bothe. Collision between high and low viscosity droplets: Direct numerical simulations and experiments. *International Journal of Multiphase Flow*, 56:81–92, 2013.

M. Gauer, V. Hannemann, and K. Hannemann. Implementation of the VOF method in the DLR TAU code. In *45th AIAA/ASME/ASEE Joint Propulsion Conference & Exhibit*, 2009.

B. Gorain, J.-P. Franzidis, and E. Manlapig. Studies on impeller type, impeller speed and air flow rate in an industrial scale flotation cell — part 1: Effect on bubble size distribution. *Minerals Engineering*, 8(6):615–635, 1995.

M. Gorokhovski and M. Herrmann. Modeling primary atomization. *Annual Review of Fluid Mechanics*, 40(1):343–366, 2008.

S. Grevskott, B. Sannæs, M. Duduković, K. Hjarbo, and H. Svendsen. Liquid circulation, bubble size distributions, and solids movement in two- and three-phase bubble columns. *Chemical Engineering Science*, 51(10):1703–1713, 1996.

F. H. Harlow and J. E. Welch. Numerical calculation of time dependent viscous incompressible flow of fluid with free surface. *Physics of Fluids*, 8(12):2182–2189, 1965.

D. Harvie, M. Davidson, and M. Rudman. An analysis of parasitic current generation in volume of fluid simulations. *Applied Mathematical Modelling*, 30(10):1056–1066, 2006.

J. A. Heyns, T. M. Harms, and A. G. Malan. Free-surface modelling technology for compressible and violent flows. In *20th AIAA Computational Fluid Dynamics conference*, 2011.

C. Hirt and B. Nichols. Volume of fluid (VOF) method for the dynamics of free boundaries. *Journal of Computational Physics*, 39(1):201–225, 1981.

R. Issa, A. Gosman, and A. Watkins. The computation of compressible and incompressible recirculating flows by a non-iterative implicit scheme. *Journal of Computational Physics*, 62(1):66–82, 1986.

H. Jakobsen, H. Lindborg, and C. Dorao. Modeling of bubble column reactors: Progress and limitations. *Industrial & Engineering Chemistry Research*, 44(14):5107–5151, 2005.

H. A. Jakobsen. *Bubble Column Reactors*, pages 883–935. Springer International Publishing, 2014. ISBN 978-3-319-05092-8. doi: 10.1007/978-3-319-05092-8_8.

H. A. Jakobsen, B. H. Sannæs, S. Grevskott, and H. F. Svendsen. Modeling of vertical bubble-driven flows. *Industrial & Engineering Chemistry Research*, 36(10):4052–4074, 1997.

H. Jasak. *Error analysis and estimation for the finite volume method with applications to fluid flows*. PhD thesis, Imperial College of Science, Technology and Medicine, 1996.

X. Jiang and A. J. James. Numerical simulation of the head-on collision of two equal-sized drops with van der waals forces. *Journal of Engineering Mathematics*, 59(1): 99–121, 2006.

R. Krishna, J. Ellenberger, and C. Maretto. Flow regime transition in bubble columns. *International Communications in Heat and Mass Transfer*, 26(4):467–475, 1999.

R. Kuriakose and C. Anandharamakrishnan. Computational fluid dynamics (CFD) applications in spray drying of food products. *Trends in Food Science & Technology*, 21(8):383–398, 2010.

M. Kwakkel, W.-P. Breugem, and B. J. Boersma. An efficient multiple marker front-capturing method for two-phase flows. *Computers & Fluids*, 63:47–56, 2012.

M. Kwakkel, W.-P. Breugem, and B. J. Boersma. Extension of a CLSVOF method for droplet-laden flows with a coalescence/breakup model. *Journal of Computational Physics*, 253:166–188, 2013.

B. Lafaurie, C. Nardone, R. Scardovelli, S. Zaleski, and G. Zanetti. Modelling merging and fragmentation in multiphase flows with SURFER. *Journal of Computational Physics*, 113(1):134–147, 1994.

A. Lapin and A. Lübbert. Numerical simulation of the dynamics of two-phase gas—liquid flows in bubble columns. *Chemical Engineering Science*, 49(21):3661–3674, 1994.

Y. Liao and D. Lucas. A literature review on mechanisms and models for the coalescence process of fluid particles. *Chemical Engineering Science*, 65(10):2851–2864, 2010.

C.-Y. Lin and J. C. Slattery. Thinning of a liquid film as a small drop or bubble approaches a fluid–fluid interface. *AIChE Journal*, 28(5):786–792, 1982.

T. Lin, J. Reese, T. Hong, and L. Fan. Quantitative analysis and computation of two-dimensional bubble columns. *AIChE Journal*, 42(2):301–318, 1996.

Z. Liu, J. Wu, H. Zhen, and X. Hu. Numerical simulation on head-on binary collision of gel propellant droplets. *Energies*, 6(1):204–219, 2013.

A. Lubbert, T. Paaschen, and A. Lapin. Fluid dynamics in bubble column bioreactors: Experiments and numerical simulations. *Biotechnology and Bioengineering*, 52(2): 248–258, 1996.

A. J. A. Malavé, E. Sira, and M. G. Sucre. Film drainage between two drops: vortex formation in thin liquid films. *Interciencia: Revista de ciencia y tecnología de América*, 34(6):380–384, 2009.

R. Manica, J. N. Connor, R. R. Dagastine, S. L. Carnie, R. G. Horn, and D. Y. C. Chan. Hydrodynamic forces involving deformable interfaces at nanometer separations. *Physics of Fluids*, 20(3):032101, 2008.

L. Mason, G. Stevens, and D. Harvie. Multi-scale volume of fluid modelling of droplet coalescence. In *9th International conference on CFD in the Minerals and Process Industries*, 2012.

L. Mason, G. Stevens, and D. Harvie. Subgrid CFD film-drainage modelling: Application to buoyancy-driven droplet-wall collisions in emulsions. In *19th Australasian Fluid Mechanics Conference*, 2014.

Z. Mohamed-Kassim and E. K. Longmire. Drop impact on a liquid–liquid interface. *Physics of Fluids (1994-present)*, 15(11):3263–3273, 2003.

Z. Mohamed-Kassim, E. K. Longmire, X. Zheng, and J. Lowengrub. Experiments and computations on drop impact at a liquid/liquid interface. In *5th International Conference on Multiphase Flow*, 2004.

A. Murrone and P. Villedieu. Numerical modeling of dispersed two-phase flows. *Aerospace Lab*, 2(2):1–13, 2011.

N. Musehane, O. Oxtoby, and B. Reddy. Modelling bubble colum reactors: coalescence. In *Fourth African Conference of Computational Mechanics*, 2015. URL `http://africomp15.com/documents/Africomp15_booklet.pdf?&session-id=c69304346e5f45659bcfd8ac9457e956`.

N. Nikolopoulos, K. Nikas, and G. Bergeles. A numerical investigation of central binary collision of droplets. *Computers & Fluids*, 38(6):1191–1202, 2009a.

N. Nikolopoulos, A. Theodorakakos, and G. Bergeles. Off-centre binary collision of droplets: A numerical investigation. *International Journal of Heat and Mass Transfer*, 52(19-20):4160–4174, 2009b.

N. Nikolopoulos, G. Strotos, K. Nikas, and G. Bergeles. The effect of Weber number on the central binary collision outcome between unequal-sized droplets. *International Journal of Heat and Mass Transfer*, 55(7-8):2137–2150, 2012.

M. Nobari, Y. Jan, and G. Tryggvason. Head-on collision of drops–a numerical investigation. *Physics of Fluids*, 8(1):29, 1996.

W. F. Noh and P. Woodward. *Proceedings of the Fifth International Conference on Numerical Methods in Fluid Dynamics June 28–July 2, 1976 Twente University, Enschede*, chapter SLIC (Simple Line Interface Calculation), pages 330–340. Springer Berlin Heidelberg, 1976. ISBN 978-3-540-37548-7.

O. L. Néstor Balcázar, Llu ís Jofre et al. A multiple marker level-set method for simulation of bubbly flows. In J. O. E. O ńate and A. Huerta, editors, *11th World Congress on Computational Mechanics (WCCM XI), 6th European Conference on Computational Fluid Dynamics (ECFD VI), 5th European Conference on Computational Mechanics (ECCM V)*, 2014.

P. J. O'Rourke, P. P. Zhao, and D. Snider. A model for collisional exchange in gas/liquid/solid fluidized beds. *Chemical Engineering Science*, 64(8):1784 – 1797, 2009.

K.-L. Pan, C. K. Law, and B. Zhou. Experimental and mechanistic description of merging and bouncing in head-on binary droplet collision. *Journal of Applied Physics*, 103(6), 2008.

S. Pawar, J. Padding, N. Deen, A. Jongsma, F. Innings, and J. H. Kuipers. Numerical and experimental investigation of induced flow and droplet–droplet interactions in a liquid spray. *Chemical Engineering Science*, 138:17–30, 2015.

S. Quan. Dynamics and thin film drainage of a deformable droplet moving towards a solid wall with finite inertia. *RSC Advances*, 2:1927–1935, 2012.

V. Ranade. Modelling of turbulent flow in a bubble column reactor. *Chemical Engineering Research and Design*, 75(1):14–23, 1997.

Y. Renardy and M. Renardy. Prost: A parabolic reconstruction of surface tension for the volume-of-fluid method. *Journal of Computational Physics*, 183(2):400–421, 2002.

J. A. Sethian and P. Smereka. Level set methods for fluid interfaces. *Annual Review of Fluid Mechanics*, 35(1):341–372, 2003.

A. Sokolichin and G. Eigenberger. Gas—liquid flow in bubble columns and loop reactors: Part I. Detailed modelling and numerical simulation. *Chemical Engineering Science*, 49(24, Part 2):5735–5746, 1994.

A. Sokolichin, G. Eigenberger, A. Lapin, and A. Lübert. Dynamic numerical simulation of gas-liquid two-phase flows Euler/Euler versus Euler/Lagrange. *Chemical Engineering Science*, 52(4):611–626, 1997.

M. Sussman and E. Fatemi. An efficient, interface-preserving level set redistancing algorithm and its application to interfacial incompressible fluid flow. *SIAM Journal on scientific computing*, 20(4):1165–1191, 1999.

M. Sussman and E. G. Puckett. A coupled level set and volume-of-fluid method for computing 3D and axisymmetric incompressible two-phase flows. *Journal of Computational Physics*, 162(2):301–337, 2000.

M. Sussman, E. Fatemi, P. Smereka, and S. Osher. An improved level set method for incompressible two-phase flows. *Computers & Fluids*, 27(5-6):663–680, 1998.

A. Tomiyama, A. Sou, H. Minagawa, and T. Sakaguchi. Numerical analysis of a single bubble by VOF method. *JSME International Journal Series B*, 36, 1993.

R. Tsekov and E. Ruckenstein. Dimple formation and its effect on the rate of drainage in thin liquid films. *Colloids and Surfaces A: Physicochemical and Engineering Aspects*, 82(3):255–261, 1994.

O. Ubbink and R. Issa. A method for capturing sharp fluid interfaces on arbitrary meshes. *Journal of Computational Physics*, 153(1):26–50, 1999.

S. O. Unverdi and G. Tryggvason. A front-tracking method for viscous, incompressible, multi-fluid flows. *Journal of Computational Physics*, 100(1):25–37, 1992.

M. van Sint Annaland, N. Deen, and J. Kuipers. Numerical simulation of gas bubbles behaviour using a three-dimensional volume of fluid method. *Chemical Engineering Science*, 60(11):2999–3011, 2005.

H. K. Versteeg and W. Malalasekera. *An introduction to computational fluid dynamics: the finite volume method*. Pearson Education, 2007.

S. Whitaker. The transport equations for multi-phase systems. *Chemical Engineering Science*, 28(1):139–147, 1973.

M. Wörner. *A Compact Introduction to the Numerical Modeling of Multiphase Flows*. Forschungszentrum Karlsruhe Technik und Umwelt. Forschungszentrum Karlsruhe, 2003. URL `https://books.google.co.za/books?id=pwCrMAEACAAJ`.

L. Y. Yeo, O. K. Matar, E. P. de Ortiz, and G. F. Hewitt. Film drainage between two surfactant-coated drops colliding at constant approach velocity. *Journal of Colloid and Interface Science*, 257(1):93–107, 2003.

D. L. Youngs. Time-dependent multi-material flow with large fluid distortion. *Numerical methods for fluid dynamics*, 24(2):273–285, 1982.

P. Zhang and C. K. Law. An analysis of head-on droplet collision with large deformation in gaseous medium. *Physics of Fluids*, 23(4), 2011.

C.-X. Zhao and A. P. Middelberg. Two-phase microfluidic flows. *Chemical Engineering Science*, 66(7):1394–1411, 2011.

X. Zheng, J. Lowengrub, A. Anderson, and V. Cristini. Adaptive unstructured volume remeshing – ii: Application to two- and three-dimensional level-set simulations of multiphase flow. *Journal of Computational Physics*, 208(2):626–650, 2005.